博　士　論　文

Study of the nonlinear pitch angle scattering of energetic particles caused by plasma waves in the magnetosphere

（磁気圏内プラズマ波動による高エネルギー粒子の非線形ピッチ角散乱についての研究）

東北大学大学院理学研究科地球物理学専攻

北原理弘

論文審査委員
加藤　雄人　准教授　(指導教員・主査)
小原　隆博　教　授
笠羽　康正　教　授
熊本　篤志　准教授
三好　由純　准教授　(名古屋大学)

平成２８年

Acknowledgement

I would like to express my sincere gratitude to my supervisor, Associate Professor Yuto Katoh, for his kind support and sound advice. His simulation results are the basis of this study. I wish to thank him for helpful suggestions and discussion.

I would also like to express my great thanks to Associate Professor Atsushi Kumamoto for deep and hearty discussion. I am grateful to Emeritus Professor Hiroshi Oya, who has provided me valuable suggestions and encouragement. I am also deeply grateful to the late Professor Takayuki Ono, who has introduced the space plasma physics to me.

I have been really helped by them for promoting the present study. Professors Takahiro Obara and Yasumasa Kasaba, Associate Professors Hiroaki Misawa, Takeshi Sakanoi, Naoki Terada, and Isao Murata, Drs. Fuminori Tsuchiya, Masato Kagitani, and Hiromu Nakagawa always assisted me to improve this work through useful discussion.

I extend my deep thanks to Professor Yoshiharu Omura, Associate Professor Yoshizumi Miyoshi, Dr. Yukitoshi Nishimura, and Ms. Yuko Kubota, for helpful comments and discussion on the present study. Dr. Masafumi Shoji provided very useful and worth simulation data with fruitful advice. The THEMIS data used in this study was provided by Professor Vassilis Angelopoulos. I also appreciate for his cooperation and kind support.

This work was carried out by the joint research program of the Institute for Space-Earth Environmental Research (ISEE), Nagoya University. This study was also supported by Grants-in-Aid for Scientific Research and JSPS Research Fellow.

All members of Space and Terrestrial Plasma Physics (STPP) Laboratory provided hearty support and great environment to accomplish this work. I wish to express my hearty thanks for their help and kindness.

Finally, I thank to my family for their warm support for a long period of years.

Abstract

Whistler mode chorus emissions are one of frequently observed plasma waves in the Earth's inner magnetosphere. Chorus emissions are generated near the magnetic equator through an instability driven by anisotropic electrons injected into the inner magnetosphere. Chorus emissions scatter energetic electrons in pitch angle, and precipitation of electrons as a result of the pitch angle scattering is one of candidate processes causing diffuse and pulsating auroras [e.g., Nishimura et al., 2010; 2011; Nishiyama et al., 2011; Miyoshi et al., 2010; 2015]. Chorus emissions are characterized by a sequence of intense and coherent wave elements with a frequency sweep, and rising tones are observed more frequently than falling tones. The frequency sweep is a strong evidence that non-linear processes are responsible for chorus generation [Omura et al., 2008; 2009; Katoh et al., 2007a, b].

Electromagnetic ion cyclotron (EMIC) waves are another mode of plasma waves in the inner magnetosphere. EMIC waves are generated by anisotropic ions and scatter energetic ions in pitch angle, driving proton aurora [e.g., Yahnin et al., 2007; Sakaguchi et al., 2008; Nomura et al., 2012; Nishimura et al., 2014]. Recently, EMIC waves with rising tones are discovered by satellite observations in the magnetosphere [e.g., Pickett et al., 2010; Sakagushi et al., 2013; Nakamura et al., 2014]. Furthermore, Nomura et al. (2016) reported that simultaneous observation of rising tone EMIC waves and pulsating pro-

ton aurora, and suggested that there is a strong relation between proton precipitation with pulsation and rising tone EMIC waves. These pitch angle scattering by wave-particle interaction not only causes the auroral precipitation but also plays an important role in loss of ring current particles [e.g., Jordanova et al., 1997]. Therefore, both chorus and EMIC waves are significant plasma waves closely related to the inner magnetospheric and auroral dynamics, and involve nonlinear wave-particle interaction processes.

A number of previous studies treat the pitch angle scattering of energetic particles (electrons or ions) as the diffusion process in the velocity phase space density and calculate diffusion coefficients from wave spectrum [e.g., Kennel and Engelmann, 1966; Lyons 1971; Thorne et al., 2010; Tao et al, 2011]. However, we cannot evaluate the nonlinearity of pitch angle scattering with the assumption of the diffusion model. In the quasi-linear regime, we assume that the pitch angle distribution of particles is gradually diffused by weak amplitude waves in the timescale of one hour. On the other hand, the nonlinear process [Omura et al., 2008; 2009; Hikishima et al., 2009] indicates that one chorus element strongly scatter particles in pitch angle. Simulation of rising tone EMIC waves also predict that the waves strongly scatter the pitch angle of protons toward the loss cone in short time scale [Omura et al., 2010; Shoji and Omura, 2013].

Direct evidence of wave-particle interaction is needed because we cannot quantitatively compare the distribution of particles and spectrum or waveform data in the time scale enough to resolve wave-particle interactions due to the limitation of the time resolution. Moreover, details of the physical process occurring in a short time scale are still unclear. We should also discuss the evolution of the distribution function of electrons or protons through nonlinear wave-particle interaction and validate assumptions used in theoretical

studies. The aims of this thesis are to establish the method of direct detection of nonlinear pitch angle scattering and to understand the basic process of nonlinear pitch angle scattering using simulation and observation data.

In chapter 2, we propose the general method to directly detect pitch angle scattering of energetic particles caused by plasma waves and focus on the pitch angle scattering of electrons caused by chorus emissions in the simulation system. Wave-Particle Interaction Analyzer (WPIA), a new instrument proposed by Fukuhara et al. (2009), measures the relative phase angle between the wave magnetic field vector and the velocity vector of each particle and calculates the energy exchange from waves to particles. We expand its applicability by proposing a method of using the WPIA to directly detect pitch angle scattering of resonant particles by plasma waves by calculating newly proposed G values. The G value is defined as the accumulation value of the Lorentz force acting on each particle and indicates the lost momentum of waves. We apply the proposed method to the results of a one-dimensional electron hybrid simulation reproducing the generation of whistler mode chorus emissions [Katoh and Omura, 2007a, b]. Using the wave and particle data obtained at fixed observation points assumed in the simulation system, we conduct a pseudo-observation of the simulation result using the WPIA and analyze the G values. Our analysis yields significant values indicating the strong pitch angle scattering for electrons in the kinetic energy and pitch angle ranges satisfying the cyclotron resonance condition with the reproduced chorus emissions. The results of this study demonstrate that the proposed method enables us to directly and quantitatively identify the location at which pitch angle scattering occurs in the simulation system.

In chapter 3, we focus on the the pitch angle scattering of energetic ions caused by rising tone EMIC waves observed by THEMIS satellites, and apply

the proposed method of WPIA to detect the pitch angle scattering. The Electrostatic Analyzer (ESA) installed on the THEMIS can detect ions in the energy range from 5 eV up to 25 keV with 32 energy channels. The ESA is designed with 180 degrees $\times$ 6 degrees fields-of-view and sweeps out 4π steradians each 3 s spin period. Since the maximum azimuthal angle resolution of the ESA burst-mode data is 22.5 degrees, the time resolution of the count rate detected by the ESA is 6 ms. The sampling frequency of burst-mode data of both the Electric Field Instrument (EFI) and the Fluxgate Magnetometer (FGM) are 128 Hz. Therefore, the THEMIS data of particles and waves have enough time resolutions to be applied the WPIA method to rising tone EMIC waves observed in the frequency range of 1 Hz. Using these plasma particle and wave data, we calculate the proposed G values with 90 s sliding time window. As a result of the analysis, we successfully detect the pitch angle scattering of ions by observation data. Furthermore, we compare the simulation results reproduced by an ion hybrid code [Shoji and Omura, 2011; 2013] and THEMIS observation. The both data show good agreement each other.

In chapter 4, we investigate the theoretical understanding of pitch angle scattering, especially low pitch angle electrons closely related to the auroral precipitation. Conventionally, it is considered that particles that satisfy the cyclotron resonance condition in the energy range from a few keV to tens keV are scattered toward the loss cone by whistler mode waves. Li et al. (2015) indicates, however, that low pitch angle particles tend to be scattered away from the loss cone by coherent whistler mode waves. Omura et al. (1991) reviewed the study of the motion of particles under the presence of coherent waves and represented the equation of motion of particle near the resonance condition as a pendulum equation. The derivation of the equation needs

assumptions that the wave amplitude is sufficiently small compared to the ambient magnetic field [Dysthe, 1971] and the pitch angle of particles is not small [Nunn, 1974]. In this chapter, we derive the equation of the motion of particles without both assumptions. The term that has been ignored previously means the Lorentz force caused by the wave magnetic field and the parallel velocity of particles. We clarify that particle near the loss cone satisfying the cyclotron resonant condition are scattered away from the loss cone, due to E_w and $v_\parallel \times B_w$ Lorentz force. In order to reproduce the pitch angle scattering caused by chorus emissions, we carry out a test particle simulation using the simulation system along a dipole magnetic field line and a whistler mode wave model. The results of test particle simulation are consistently explained by the nonlinear theory we derived. Furthermore, we estimate the modulation of pitch angle distribution while electrons encounter one wave packet of chorus emissions using an amount of particles in the pitch angle range from 0 to 90 degrees. Our results indicate that most of electrons near the loss cone scattered away from the loss cone and build a bump of distribution at the moderate pitch angle satisfying the cyclotron resonant condition.

Based on the results and discussion in this thesis, we conclude that the method we proposed using WPIA for direct detection of nonlinear pitch angle scattering is useful not only for the interaction between chorus emissions and electrons but also for the interaction between rising tone EMIC waves and ions. This method can identify the location at which pitch angle scattering occurs and the energy and pitch angle ranges in which energetic particles are effectively scattered. If we can apply the method to observation data of chorus emissions by ERG satellite, the process of wave-particle interaction in the magnetosphere will be clarified in detail. The theoretical approach

in chapter 4 is also significant to understand the fundamental process of nonlinear wave-particle interaction. The process of scattered electrons away from the loss cone producing anisotropic distributions is possibly related to the generation and damping mechanisms of chorus emissions. The proposed non-linear process should be validated by in-situ observations.

Contents

Chapter 1

Introduction

1.1 Earth's inner magnetosphere

The Earth has an intrinsic magnetic field, and the magnetosphere is formed as a consequence of the interaction with the solar wind. In particular, the dipole magnetic field region of magnetosphere is called the inner magnetosphere. In the inner magnetosphere, there are various kinds of plasma population (Figure 1.1). The plasmasphere is the most dense ($\sim$ 1000 /cc) and cold ($<$ 10 eV) plasma population in the inner magnetosphere and that is populated by the outflow of ionospheric plasma along low-latitude magnetic field lines. The ring current region consists of energetic particles (1 keV to a few hundred keV), and radiation belts discovered by James Van Allen consist of relativistic particles of more than a few hundreds keV. The electron radiation belts consist of the inner and outer radiation belts, and the region between them is called a slot region. In the inner magnetosphere, energetic electrons injected into the inner magnetosphere excite whistler mode chorus emissions on the dawn side, and injected ions generate electromagnetic ion cyclotron (EMIC) waves on the dusk side near the plasmapause

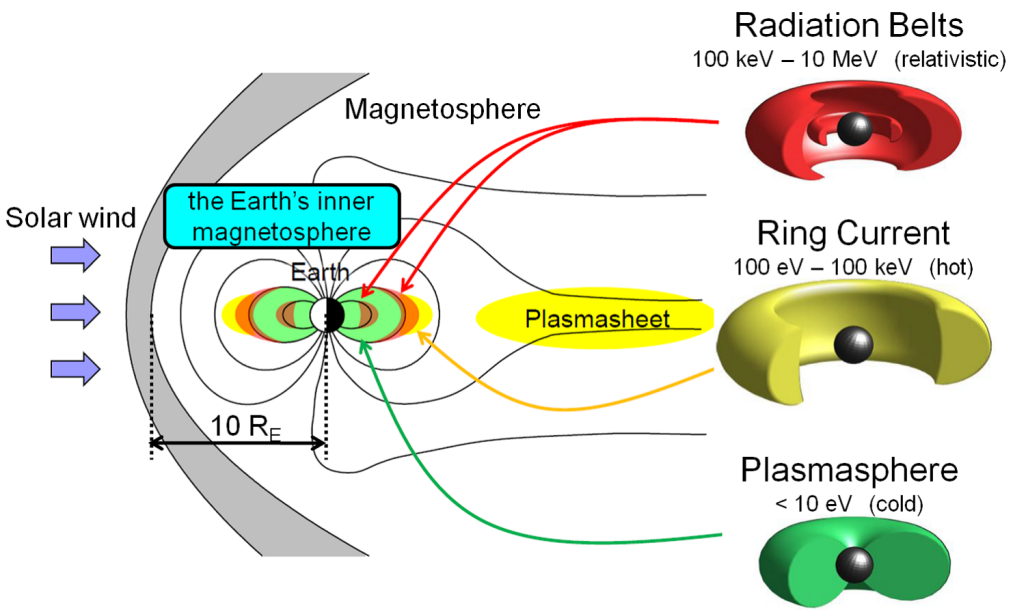

Figure 1.1: Overview of plasma population in the inner magnetosphere.

(Figure 1.2). Generated whistler mode waves and EMIC waves can interact with relativistic electrons through the cyclotron resonance, and these interactions are candidates of the accerelation and loss process of radiation belts [e.g., Summers et al., 1998]. In the Figure 1.3, we summarize the significant wave particle interactions between ring current/radiation belt electrons and whistler mode/EMIC waves.

1.2 Whistler mode chorus emissions

1.2.1 Brief history of study of whistler mode waves

The discovery of whistler mode wave phenomena is obscure. The first known report of whistlers is letter to the editor of Nature in 1894. According to Preece's paper, telephone operators in Britain heard some strange tones when they listened to telephone receivers connected to telegraph wire during

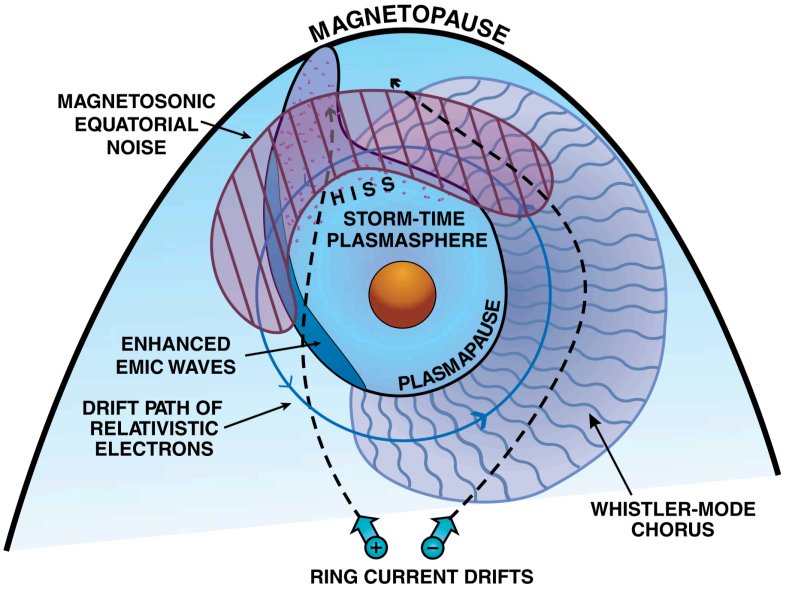

Figure 1.2: Schematic illustration of the spatial distribution of plasma waves [Summers et al., 1998; Thorne, 2010].

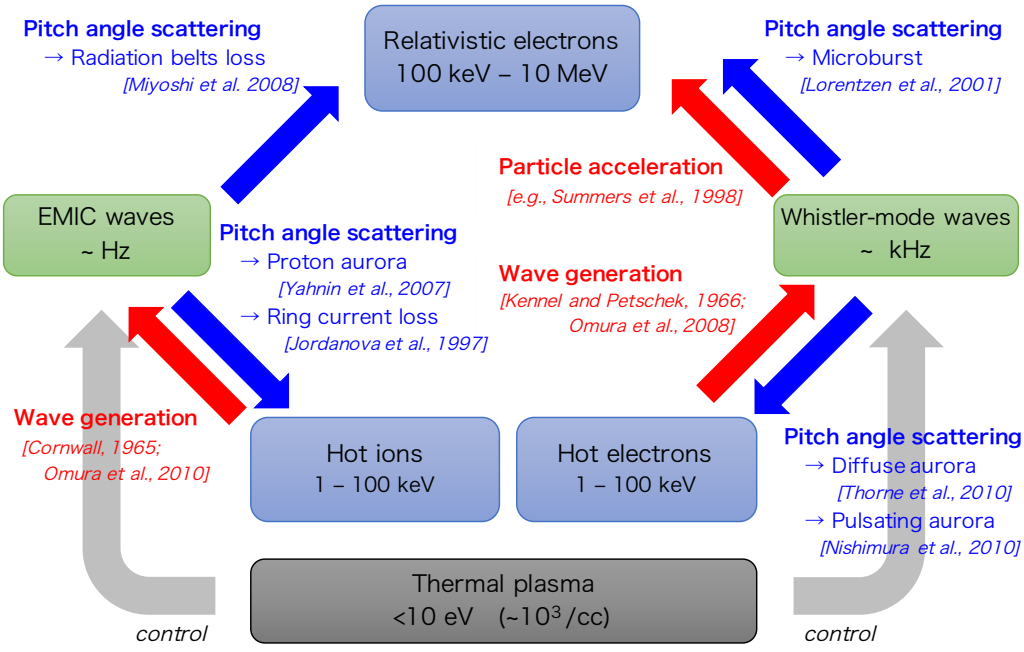

Figure 1.3: Wave particle interactions in the inner magnetosphere.

a display of aurora borealis on March 30–31. They reported: “Peculiar and wend sounds distinctly perceived, some highly-pitched musical notes, others resembling murmur of waves on a distant beach⋯” [Preece, 1894]. On the basis of the current knowledge, we can speculate that ”musical notes” that the operators had heard were chorus emissions which propagated from magnetosphere.

Allcock (1957) is probably the initial study of chorus emissions based on the grand observations. Allcock (1957) investigated the relation between the geomagnetic activity and the appearance of dawn chorus, and concluded that there are strong correlation between the occurrence rate of chorus emissions and the geomagnetic variations. Allcock (1957) also concluded that the entry of particles into the magnetosphere at the geomagnetic disturbance cause the propagation of chorus emissions into the atmosphere along the magnetic field. Gurnett and O’Brien (1964) reported the first satellite observations of the whistler mode phenomena made with the satellite Injun 3. The Injun 3 was designed and built by researchers at the University of Iowa, and was launched on December 13, 1962. A VLF detector (a loop antenna) installed on the Injun 3 successfully detected the whistlers, chorus and hiss emissions. Furthermore, the observations by the Injun 3 revealed that microbursts, which are impulsive precipitations of large fluxes of electrons into the auroral zone, are always accompanied by a group of chorus emissions, and chorus is not necessarily accompanied by the microbursts [Oliven and Gurnett, 1968]. Orbiting Geophysical Observatory (OGO) series, the six satellites launched to conduct diversified geophysical experiments, also detected chorus emissions in the magnetosphere. Burtis and Helliwell (1969) analyzed the frequency of chorus emissions observed by OGO 1 and OGO 3 and clarified that the chorus emissions are generated near the magnetic

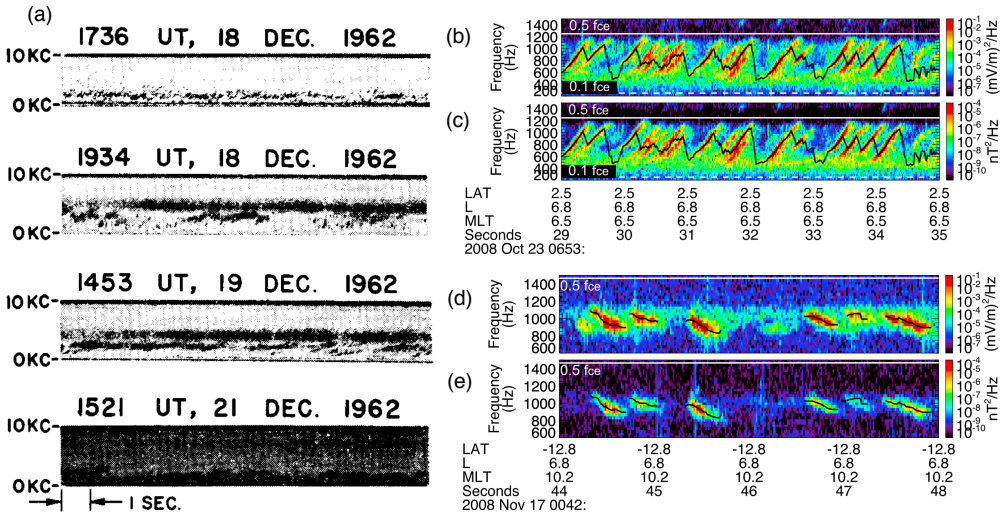

Figure 1.4: (a) Whistler mode chorus emissions observen by Injun 3 satellite [*Gurnett and O'Brien*, 1964] and (b)-(e) observed by THEMIS satellites [*Li et al.*, 2011]. (b) and (d) show wave electric field and (c) and (e) show wave magnetic field, respectively.

equator. Using the observation data by OGO 5, Tsurutani and Smith (1974) investigated the frequency property and existence region of chorus emissions. Chorus emissions are often observed in two distinct frequency bands, referred to as upper and lower band chorus, with a gap at half the electron cyclotron frequency. Chorus emissions are generated near the magnetic equator in association with injections of energetic electrons during a geomagnetic storm or substorm, and propagate along the Earth ' s magnetic field lines toward both hemispheres. The most of current knowledge about chorus emissions are based on Tsurutani and Smith (1974).

1.2.2 Generation process of chorus emissions

Whistler mode chorus emissions are one of the whistler-mode waves and are frequently observed in the inner magnetosphere [e.g., Tsurutani and Smith, 1974; Santolik et al., 2003, 2008]. Whistler mode chorus emissions are

generally characterized by a sequence of intense and coherent emissions with a frequency shift, and their frequency is less than the cyclotron frequency of electrons (Figure 1.4). Emissions with a positive or negative frequency sweep rate are called rising or falling tones, respectively, and rising tones are observed more frequently than falling tones. Whistler mode chorus emissions are generated near the magnetic equator, in association with injections of energetic electrons during a geomagnetic storm or substorm [Meredith et al., 2001; Meredith et al., 2002; Miyoshi et al., 2003], and propagate along the Earth's magnetic field lines toward both hemispheres.

The generation process of chorus emissions has been studied over a long period. Kennel and Petschek (1966) developed a linear growth theory in which whistler mode waves are generated by an instability driven by a temperature anisotropy in the velocity distribution function of energetic electrons. In the frame of a linear theory, the growth rate of whistler mode waves is derived from the linearly approximated Vlasov equation as the imaginary part of the frequency of plasma waves. The linear theory can describe the generation process of broadband whistler mode waves like hiss emissions, but cannot explain frequency shifts like chorus emissions. In order to describe the frequency shift of chorus emissions, Helliwell (1967) proposed the source-moving model. According to this model, because the cyclotron frequency is a function of position along the ambient magnetic field, the frequency shift of generated whistler mode waves is related to the variation of the location where waves interact with electrons. Trakhtengerts (1995) and Trakhtengerts et al. (1999) proposed the Backward Wave Oscillator (BWO) model, and the concept of the BWO model is close to the Helliwell ' s source-moving model. According to the BWO model, a step-like distribution of energetic electrons formed by noise-like emissions behaves like a beam, and a generation point

of a wave moves.

On the other hand, Omura et al. (2008, 2009) proposed a nonlinear wave growth theory for the generation mechanism of rising tone chorus emissions, and emphasized the importance of resonance currents formed by untrapped resonant electrons under the process of an electromagnetic electron hole in velocity phase space. The electromagnetic electron hole is produced by depletion of velocity phase space due to nonlinear interactions between a coherent whistler mode wave and resonant electrons moving along the field lines around the magnetic equator. The presence of the hole results in the formation of nonlinear resonant currents that contribute to the growth of coherent wave elements with a specific phase variation with significantly large growth rate rather than the linear growth rate. Based on the results of previous theoretical and simulation studies on chorus emissions, the nonlinear theory is promising and can be verified by obtaining evidence of an electromagnetic electron hole in the equatorial region of the inner magnetosphere during typical chorus events. However, the greatest difficulty with regard to direct measurements is that the hole is formed in a specific phase range relative to the wave magnetic field vector rotating with the wave frequency, which is several kilohertz in the inner magnetosphere. This is a crucial problem for conventional plasma instruments.

1.2.3 Pitch angle scattering and pulsating aurora

Pitch angle scattering of energetic electrons caused by whistler mode chorus emissions is a significant wave-particle interaction in the Earth's magnetosphere. Previous studies suggested that whistler mode chorus emissions play a dominant role in pitch angle scattering of energetic electrons in the kinetic energy range from a few to tens of keV, which is closely related to precipita-

tion contributing to diffuse aurora [e.g., Thorne et al., 2010; Nishimura et al., 2013] and pulsating aurora [Nishimura et al., 2010; 2011; Miyoshi et al., 2010; 2015; Nishiyama et al., 2011], and in the kinetic energy range from hundreds of keV to a few MeV, contributing to microburst precipitation in the outer zone of the Van Allen radiation belt [Nakamura et al., 2000; Lorentzen et al., 2001; Horne and Thorne 2003; Saito et al., 2012]. On the basis of the quasi-linear diffusion theory, previous studies of pitch angle scattering by whistler mode chorus emissions [Lyons, 1974; Thorne et al., 2010] evaluated the diffusion coefficients by referring to the observed whistler mode wave intensity and solved the Fokker-Planck equation for the temporal variation of the pitch angle distribution of energetic electrons. On the other hand, Hikishima et al. (2009) showed a nonlinear effect in the pitch angle scattering of energetic electrons caused by whistler mode chorus emissions. In the same simulation result, microburst precipitation of electrons in the energy range from 10 to 100 keV, which is considered to be the electron flux scattered by whistler mode chorus emissions, was detected [Hikishima et al., 2010]. These results suggest that nonlinear effects of chorus emissions should be considered for a thorough understanding of pitch angle scattering of energetic electrons in the magnetosphere.

1.3 Electromagnetic ion cyclotron (EMIC) waves with frequency shift

Pickett et al. (2010) discovered Electromagnetic Ion Cyclotron (EMIC) waves with frequency drift are observed by Cluster satellites in the Earth's inner magnetosphere. The phenomena are called EMIC triggered emissions or EMIC rising tones. Following the Cluster observation, various satellites

have observed the EMIC rising tones [e.g., Akebono: *Sakagushi et al.*, 2013; THEMIS: *Nakamura et al.*, 2014; RBSP: *Engebretson et al.*, 2015]. In the initial phase, EMIC waves are generated by anisotropic energetic ions through the cyclotron resonance [Cornwall, 1965]. Omura et al. (2010) showed that generation process of the EMIC rising tones could be explained by the nonlinear growth theory that is the same principle and conceptas the nonlinear generation process of whistler-mode chorus emissions [Omura et al., 2008; 2009]. Shoji and Omura (2011, 2013) successfully reproduced the EMIC rising tones by the one-dimensional ion hybrid simulation, and the theory have been compared to observations and simulation. With analogical consideration, we can expect that the ion pitch angle scattering is effectively caused by the EMIC rising tones like an interaction between the whistler mode chorus emissions and energetic electrons. Indeed, the velocity distribution function of ions is strongly modulated by the EMIC rising tones in the simulation [Shoji and Omura, 2013]. As whistler mode chorus emissions scatter energetic electrons and precipitated electrons cause diffuse and pulsating aurora, the precipitated ions by pitch angle scattering caused by EMIC waves may cause the proton aurora. Indeed, observation reported by Yahnin et al. (2007) also indicated that the proton precipitation caused by pitch angle scattering of EMIC waves caused the proton aurora. In the recent study, Nomura et al., (2016) reported the simultaneous observation of EMIC rising tones and pulsating proton aurora, and suggested that there is the strong relation between proton precipitation with pulsation and EMIC rising tones. These pitch angle scattering by wave-particle interaction is not only the cause of the auroral precipitation but also plays an important role in loss of ring current particles [e.g., Cornwall et al., 1970; Jordanova et al., 1997]. Thus both chorus and EMIC waves are fundamental modes of waves

in the inner magnetospheric and auroral dynamics, and involve non-linear wave-particle interaction processes.

1.4 Theory of pitch angle scattering

In this section, we summarize a brief review of theory of pitch angle scattering of plasma particles caused by plasma waves.

1.4.1 Quasi-linear diffusion model

The Vlasov equation of colisionless plasmas is given by

$$\frac{\partial f}{\partial t} + \boldsymbol{v} \cdot \nabla f + \frac{q}{m} (\boldsymbol{E} + \boldsymbol{v} \times \boldsymbol{B}) \cdot \frac{\partial f}{\partial \boldsymbol{v}} = 0. \tag{1.1}$$

Kennel and Engelmann (1966) and Lerche (1968) showed the quasi-linear diffudsion formula of resonant diffusion from equation (1.1), and Lyons et al. (1971) and Lyons (1974) represented the general quasi-linear diffusion equation.

$$\frac{\partial f}{\partial t} = \nabla_{\boldsymbol{v}} \cdot (\overleftrightarrow{\mathsf{D}} \cdot \nabla_{\boldsymbol{v}} f) \tag{1.2}$$

$$= \frac{1}{v \sin\alpha} \frac{\partial}{\partial \alpha} \sin\alpha \left(D_{\alpha\alpha} \frac{1}{v} \frac{\partial f}{\partial \alpha} + D_{\alpha v} \frac{\partial f}{\partial v} \right) + \frac{1}{v^2} \frac{\partial}{\partial v} v^2 \left(D_{v\alpha} \frac{1}{v} \frac{\partial f}{\partial \alpha} + D_{vv} \frac{\partial f}{\partial v} \right). \tag{1.3}$$

Diffusion coefficient is written as a summation over all harmonic resonance n:

$$D_{\alpha\alpha} = \sum_{n=-\infty}^{\infty} \int_0^{\infty} k_\perp dk_\perp D_{\alpha\alpha}^{nk_\perp}, \tag{1.4}$$

$$D_{\alpha v} = D_{v\alpha} = \sum_{n=-\infty}^{\infty} \int_0^{\infty} k_\perp dk_\perp D_{\alpha v}^{nk_\perp}, \tag{1.5}$$

$$D_{vv} = \sum_{n=-\infty}^{\infty} \int_0^{\infty} k_\perp dk_\perp D_{vv}^{nk_\perp}, \tag{1.6}$$

where

$$D_{\alpha\alpha}^{nk_\perp} = \lim_{V\to\infty} \frac{\pi q^2}{(2\pi)^2 V m^2} \left(\frac{-\sin^2\alpha + n\Omega/\omega}{\cos\alpha} \right)^2 \left. \frac{|\Theta_{nk}|^2}{|v_\parallel - \partial\omega/\partial k_\parallel|} \right|_{k_\parallel = k_{\parallel res}}, \tag{1.7}$$

$$D_{\alpha v}^{nk_\perp} = D_{\alpha\alpha}^{nk_\perp} \left(\frac{\sin\alpha\cos\alpha}{-\sin^2\alpha + n\Omega/\omega} \right) |_{k_\parallel = k_{\parallel res}}, \tag{1.8}$$

$$D_{vv}^{nk_\perp} = D_{\alpha\alpha}^{nk_\perp} \left(\frac{\sin\alpha\cos\alpha}{-\sin^2\alpha + n\Omega/\omega} \right)^2 |_{k_\parallel = k_{\parallel res}}, \tag{1.9}$$

and

$$\Theta_{nk} = \frac{E_{k,R} J_{n+1} + E_{k,L} J_{n-1}}{\sqrt{2}} + \frac{v_\parallel}{v_\perp} E_{k,\parallel} J_n. \tag{1.10}$$

V, q, m are the volume, the charge, and the rest mass of plasma, respectively, v is the velocity of a particle. ω and k are frequency and wave number of plasma waves. Subscripts $\perp$ and $\parallel$ refer to the componets of perpendicular and parallel to the ambient magnetic field $\boldsymbol{B}_0$. $\Omega = qB_0/m$ is the gyro frequency and J_n is the Bessel functions of $k_\perp v_\perp/\Omega$.

Assuming that the wave spectrums are a Gaussian distribution [e.g., Lyons, 1974; Albert, 1999; Glauert and Horne, 2005], we can use the fol-

lowing expressions.

$$B_w^2(\omega) = \begin{cases} A^2 \exp\left(-\left(\frac{\omega-\omega_m}{\delta\omega}\right)^2\right) & (\omega_{min} \leq \omega \leq \omega_{max}) \\ 0 & (\text{otherwise}), \end{cases} \tag{1.11}$$

where

$$A^2 = \frac{|B_w|^2}{\delta\omega}\frac{2}{\sqrt{\pi}}\left[\text{erf}\left(\frac{\omega_m - \omega_{min}}{\delta\omega}\right) + \text{erf}\left(\frac{\omega_{max} - \omega_m}{\delta\omega}\right)\right]^{-1}. \tag{1.12}$$

Furthermore, Summers (2005) approximated that wave propagation direction is purely parallel to $\boldsymbol{B}_0$ and the relativistic diffusion coefficient is given by

$$D_{\alpha\alpha} = \frac{\pi\Omega_\sigma^2}{2\nu|\Omega_e|\gamma^2}\sum_s\sum_j \frac{R\left(1-\frac{x\cos\alpha}{y\beta}\right)^2\left|\frac{dx}{dy}\right|}{\delta x\left|\beta\cos\alpha - \frac{dx}{dy}\right|}\exp\left[-\left(\frac{x-x_m}{\delta x}\right)^2\right], \tag{1.13}$$

where $\nu = \sqrt{\pi}\text{erf}((\omega_{max}-\omega_{min})/(2\delta\omega))$, $x = \omega_j/\Omega$, $y = ck_j/\Omega$, $\beta = v/c$, $\gamma = 1/\sqrt{1-\beta^2}$, $R = B_w^2/B_0^2$. The summations are carried out over the wave modes indicated by $s = -1$ (R-mode) and $s = 1$ (L-mode), and over the resonant frequency ω_j and wave number k_j corresponding to each wave mode.

One of the remarkable points of the quasi-linear diffusion model is $D_{\alpha\alpha}$ indicating the intensity of pitch angle diffusion is proportional to the the square of the wave amplitude, and the direction of pitch angle scattering is defined by the gradient of the phase space density, e.g., $\frac{\partial f}{\partial\alpha}$ and $\frac{\partial f}{\partial v}$. Waves are treated as the weak turbulence and pitch angle scattering is treated as a

diffusion as a summation of random small scatterings regardless of the basic physics.

1.4.2 Nonlinear theory

Whistler mode chorus emissions are generated by anisotropic energetic electrons in the energy range of a few to tens of keV, and scatter these electrons in pitch angle. Pitch angle scattering of energetic electrons caused by whistler mode chorus emissions at the magnetosphere is a strong candidate of the pulsating auroral precipitation into the ionosphere [e.g., Nishimura et al., 2010; Nishiyama et al., 2011; Miyoshi et al., 2015]. The process of pitch angle scattering are commonly expressed as a diffusion in the quasilinear theory [e.g., Lyons, 1974], and the results of the Fokker-Plunk simulation using the quasilinear theory concluded that the pitch angle distribution of anisotropic electrons is gradually diffused toward the loss cone by the weak amplitude waves in the timescale of one hour [Thorne et al., 2010]. On the other hand, nonlinear theory predicts that most of particles are scattered toward the loss cone and some particles in the specific phase are trapped and scattered away from the loss cone [Bortnik et al., 2008, Hikishima et al., 2009]. Omura et al. (1991) reviewed the study of the motion of particles in the waves and represented the equation of motion of particle near the resonance condition as a pendulum equation. The derivation of the equation needs assumptions that the the wave amplitude is sufficiently small compared to the ambient magnetic field [Dysthe, 1971] and the pitch angle of particles is not so small [Nunn, 1974]. As previous derivation, the basic equations are

expressed by the pendulum equations as following:

$$\frac{\mathrm{d}\zeta}{\mathrm{d}t} = \theta, \tag{1.14}$$

$$\frac{\mathrm{d}\theta}{\mathrm{d}t} = \omega_{tr}(\sin\zeta + S). \tag{1.15}$$

S parameter, so-called the inhomogeneity factor, is determined frequency sweep rate of coherent waves and gradient of ambient magnetic field intensity. Figure 1.5 shows the trajectories of electrons in the ζ-θ phase space in the case of the $S = -0.4$. The most of resonant particles encountering the coherent waves move around the outer circumference of the closed trajectory (electromagnetic electron hole) indicated white region of Figure 1.5. Therefore, the particles lose their energy and pitch angle. Figure 1.6 indicates the spatial profiles of S parameter and electromagnetic electron hole in the ζ-θ phase space. The nonlinear interaction is effectively cased at the near equator region. Bortnik et al. (2008) revealed that the scattering property was defined by the ration between the gradient of the ambient magnetic field and wave intensity, and the pitch angle scattering effectively shows strong nonlinearity in the case of large amplitude (Figures 1.7 and 1.4.2). However, However, the simulation result introduced by Li et al. (2015) indicates that all electrons near the loss cone scattered toward 90 degrees pitch angle away from the loss cone (Figure 1.9). This motion of particles are not expected from the nonlinear theory introduced in this section.

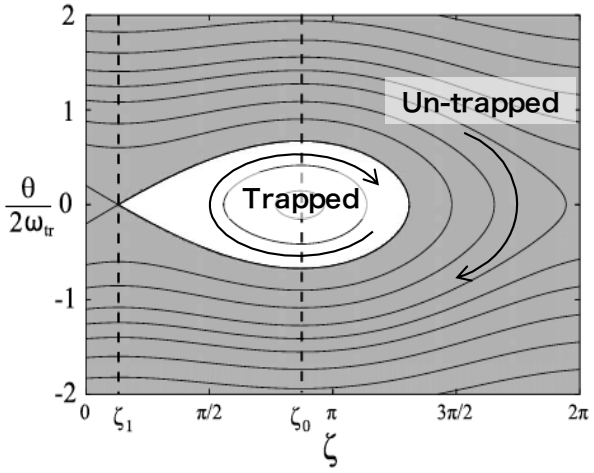

Figure 1.5: The trajectories of electrons in the ζ-θ phase space for $S = -0.4$. [after *Omura et al.,* 2008, 2009; *Hikishima et al.,* 2009, 2010]

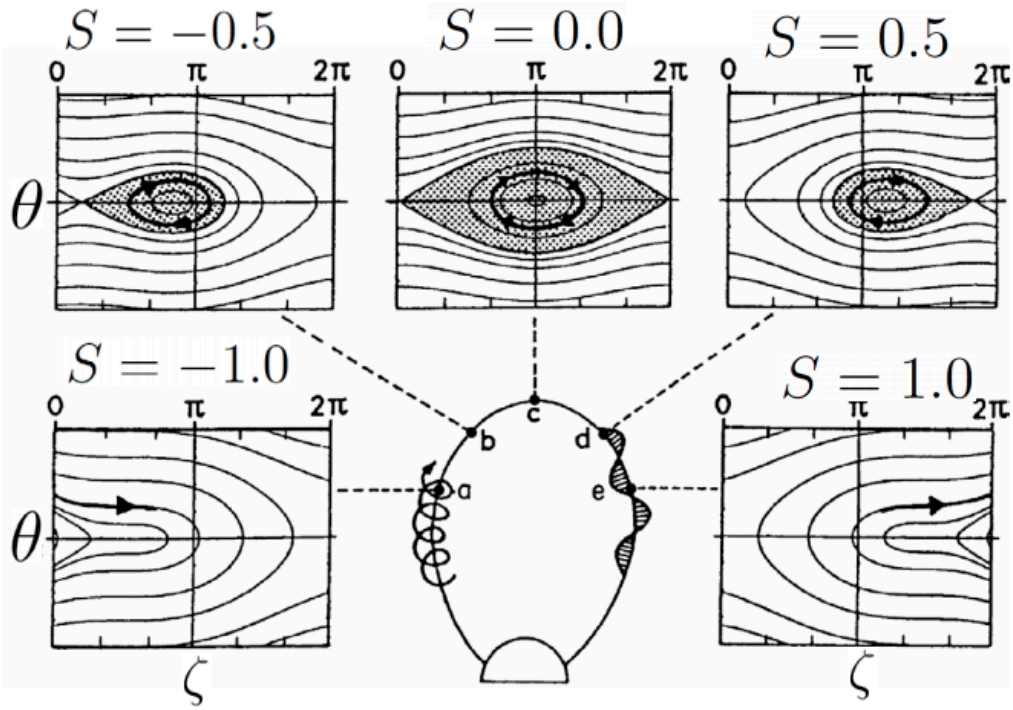

Figure 1.6: Spatial structure of S parameter and elecromagnetic electron hole in the ζ-θ phase space.[*Omura et al.,* 1991]

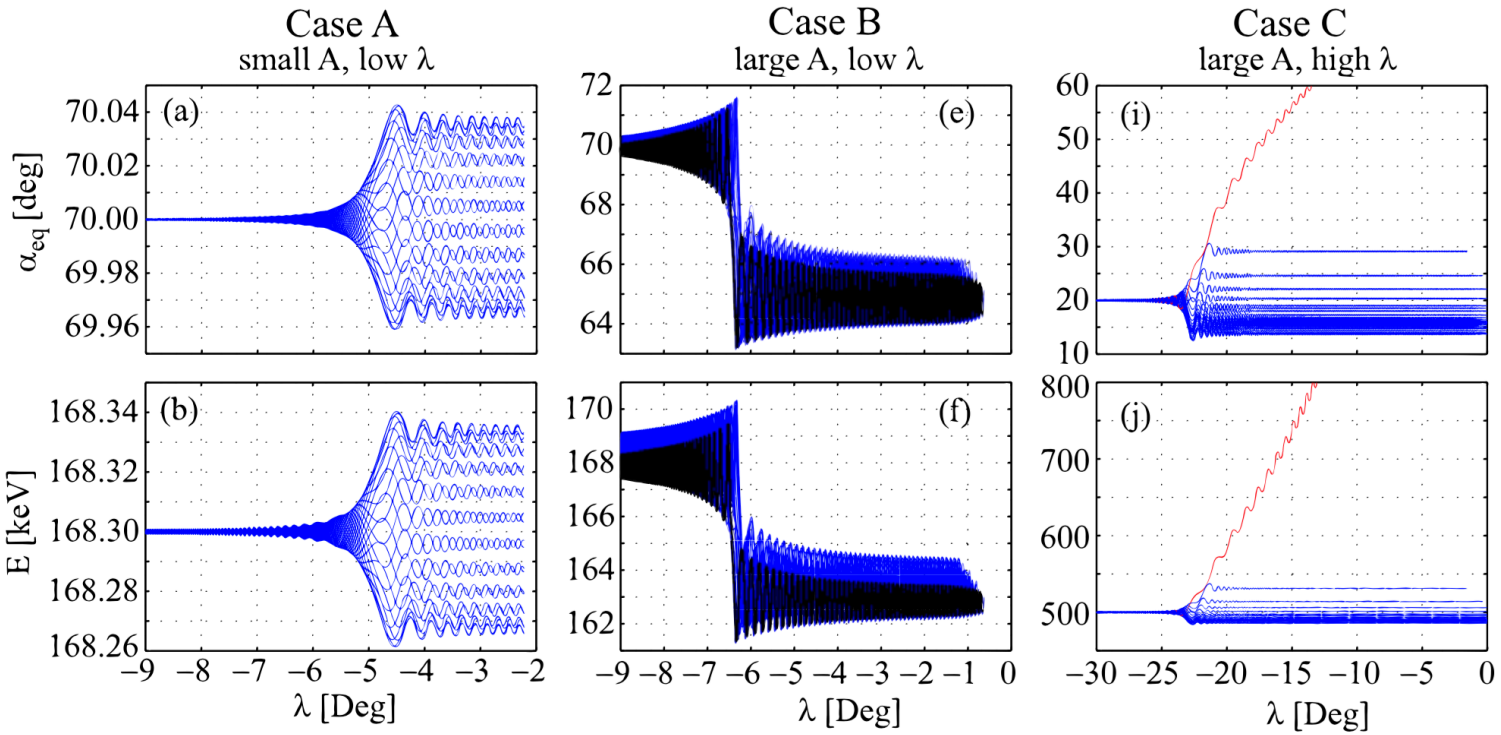

Figure 1.7: The trajectories of moderate pitch angle electrons interacted with coherent whistler mode waves along the magnetic field [*Bortnik et al.*, 2008].

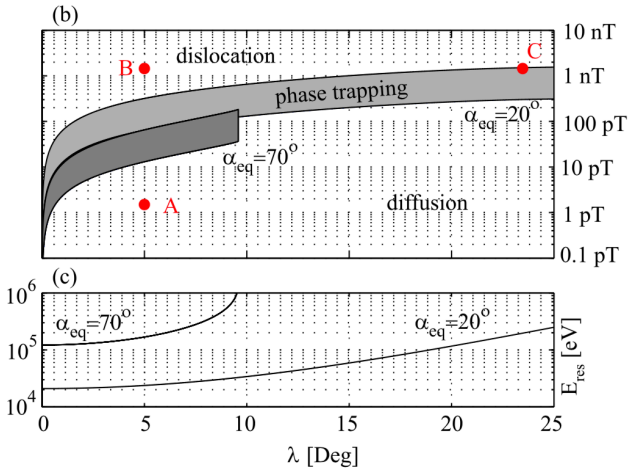

Figure 1.8: The categorization of wave particle interaction by the ration between the gradient of the ambient magnetic field and wave intensity at $L = 5$ [*Bortnik et al.*, 2008].

1.5 Wave-Particle Interaction Analyzer (WPIA)

On the JAXA satellite mission Exploration of energization and Radiation in Geospace (ERG), a software-type Wave-Particle Interaction Analyzer (WPIA) is installed to directly and quantitatively detect wave-particle interactions between whistler mode chorus emissions and energetic electrons [Miyoshi et al., 2012]. The WPIA is a new instrument proposed by Fukuhara et al. (2009) and measures the relative phase angle between the wave magnetic field vector and the velocity vector of each particle so as to calculate the energy exchange between waves and particles [Katoh et al., 2013]. The onboard processing by the software-type WPIA is not real-time. All velocity vectors of detected particles and waveforms of electromagnetic fields measured in a certain time interval will be once stored to the onboard memory, and later the onboard CPU reads out the stored data and conducts computations. The WPIA is important because this method enables us to measure the

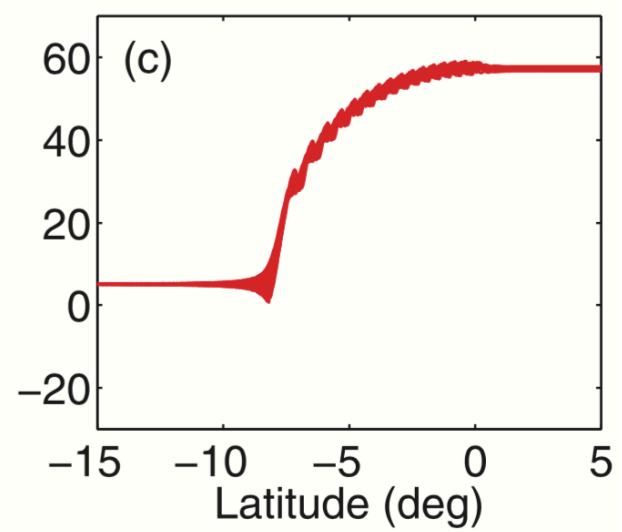

Figure 1.9: The trajectories of low pitch angle electrons interacted with coherent whistler mode waves along the magnetic field [after *Li et al.*, 2015]. The vertical axis indecate pitch angle of electrons at the magnetic equator.

energy exchange regardless of whether the physical process governing wave-particle interactions in the observed phenomenon is linear, quasi-linear, or nonlinear. Ergun et al. (1991) also introduced the concept of measuring wave-particle interactions using the Wave-Particle Correlator (WPC) but they measured only the correlation between the particle distribution and the waveform of electrostatic waves. The WPIA differs from the WPC because it measures not only the phase relation of particles with respect to the waveform but also a specific physical quantity derived from the computation of the measured wave electromagnetic field and velocity vectors. As a measurable value obtained by the WPIA, Fukuhara et al. (2009) introduced $I = q \sum_i \boldsymbol{E}_w(t_i) \cdot \boldsymbol{v}_i$, where q, v_i, t_i, and $\boldsymbol{E}_w$ are the charge, velocity, and timing of the detection of the $i-$th particle, and the wave electric field vector as a function of time, respectively. The I value is the accumulated value of the time variation of the kinetic energy of particles. Katoh et al. (2013)

formulated the I value as the Joule heat of resonance particles gained from plasma waves, which is expressed as $W = \iiint q\boldsymbol{E}_w(t) \cdot \boldsymbol{v} f(\boldsymbol{v}) \mathrm{d}\boldsymbol{v}$. For direct measurement of pitch angle scattering, we should consider another physical value to measure using the WPIA.

1.6 Purpose of this thesis

Pitch angle scattering of electrons and protons caused by chorus emissions and EMIC waves containing rising tones in frequency, respectively, are essentially nonlinear wave-particle interaction processes. However, there has not been sufficient direct detection in the observational study. Furthermore, the theoretical understanding of pitch angle scattering is also not sufficient. The general purposes of this thesis are to establish the method of direct detection of nonlinear pitch angle scattering and to understand the basic process of nonlinear pitch angle scattering using simulation and observation data. In chapter 2, we focus on the pitch angle scattering of electrons caused by chorus emissions in the simulation system, and we propose a method method to directly detect pitch angle scattering of energetic particles caused by plasma waves. Moreover, we show the utility of the proposed method by comparing simulation and observation data. In chapter 3, we focus on the the pitch angle scattering of energetic ions caused by rising tone EMIC waves observed by THEMIS satellites, and apply the proposed method of WPIA to detect the pitch angle scattering. Through analyzing the observation data, we evaluate the pitch angle scattering quantitatively from observation using our proposed method. In chapter 4, we investigate to understand the basic mechanism of nonlinear pitch angle scattering, especially low pitch angle electrons closely related to the auroral precipitation. Using test particle simulation data, we

clarify and evaluate the scattering process theoretically.

Chapter 2

Method for direct detection of pitch angle scattering of energetic particles caused by plasma waves

In this chapter, we propose a method of directly and quantitatively detecting pitch angle scattering of energetic particles caused by plasma waves using the WPIA. First, in section 1, we formulate the measurable value for detecting pitch angle scattering using the momentum variation of particles and wave electromagnetic fields. Next, we briefly describe simulation results of the generation of chorus emissions [Katoh and Omura, 2007a, b] in section 2, and we evaluate the feasibility of the proposed method by conducting a pseudo-observation of the simulation results using the WPIA in section 3. In section 4, we discuss in-situ measurements by the proposed method in the magnetosphere. Section 5 summarizes this study.

2.1 Measurable values of the WPIA

In this section, we derive the measurable values of the WPIA for pitch angle scattering of plasma particles by plasma waves. The pitch angle α is defined as

$$\alpha = \tan^{-1}\left(\frac{v_\perp}{v_\parallel}\right) = \tan^{-1}\left(\frac{p_\perp}{p_\parallel}\right), \tag{2.1}$$

where $v_\perp$ and $v_\parallel$ are the perpendicular and parallel components of the velocity vector $\boldsymbol{v}$ of a particle, respectively, and $p_\perp$ and $p_\parallel$ are the perpendicular and parallel components of the momentum vector $\boldsymbol{p}$, given by $\boldsymbol{p} = m\gamma\boldsymbol{v}$, respectively. Further, m and γ are the rest mass of the particle and the Lorentz factor, respectively. In this study, we define the pitch angle of particles in a range from 0 to 180°.

Differentiating both sides of equation (2.1), we obtain the following equations:

$$\frac{\mathrm{d}\alpha}{\mathrm{d}t} = \frac{1}{p}\left(\frac{\mathrm{d}p_\perp}{\mathrm{d}t}\cos\alpha - \frac{\mathrm{d}p_\parallel}{\mathrm{d}t}\sin\alpha\right) = \frac{1}{p}\frac{\mathrm{d}\boldsymbol{p}}{\mathrm{d}t}\cdot\boldsymbol{e}_\alpha, \tag{2.2}$$

where $p = |\boldsymbol{p}|$, and $\boldsymbol{e}_\alpha$ is a unit vector in the direction of increasing pitch angle (see Figure 2.1); $\boldsymbol{e}_\alpha$ is defined as

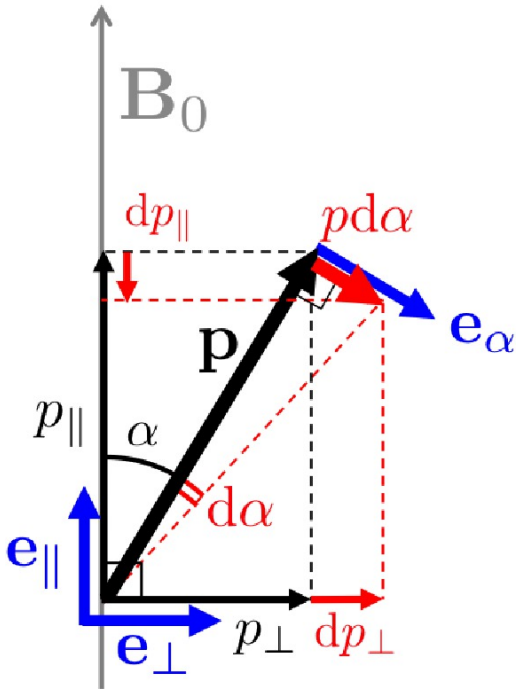

Figure 2.1: Geometric relationships among $\boldsymbol{p}$, $\boldsymbol{e}_{\parallel}$, $\boldsymbol{e}_{\perp}$, and $\boldsymbol{e}_{\alpha}$. Note that all vectors in this figure are defined in the $p_{\parallel}$–$p_{\perp}$ plain.

$$\boldsymbol{e}_{\alpha} = \boldsymbol{e}_{\perp} \cos\alpha - \boldsymbol{e}_{\parallel} \sin\alpha. \tag{2.3}$$

Equation (2.2) shows that the variation of the pitch angle with time is equal to the component of the time differentiation of the momentum along $\boldsymbol{e}_{\alpha}$. Because the time variation of the momentum is equal to the force acting on a particle, the pitch angle variation caused by wave-particle interaction is expressed by the Lorentz force due to wave electromagnetic fields. Equation (2.2) is rewritten as

$$F_{\alpha} = q\left(\boldsymbol{E}_{w} + \boldsymbol{v} \times \boldsymbol{B}_{w}\right) \cdot \boldsymbol{e}_{\alpha} = p\frac{\mathrm{d}\alpha}{\mathrm{d}t}. \tag{2.4}$$

Because the magnitude of the momentum p of a particle depends on the ki-

netic energy K as described by $K = \sqrt{p^2c^2 + m^2c^4} - mc^2$, we should consider that the significance of the same F_α changes depending on its kinetic energy. If we choose particles in a certain kinetic energy range, we can treat p as constant and F_α as simply indicating the pitch angle component of the force acting on the particles.

Katoh et al. (2013) formulated the measurable value of the WPIA for determining the energy exchange between waves and particles as the moment of the velocity distribution function about the energy exchange $\frac{\mathrm{d}K}{\mathrm{d}t}$, which represents the Joule heat. Following Katoh et al. (2013), we define G as the moment of the velocity distribution function $f(\boldsymbol{v}, t)$ about the Lorentz force by the wave electromagnetic field acting on particles, which is expressed as

$$G = \iiint q\left(\boldsymbol{E}_w + \boldsymbol{v} \times \boldsymbol{B}_w\right) \cdot \boldsymbol{e}_\alpha f(\boldsymbol{v}, t) \mathrm{d}\boldsymbol{v}. \tag{2.5}$$

G is the pitch angle component of the momentum exchanged from waves to particles during a unit time; in other words, G represents the accumulated momentum of the resonant particles in the direction of varying pitch angle during a unit time. If $G > 0$, the particles gained momentum from waves in the direction of increasing pitch angle, and if $G < 0$, the particles gained momentum in the direction of decreasing pitch angle. Note that the time variation of the pitch angle is also caused by the ambient magnetic field, but, considering the Lorentz force caused by the wave electromagnetic field, G shows only the pitch angle variation due to wave-particle interactions.

To discriminate scattered particles from other particles, we define g as a function of $\boldsymbol{v}$ and time:

$$g(\boldsymbol{v}, t) = q\left(\boldsymbol{E}_w + \boldsymbol{v} \times \boldsymbol{B}_w\right) \cdot \boldsymbol{e}_\alpha f(\boldsymbol{v}, t). \tag{2.6}$$

G is expressed in terms of g as

$$G = \iiint g(\boldsymbol{v}, t) \mathrm{d}\boldsymbol{v}. \tag{2.7}$$

Because g is the distribution of the amount of momentum exchange in the direction of varying pitch angle, $g(\boldsymbol{v}, t)$ shows the time and the location in velocity space at which momentum is effectively exchanged between waves and particles. Because we define the pitch angle in a range from 0 to 180°, positive g in the range from 0 to 90° and negative g in the range from 90 to 180° shows that particles are moving away from the loss cone, and negative g in the range from 0 to 90° and positive g in the range from 90 to 180° shows that particles are moving toward the loss cone.

Practically, we calculate the g values from data for a finite number of particles. Let N be the number of particles in a finite energy range, in a finite solid angle range, and in a finite time interval in a unit area. Then the g value calculated from discrete data in energy-pitch angle space is expressed as

$$g(K, \alpha, t) = \frac{1}{2\pi \sin\alpha \Delta K \Delta\alpha \Delta t} \frac{m^2}{K} \frac{\gamma^5}{\gamma + 1} \frac{1}{\boldsymbol{n} \cdot \hat{\boldsymbol{v}}} \sum_{\substack{K \le K_i \le K + \Delta K \\ \alpha \le \alpha_i \le \alpha + \Delta\alpha \\ t \le t_i \le t + \Delta t}}^{N} (F_\alpha)_i, \tag{2.8}$$

where m, $\boldsymbol{n}$, and $\hat{\boldsymbol{v}}$ are the rest mass of the particles, the normal vector to the detection plane, and a unit vector in the direction of $\boldsymbol{v}$, respectively, and

$$(F_\alpha)_i = q \left(\boldsymbol{E}_w(t_i) + \boldsymbol{v}_i \times \boldsymbol{B}_w(t_i) \right) \cdot (\boldsymbol{e}_\alpha)_i, \tag{2.9}$$

where i is the particle index, and t_i is the time at which the i-th particle is detected. For the details of the derivation of equation (2.8), see the Appendix.

If the waves scatter the pitch angle of electrons and then the distribution function f in the ϕ direction is modulated on a time scale corresponding to the wave frequency, g integrated over ϕ is expected to show a significant value. In contrast, if there are no wave-particle interactions, g is negligible small.

The g value contains statistical fluctuations because it is calculated by accumulating a finite number of particles. According to the central limit theorem, because we can assume that the accumulated g follows a normal distribution function, we can estimate the fluctuation of the g value by evaluating the standard deviation of the distribution, which is given by

$$\sigma_g(K,\alpha,t) = \Lambda \sqrt{\sum_{\substack{K\le K_i\le K+\Delta K\\ \alpha\le\alpha_i\le\alpha+\Delta\alpha\\ t\le t_i\le t+\Delta t}}^{N} \left((F_\alpha)_i\right)^2 - \frac{1}{N}\left(\sum_{\substack{K\le K_i\le K+\Delta K\\ \alpha\le\alpha_i\le\alpha+\Delta\alpha\\ t\le t_i\le t+\Delta t}}^{N} (F_\alpha)_i\right)^2}, \qquad (2.10)$$

where Λ is expressed as

$$\Lambda = \frac{1}{2\pi\sin\alpha\Delta K\Delta\alpha\Delta t}\frac{m^2}{K}\frac{\gamma^5}{\gamma+1}\frac{1}{\boldsymbol{n}\cdot\hat{\boldsymbol{v}}}. \qquad (2.11)$$

As the relation between G and g is expressed by equation (2.7), we can also calculate the G values from discrete particle data using the following equation:

$$G = \sum_{K,\alpha} g(K,\alpha,t)\frac{2\pi v\sin\alpha}{\gamma^3}\Delta K\Delta\alpha. \qquad (2.12)$$

According to the law of error propagation, we can also evaluate the statistical fluctuation of G as σ_G:

$$\sigma_G = \sqrt{\sum_{K,\alpha} \left(\sigma_g(K,\alpha,t) \frac{2\pi v \sin\alpha}{\gamma^3} \Delta K \Delta\alpha \right)^2}. \tag{2.13}$$

Therefore, by calculating the G values with σ_G, we can detect whether the particle population gains momentum in the direction of varying pitch angle because of pitch angle scattering caused by plasma waves, and by evaluating the g values with the uncertainty σ_g, we can clarify the energy and pitch angle range that are scattered.

For purely parallel propagating electromagnetic waves, we use the following conditions.

$$\boldsymbol{E}_w \perp \boldsymbol{B}_w, \quad \boldsymbol{B}_w \perp \boldsymbol{v}_\parallel, \quad \boldsymbol{E}_w \perp \boldsymbol{v}_\parallel, \tag{2.14}$$

and $\boldsymbol{v}_\perp$ exists in the $\boldsymbol{E}_w$-$\boldsymbol{B}_w$ plane. The relative phase angle ζ is defined as the angle between $\boldsymbol{B}_w$ and $\boldsymbol{v}_\perp$ (see Figure 2.2). Using ζ and equation (2.3), we can rewrite equation (2.9) as

$$\begin{aligned}(F_\alpha)_i &= q\left(\boldsymbol{E}_w(t_i) + \boldsymbol{v}_i \times \boldsymbol{B}_w(t_i)\right) \cdot \left(\boldsymbol{e}_\perp \cos\alpha_i - \boldsymbol{e}_\parallel \sin\alpha_i\right) \\ &= q \sin\zeta_i (-E_w(t_i)\cos\alpha_i + v_{\parallel i} B_w(t_i)\cos\alpha_i + v_{\perp i} B_w(t_i)\sin\alpha_i). \end{aligned} \tag{2.15}$$

For pitch angle scattering of electrons, the first term on the right side of equation (2.15) describes the pitch angle increase ($\frac{\mathrm{d}\alpha}{\mathrm{d}t} > 0$) caused by the increase in $v_\perp$ due to the Coulomb force of the wave electric field. The second term describes the pitch angle variation caused by the increase in $v_\perp$ due to the perpendicular component of the Lorentz force of the wave magnetic field. The third term describes the pitch angle variation caused by the decrease in $v_\parallel$ due to the parallel component of the Lorentz force of the wave magnetic

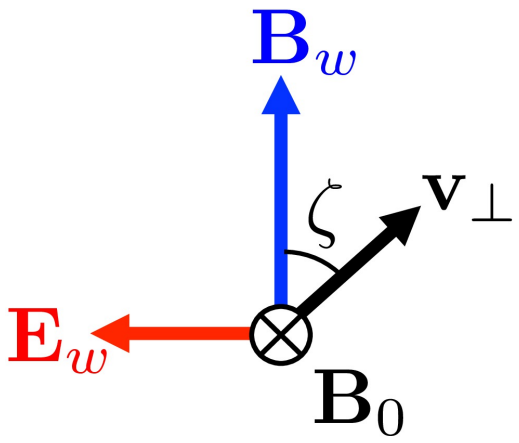

Figure 2.2: Definition of relative phase angle ζ.

field. Because G and g calculated from equation (2.15) depends on ζ, the modulation of the velocity distribution function in ζ results in significant G and g. In other words, the G and g show identically zero for the case of the gyro-tropic velocity distribution function and we cannot detect the diffusion type pitch angle scattering (e.g., quasi-linear diffusion with assumption of $\frac{\partial f}{\partial \phi} = 0$, where ϕ is the gyro-phase) by calculating G and g. In this study, using equation (2.15) for G and g, we apply the method to simulation results of purely parallel propagating whistler-mode waves generated by energetic electrons. The details of the data set are described in the next section.

2.2 Simulation

Katoh et al. (2013) studied the feasibility of the WPIA by conducting a pseudo-observation of a simulation result reproducing the chorus generation process [Katoh and Omura, 2007a]. Following the method used in Katoh et al. (2013) we analyzed the simulation results in order to evaluate the feasibility of the method proposed in the previous section. By a spatially one-dimensional electron hybrid simulation in an inhomogeneous ambient mag-

netic field, Katoh and Omura (2007a, b) reproduced the generation process of whistler-mode chorus emissions in the region close to the magnetic equator. Chorus emissions emerge from a band of whistler-mode waves excited by an instability driven by a temperature anisotropy of energetic electrons and are generated by nonlinear wave-particle interactions [Omura et al., 2008, 2009]. The initial distribution function of anisotropic energetic electrons is given by the loss cone distribution constructed by summing the bi-Maxwellian distributions. The characteristics of the chorus generation process have been studied using the results of electron hybrid simulations [Katoh and Omura, 2007a, b, 2011, Katoh et al., 2008, 2013; Omura et al., 2008, 2009]. In this simulation, the free energy in generating chorus is mainly supplied by a few hundred keV electrons Katoh et al. (2013), which is higher than the typical energy range discussed in previous studies. This is because the limited computational resources prevent us to use the realistic velocity distribution of energetic electrons as well as the spatial gradient of the background magnetic field in the simulation system. For the details of the numerical scheme and initial conditions used in the simulation, see Katoh and Omura (2007a, b).

We analyzed the result of a simulation conducted using the same parameters as in [Katoh and Omura, 2007a, b]. Two pseudo-observation points were fixed in the simulation box at $h = \pm 200\ c\Omega_e^{-1}$, corresponding to the locations at which the magnetic latitude is about $\pm 8^\circ$ at $L = 4$, where c and Ω_e are the speed of light and cyclotron frequency of electrons, respectively. We analyzed the wave electromagnetic fields at these points and the velocity of particles that passed through them at each time step. Because the simulation system is spatially one-dimensional, waves generated in the simulation are in the field-aligned propagation mode and are purely electromagnetic.

Therefore, we used four components of the wave electromagnetic fields (E_x, E_y, B_x, and B_y), which are perpendicular to the ambient magnetic field $\boldsymbol{B}_0$, in the analysis. The velocity of the particles is computed in three dimensions; therefore, we used three velocity components (v_x, v_y, and v_z) detected at each time step. Henceforth, the points at $h = +200\ c\Omega_e^{-1}$ and $h = -200\ c\Omega_e^{-1}$ are called points A and B, respectively.

2.3 Results

Figures 2.3 (a) and (b) show wave magnetic field spectra at the fixed points A and B, respectively. Rising tone chorus emissions are reproduced in the simulation system. In this simulation, chorus emissions are generated from the initial thermal noise of energetic electrons near $h = \pm 0\ c\Omega_e^{-1}$, corresponding to the magnetic equator, and propagate away from the equator as their amplitude increases nonlinearly [Katoh and Omura, 2007a].

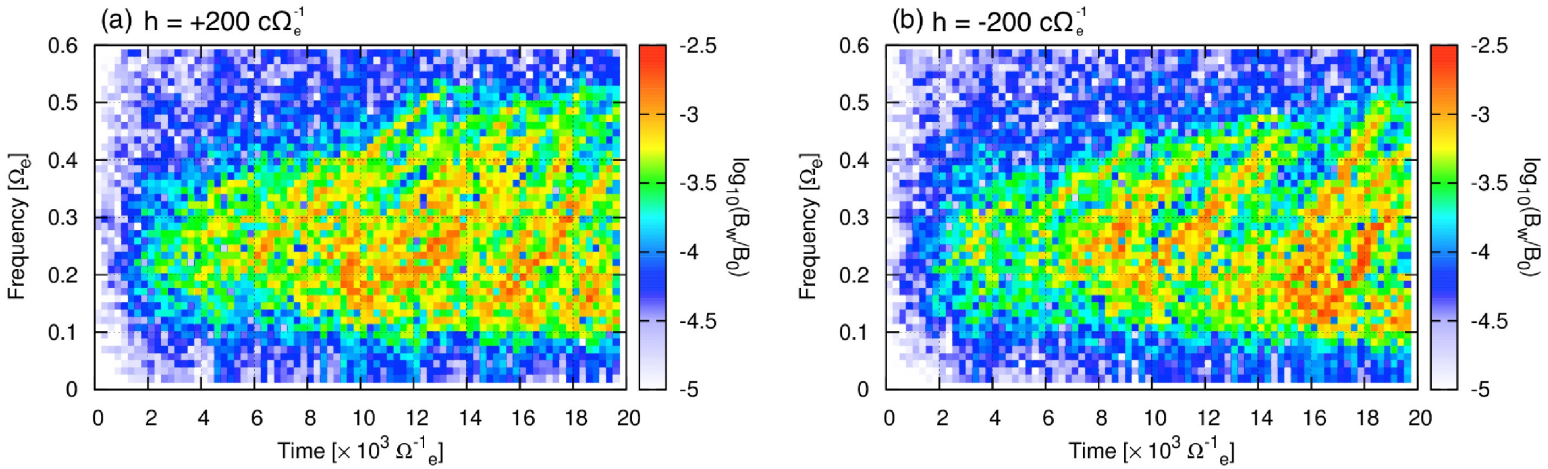

Figure 2.3: Wave magnetic field spectra measured at fixed points in the simulation system.

Figures 2.4 (a) and (b) show the evolution of the pitch angle distribution of electrons in the kinetic energy range of 180–220 keV at points A and B, respectively. Figures 2.5 (a) and (b) show the temporal variation of the distributions shown in Figures 2.4 (a) and (b) at each time interval, given by $[f(t,\alpha) - f(t-\Delta t,\alpha)]/f(t,\alpha)$, for points A and B, respectively. $\Delta\alpha$ and Δt are 1° and 500 Ω_e^{-1}, respectively. Warm and cool colors indicate that the pitch angle distribution is increasing and decreasing, respectively, relative to the distribution in the previous time interval. We find streaky oblique lines in the temporal variation of the pitch angle distribution [Figures 2.5 (a) and (b)]. The time step at which the lines appeared and the duration of each line correspond closely to those of rising tones appearing in the wave spectra. These results suggest that the variations in the pitch angle distribution are caused by chorus emissions generated in the simulation result. However, the amount of variation in the pitch angle distribution is almost always less than several percent of the total pitch angle distribution. Furthermore, the time variation of the pitch angle distribution and the difference between the distributions at points A and B are similar to each other, because the variation of the pitch angle distribution at a point is the result of modulation by waves not only at that point but also at different points along the trajectory of energetic electrons bouncing in the simulation system. Therefore, even if modulation of the distribution is detected at the fixed point, it is difficult to conclude where the pitch angle distribution is modulated by waves.

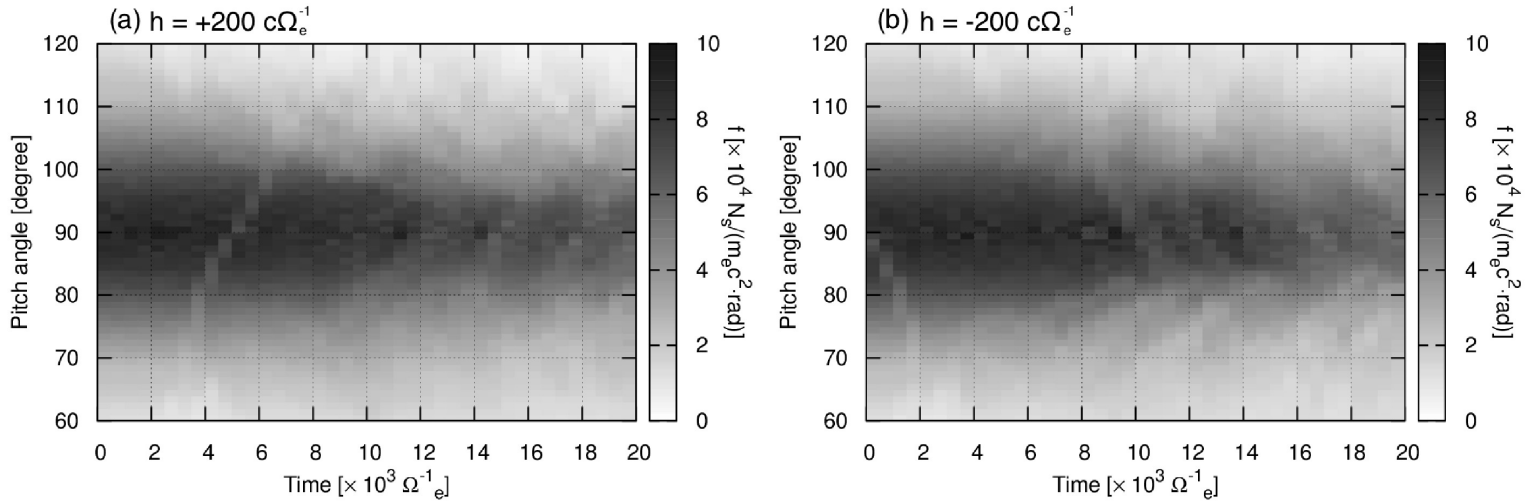

Figure 2.4: Temporal variation of the pitch angle distribution $f(t, \alpha)$ measured at fixed points in the simulation system. The pitch angle distribution at each time step is normalized by the initial pitch angle distribution at 90°. The unit of the distribution function N_s is the weight of a superparticle for the hot electron density in this simulation system.

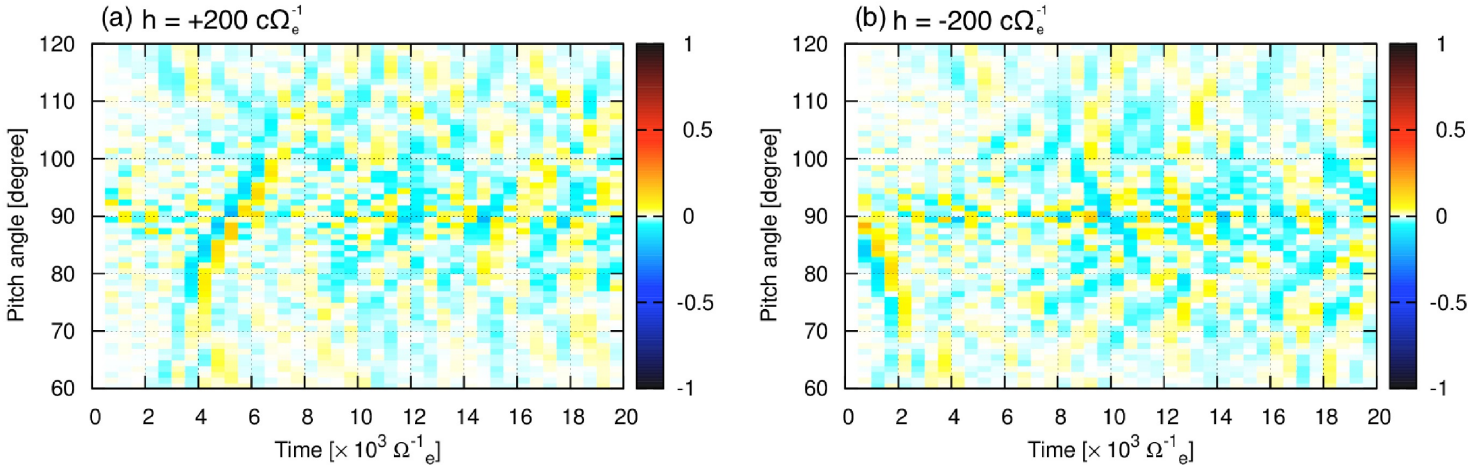

Figure 2.5: Temporal variation of each time interval of the pitch angle distribution $[f(t,\alpha) - f(t-\Delta t,\alpha)]/f(t,\alpha)$ measured at fixed points in the simulation system. The pale colors (yellow and cyan) indicate several percent ($< 10\%$) modulation of the pitch angle distribution. Relatively large variation starting at 90° at $h = -200\ c\Omega_e^{-1}$ is artificial modulation due to the lack of the initial distribution at $\alpha = 90^\circ$ in the southern hemisphere in the simulation system.

Figures 2.6 (a) and (b) shows the time history of G integrated using energetic electrons in the entire velocity space. Figure 2.6 (a) indicates that energetic electrons gain momentum in the direction of increasing pitch angle; namely, the pitch angle of electrons tends to increase toward 180° at point A. In contrast, at point B, Figure 2.6 (b) shows that the pitch angle of electrons tends to decrease toward 0°. By comparing Figures 2.6 and 2.3, we see that the G values indicate that the momentum of electrons in the direction of varying pitch angle tends to change with chorus emissions when the wave amplitude is larger. Furthermore, in the linear growth phase that is the initial stage of this simulation ($0 < t < 2500\Omega_e^{-1}$ [Omura et al., 2008; Katoh and Omura, 2011]), G at point A and B show weak but statistically significant values with sufficiently long accumulation time. These results indicate that the proposed method of measuring G has capability to detect the weak linear interactions.

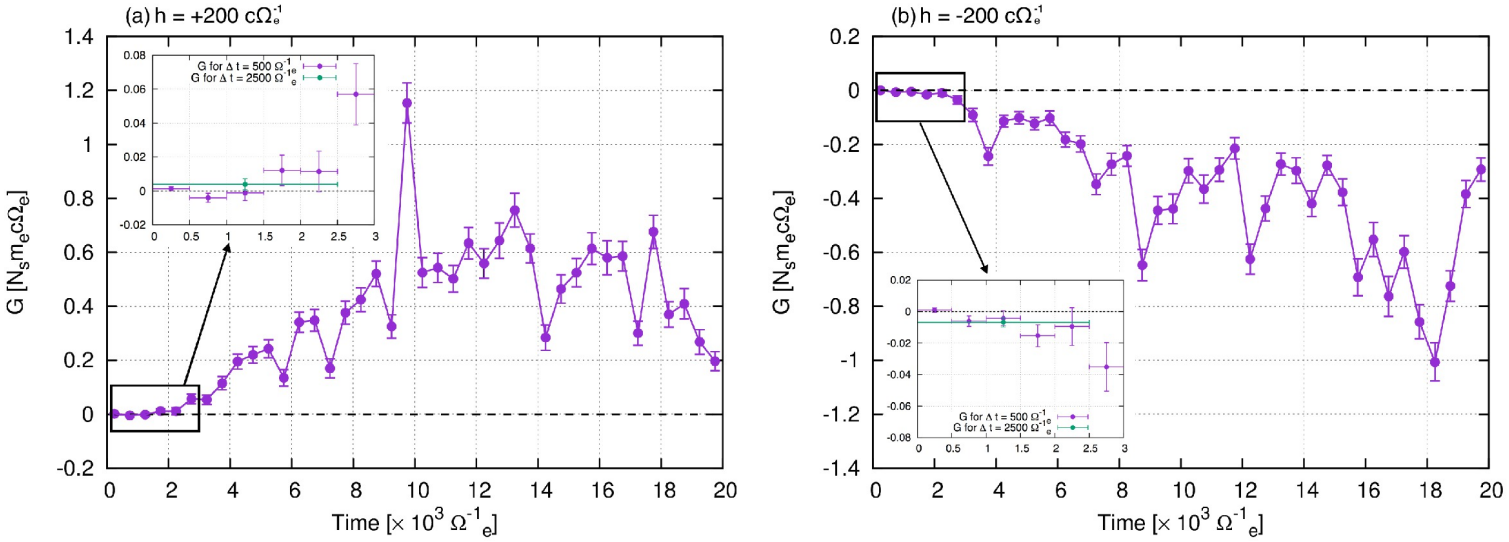

Figure 2.6: Temporal variation of G with σ_G detected at fixed points in the simulation system.

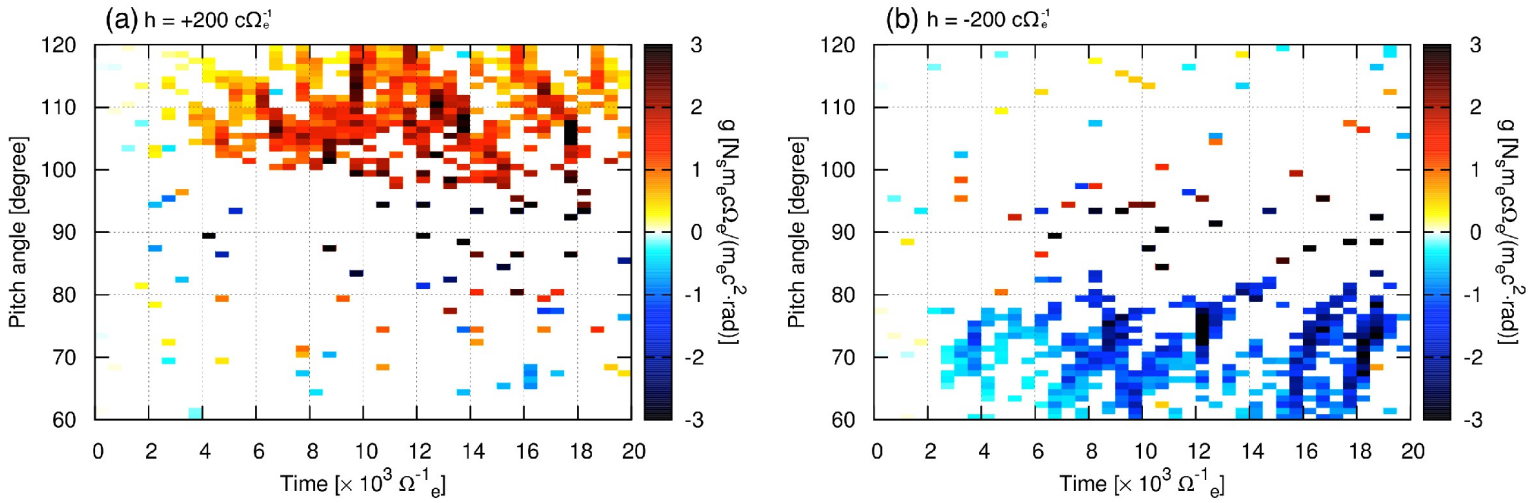

Figure 2.7: Temporal variation of g as a function of pitch angle at $K = 200 \pm 20$ keV. To show the statistically significant values, we plot only the g values satisfying the condition $g > 2\sigma_g$.

Figures 2.7 (a) and (b) show the g values obtained at each time interval in the corresponding pitch angle range. We use energetic electrons in the same energy range as in Figures 2.4 and 2.5, and we plot only the g values satisfying the condition $g > 2\sigma_g$ in order to show the statistically significant results. Warm and cool colors indicate pitch angle increases and decreases, respectively. At point A in the northern hemisphere, we obtained positive g values at pitch angles greater than 90°. On the other hand, we obtained negative g values at pitch angles less than 90° at point B in the southern hemisphere. Although we found similar variations in the pitch angle distribution at points A and B (see Figure 2.4), Figures 2.7 (a) and (b) clearly differentiate the pitch angle range in which significant pitch angle scattering occurred at points A and B. These results reveal that the g values successfully clarified the location at which pitch angle scattering occurred and the pitch angle range in which energetic electrons are effectively scattered by the waves.

Figures 2.8 (a) and (b) show the g values in K–α space calculated at points A and B, respectively. In the result shown in Figure 2.8, we used particles detected in the entire simulation time, which corresponds to the time interval from 0 to 20,000 Ω_e^{-1}. The color bar in Figure 2.8 is the same as that in Figure 2.7. Black solid lines in Figure 2.8 are the resonance curves corresponding to each frequency, which are expressed as

$$\omega - kv\cos\alpha = \frac{\Omega_e}{\gamma}, \tag{2.16}$$

where ω and k are the wave angular frequency and wave number, respectively. According to Katoh and Omura (2007a), electrons at energies from 100 keV to several hundreds of keV generate whistler-mode chorus emissions, and MeV electrons are accelerated by chorus emissions. Figures 2.8 (a) and (b)

indicate that electrons at kinetic energies from 100 keV to a few MeV are strongly scattered, and their pitch angle shifts away from 90°.

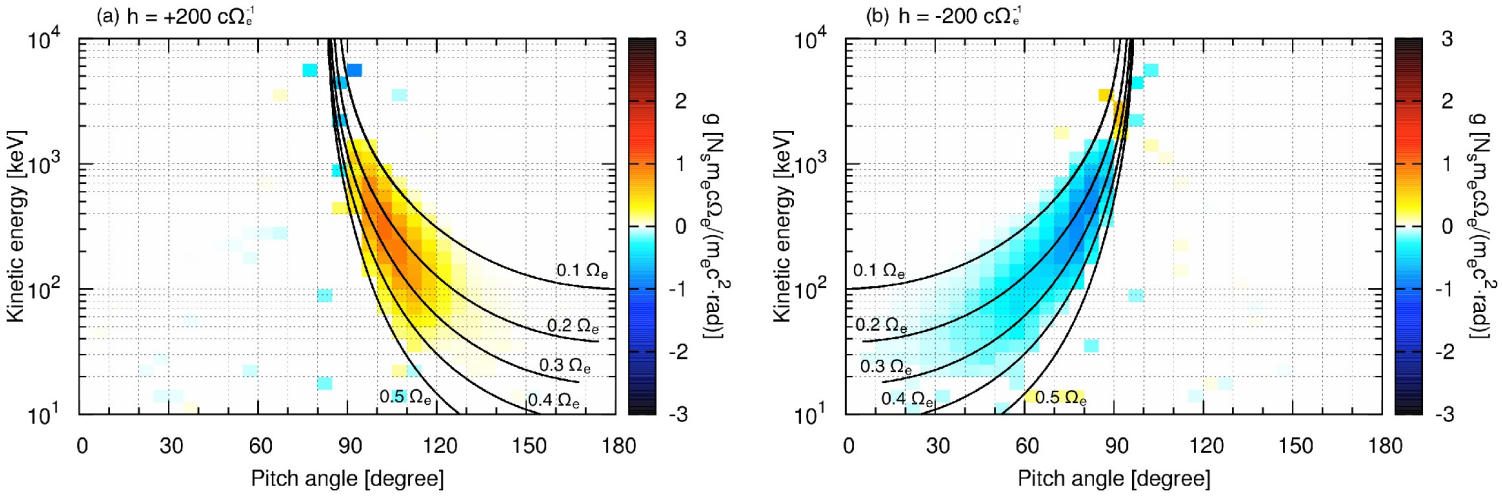

Figure 2.8: The g values in the K–α space calculated at fixed points over the time interval from 0 to 20,000 Ω_e^{-1}. Black solid lines in both panels are the resonance curves corresponding to each frequency.

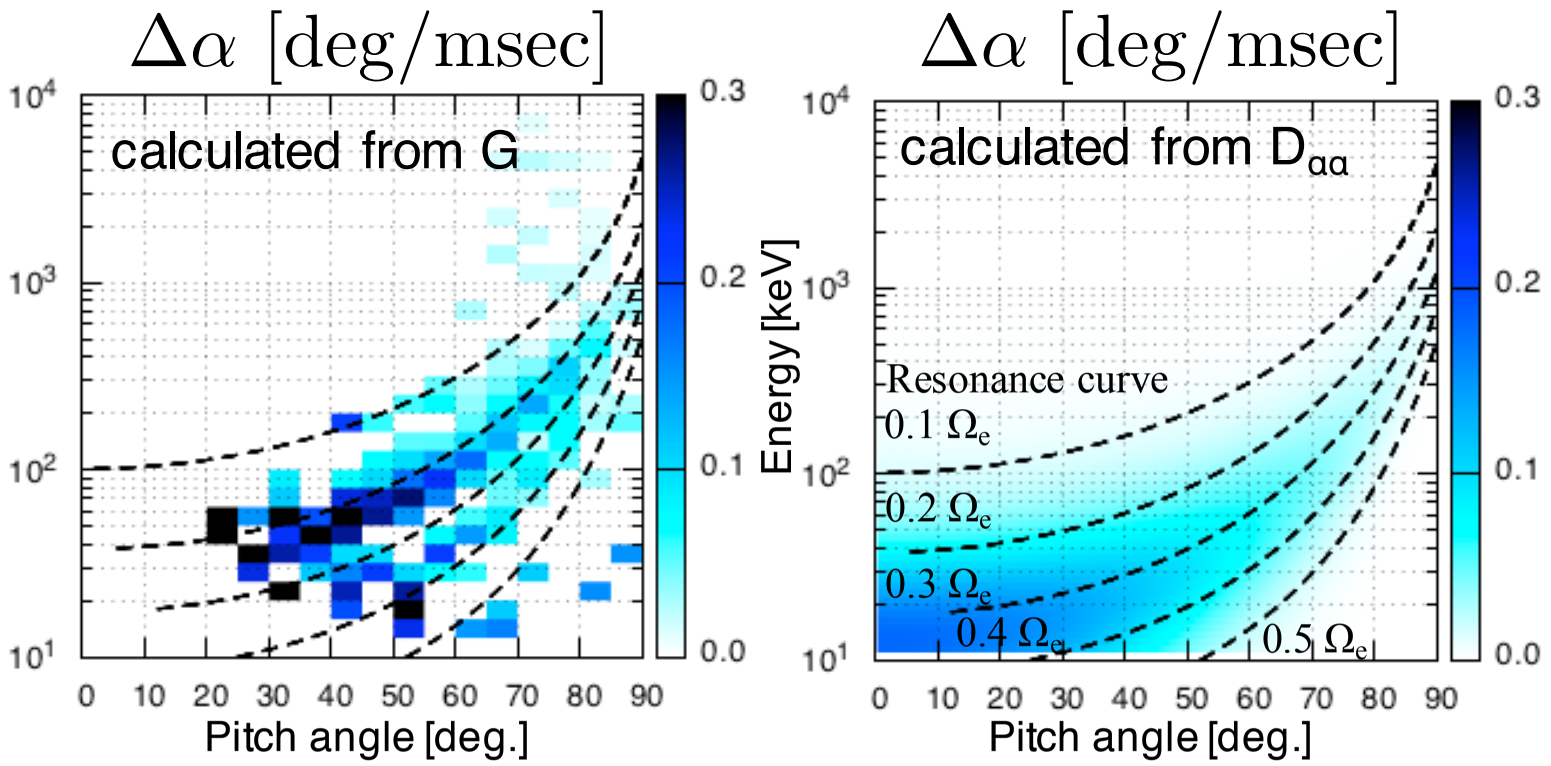

Figure 2.9: $\Delta\alpha$ in the K–α space calculated from G(left) and $D_{\alpha\alpha}$(right) with resonance curve in the period of 11000 $\Omega_e^{-1} < t <$ 12000 Ω_e^{-1}.

2.4 Discussion

We examine the resonance condition using the parameters in the simulation. For $k > 0$ (northward propagation), waves in the frequency range $0.1 < \omega/\Omega_e < 0.5$ can resonate with electrons having a kinetic energy of 200 keV and pitch angle range of $93^\circ < \alpha < 118^\circ$. For $k < 0$ (southward propagation), waves in the frequency range of $0.1 < \omega/\Omega_e < 0.5$ can resonate with 200 keV electrons in the pitch angle range of $62^\circ < \alpha < 87^\circ$. The pitch angle ranges in which statistically significant g values are obtained in Figure 2.7 are consistent with these estimations of the resonance condition, and the statistically significant g values in Figure 2.8 are also consistent with the resonance conditions for each frequency (black lines in Figure 2.8). Namely, we can discriminate scattered particles and other particles by measuring the g values at the observation point at the observation time. According to the Figure 6, we can detect the small G value with statistical significance during the initial linear phase at the both points in this simulation. This result indicates that the velocity distribution function tends to be non-gyrotropic and there should be non-negligible nonlinear effect even at the initial phase of simulation, as is just discussed in the section 2.

From the g values and the velocity distribution f, we can calculate $\langle F_\alpha \rangle = g/f$, that is, the average Lorentz force for detected particles during a time interval, and we can also estimate the averaged pitch angle variation $\left\langle \frac{\mathrm{d}\alpha}{\mathrm{d}t} \right\rangle = \langle F_\alpha \rangle / p$. In the duration of $12,000\ \Omega_e^{-1} < t < 14,000\ \Omega_e^{-1}$ at $\alpha = 110^\circ$, the averaged g value is 2.0 $N_s m_e c \Omega_e / (m_e c^2 \cdot \mathrm{rad})$, and $\langle F_\alpha \rangle$ is 0.00010 $m_e c \Omega_e$ because $f \sim 20000\ N_s/(m_e c^2 \cdot \mathrm{rad})$. Because $p = 0.97\ m_e c$ for $K = 200$ keV, we estimate $\left\langle \frac{\mathrm{d}\alpha}{\mathrm{d}t} \right\rangle = 0.00010$ rad $\Omega_e = 0.036^\circ\ f_{ce}$, where f_{ce} is the cyclotron frequency, $f_{ce} = \Omega_e/(2\pi)$. Assuming $f_{ce} = 10$ kHz, which is a typical value of the cyclotron frequency at $L = 4$, the electrons are

scattered 0.36° in 1 ms. This result indicates that the energetic electrons that encounter chorus elements are instantaneously and strongly scattered by the chorus elements. Note that, according to Figures 2.7 (a) and (b), instantaneous pitch angle scattering occurs only during a short time interval corresponding to the encounter of chorus elements and resonant particles in a limited pitch angle range. This result also clarifies that by calculating the g values, we can quantitatively detect the intensity of pitch angle scattering.

In order to compare calculated g with theoretical predicted intensity of pitch angle scattering, we also calculated $D_{\alpha\alpha}$ that means the diffusion coefficient of pitch angle scattering using the method of Summers (2005) (see equation (1.13)). To compare g value to diffusion rate $D_{\alpha\alpha}$, we estimate averaged pitch angle variation calculated from both values. Since g value is summation of a Lorentz force of N particles, we should calculate averaged pitch angle variation using $\langle \Delta\alpha \rangle = g\Delta t/pN$. On the other hand, since $D_{\alpha\alpha}$ is defined as second order time differential of pitch angle, averaged pitch angle variation is calculated from square root of $D_{\alpha\alpha}$ expressed as $\langle \Delta\alpha \rangle = \sqrt{2D_{\alpha\alpha}\Delta t/p^2}$. Figure 2.9 shows $\langle \Delta\alpha \rangle$ in the energy-pitch angle space calculated from g and $D_{\alpha\alpha}$ with resonance curve in the period of 11000 $\Omega^{-1} < t <$ 12000 Ω^{-1}. Although the cyclotron frequency is a unit frequency in the simulation, to compare g with $D_{\alpha\alpha}$, we assume the cyclotron frequency is 10 kHz. This value is consistent with the observed value at the location of $L = 4$. Because calculation of $D_{\alpha\alpha}$ requires the assumption of diffusionfor the scattering process, $\langle \Delta\alpha \rangle$ from $D_{\alpha\alpha}$ shows weak, diffusive, and broad-band scattering in the energy-pitch angle space. On the other hand, $\langle \Delta\alpha \rangle$ from g indicates stronger scattering than expected from $D_{\alpha\alpha}$. We can conclude that g can detect the pitch angle scattering with nonlinearity of wave-particle interaction.

Table 2.1: Statistical detectability of wave–particle interactions at the point A. Note that μ and σ are calculated from g and σ_g detected at the fixed point A (corresponding to the northern hemisphere) in the simulation system during linear and nonlinear phase, respectively. In this paper, linear and nonlinear phase are defined as $t \leq 2500\ \Omega_e^{-1}$ and $t > 2500\ \Omega_e^{-1}$, respectively [(see Figure 4c corresponding to the Run 3 in Katoh and Omura (2011)). $N_{2\sigma}$, $N_{1\sigma}$, $\Delta t_{2\sigma}$, and $\Delta t_{1\sigma}$ are calculated from μ and σ.

	Region I (200 – 400 keV, 100 – 110 deg)		Region II (1-4 MeV, 85 – 90 deg)	
	linear phase ($t \leq 2500\ \Omega_e^{-1}$)	nonlinear phase ($t > 2500\ \Omega_e^{-1}$)	linear phase ($t \leq 2500\ \Omega_e^{-1}$)	nonlinear phase ($t > 2500\ \Omega_e^{-1}$)
μ $[m_e c\Omega_e]$	$+7.23 \times 10^{-7}$	$+3.82 \times 10^{-5}$	-3.61×10^{-7}	-4.52×10^{-6}
σ $[m_e c\Omega_e]$	1.69×10^{-4}	1.18×10^{-3}	2.05×10^{-4}	1.47×10^{-3}
$N_{2\sigma}$ [count]	271836	3819	1296091	424016
$N_{1\sigma}$ [count]	54459	955	324023	106004
$\Delta t_{2\sigma}$ [s]	43.6	0.76	259.2	84.8
$\Delta t_{1\sigma}$ [s]	10.9	0.19	64.8	21.2

A plasma particle instrument onboard a satellite in space measures a finite number of particles, and the number of particle counts per second is typically less than several thousand. In the simulation, the number of particles obtained at the fixed points is larger than those expected to be detected by particle instruments in a real space plasma. To quantitatively estimate the feasibility of the proposed method, we calculate the number of particle counts N_{need} required to obtain statistically significant values. Let μ and σ be the mean and standard deviation, respectively, of the gained momentum of particles in the direction of increasing pitch angle averaged over the entire simulation time. We can estimate N_{need} by assuming that the ratio of σ to μ in the simulation is equivalent to that in a real space plasma. For the condition $\mu \ll \sigma$, the accumulated value of g and the standard variation σ_g are expressed as $g = N\mu$ and $\sigma_g = \sqrt{N}\sigma$, respectively. Therefore, if we require the condition $|g| > 2\sigma_g$, N should be larger than $N_{2\sigma} = (2 \times \sigma/\mu)^2$, and if we require the condition $|g| > \sigma_g$, N should be larger than $N_{1\sigma} = (\sigma/\mu)^2$. We roughly estimate $N_{2\sigma}$ and $N_{1\sigma}$ using the particles detected at the fixed point A in two energy-pitch angle regions, I and II. We assume that region I covers the kinetic energy and pitch angle ranges of 200–400 keV and 100–110° and that region II covers the ranges of 1–4 MeV and 85–90° [see Figure 2.8 (a)]. Moreover, assuming that the count rate of particles in the corresponding energy range in real observations is constant in time and is 5000 count/s, we calculate accumulation time $\Delta t_{2\sigma}$ and $\Delta t_{1\sigma}$ corresponding to $N_{2\sigma}$ and $N_{1\sigma}$, respectively. Detected μ and σ, and calculated $N_{2\sigma}$, $N_{1\sigma}$, $\Delta t_{2\sigma}$, and $\Delta t_{1\sigma}$ in the each region are listed in the Table 2.1. As results of the estimation, to detect the pitch angle scattering caused by nonlinear interactions, we need to accumulate particles during 0.76 s for region I and 84.8 s for region II. In the case of linear interactions,

we have to accumulate particles during 43.6 s for region I and 259.2 s for region II to satisfy the condition $|g| > 2\sigma_g$. we can refer to this estimation to determine the time resolution of the WPIA measurement. Under the assumed conditions, we find that $\Delta t_{2\sigma}$ and $\Delta t_{1\sigma}$ are longer than the typical duration of one chorus element, approximately 0.1 s. Therefore, we can expect to measure the variation of the g values due to each chorus element, but it would be difficult to measure the temporal variation of the g values corresponding to the frequency variation of each chorus element, as we saw in Figures 2.7 (a) and (b). To measure the rapid variation of the g values, we need to realize a higher particle count rate so as to obtain statistically significant g values in a shorter time interval. However, we can expect to measure the variation of the g values corresponding to the duration of several chorus elements integrating over a few second. We conclude that we can apply the proposed method to the situation that tens of chorus elements are continuously emitted. For the weak wave-particle interactions like a linear phase in this simulation, we can also apply the proposed method, but we need longer accumulation time of particles, such as several tens of seconds, to detect statistically significant g.

The timescale of the interaction between whistler-mode chorus emissions and electrons is nearly equal to the time scale of the cyclotron motion, In order to realize the method proposed in the present study, for $f_{ce} \sim 10$ kHz and if we divide the relative phase angle ζ into 10 points, we need the time resolution better than tens of microseconds for the detection timing of each particle count of the particle instrument. The same time resolution is also required for the time synchronization between the wave and particle instrument. In addition, in the case of real space observation, the specification of the instruments on the satellite should be evaluated, for example, the resolution of solid angle, time, and energy of particles, the contamination level of

the particle detector, the accuracy of wave phase determination, and so on. Because the required accumulation time of the WPIA is proportional to the accumulation number of particles and the square of the ambiguity of each particles, the high count rate and the low ambiguity are also required for the real observation. For a particle instrument with a limited field of view, the pitch angle range covered during a typical duration of each chorus element ($\sim$ 0.1 s) will be very narrow. In order to cover the wide pitch angle range in the analysis, we need to use observation results measured during a certain time interval. On the other hand, we note that the relative phase angle ζ can be fully covered even if the field of view of a particle instrument is limited, because wave electromagnetic field vectors rotate in the time scale enough shorter than the spin period of the satellite (typically a few seconds).

The proposed method of using the WPIA enables us to identify where and when pitch angle scattering by plasma waves occurs and the energy and pitch angle ranges in which energetic particles are scattered. The WPIA measures only the momentum variation at the observation point without any assumption regarding the physical process governing the wave-particle interactions. The g values directly show whether wave-particle interactions occur at the site of the observation, but, using only the data from a single-point observation by the WPIA, it is difficult to calculate the time variation of the velocity distribution function of the particles.

In this study, we applied the proposed method to the interaction between electrons and whistler-mode chorus emissions, which are purely parallel propagating waves in the simulation. On the other hand, this method can be applied to various types of wave-particle interactions in space plasma. For example, obliquely propagating whistler-mode waves are expected to have a parallel component of the wave electric field. In this paper, we can obtain

only a perpendicular component of electric field due to limitation of simulation setting, on the other hand, we can detect the Landau-type pitch angle scattering by measuring g as calculated by equation (2.6) using the parallel component of the electric field of the waves. By dividing the wave electric field data into parallel and perpendicular components and calculate g, we can discuss which component of waves contributes to the pitch angle scattering more effectively.

2.5 Concluding remarks

We proposed a new method of detecting pitch angle scattering using the WPIA. The time variation of the pitch angle is formulated as the time variation of the momentum, which is the Lorentz force in the direction of increasing pitch angle, and the measurable value g is defined as the direction of varying pitch angle component of the lost momentum of the wave electromagnetic fields. We applied the proposed method to simulation results reproducing the generation of whistler-mode chorus emissions and evaluated the feasibility of the proposed method. Pseudo-observations at fixed points in the simulation system indicate that the time variation of the pitch angle distribution of electrons is very small, but the g values clearly show the statistically significant results of pitch angle scattering. The simulation results clarified that the proposed method enables us to identify the location at which pitch angle scattering occurs and the energy and pitch angle ranges in which energetic electrons are effectively scattered. In this simulation, the detected g values correspond to $\left\langle \frac{\mathrm{d}\alpha}{\mathrm{d}t} \right\rangle = 0.36^\circ/\mathrm{ms}$ in the nonlinear phase. The pitch angle scattering is thus very strong, but particles in a certain pitch angle range are scattered not continuously but instantaneously. The pro-

posed method can be applied to various types of wave-particle interactions in space plasma. A significant future work is the application of the proposed method to observations made in space by the forthcoming ERG satellite. Direct measurements in space plasma will provide important clues to the study of processes governing pitch angle scattering of energetic particles in the magnetosphere.

Chapter 3

Direct detection of pitch angle scattering of energetic protons caused by rising tone EMIC waves

In this chapter, we focus on the the pitch angle scattering of energetic ions caused by rising tone EMIC waves observed by THEMIS satellites, and apply the proposed method of WPIA to detect the pitch angle scattering.

3.1 THEMIS satellites and data set

The Time History of Events and Macroscale Interactions during Substorms (THEMIS) satellites constituted from five identical probes (probe A, B, C, D, and E) are launched on February 17, 2007. The main purpose of THEMIS satellites is to reveal the basic process of onset and evolution of substorm instability at the magnetotail [*Angelopoulos*, 2008]. After the main

2 years of main mission phase, probe B and C escaped from the initial orbits and have been located in the lunar orbit. Probe A, D, and E are still in the near-Earth orbits and continue to measure the plasma environment of the inner magnetosphere. In this section, we use data set of ESA, FGM, and EFI instruments installed on the THEMIS satellites. Figure 3.1 shows schematic diagram of THEMIS spacecraft including ESA, FGM, and EFI.

3.1.1 The Electrostatic Analyzer (ESA)

The Electrostatic Analyzer (ESA) [*McFadden et al.*, 2008] installed on the THEMIS satellites can detect ions in the energy range from 5 eV up to 25 keV with 32 energy channels. The ESA is designed with $180^\circ \times 6^\circ$ fields-of-view and sweeps out 4π steradians each 3 s by spin of a probe. The azimuthal angle ϕ resolution of the ESA burst-mode data is 22.5 degrees in the polar angle θ range from -45 to 45 degrees, but ϕ resolution of the sectors in the θ range of > 45 degrees and < -45 degrees is larger than 45 degrees. Therefore, we use only the data from near-equatorial sectors in the polar angle θ range from -45 to 45 degrees. The time resolution of the count rate detected by near-equatorial sectors is less than 6 ms for each energy sweeping. The picture of sensors are shown in Figure 3.2.

3.1.2 Fluxgate Magnetometer (FGM)

The Fluxgate Magnetometer (FGM) [*Auster et al.*, 2008] measures background and low frequency fluctuating magnetic field (Figure 3.3). The FGM is capable of detecting variations of the magnetic field with amplitudes of 0.01 nT. Because the sampling frequency of particles burst-mode data of FGM is 128 Hz, the detectable frequency range is DC up to 64 Hz. Therefore, we can

detect EMIC waves outside the L values of ~ 2 in burst-mode because the typical frequency of EMIC waves in the region is up to several tens of Hz.

3.1.3 Electric Field Instrument (EFI)

The Electric Field Instrument (EFI) [*Bonnel et al.*, 2008] measures the DC and fluctuating electric field and outputs the waveforme data. The sampling frequency of EFI in the particle burst-mode is 128 Hz which is the same as the time resolution of the FGM burst-mode data. Deployed configuration of sensor and boom systems are shown in Figure 3.4. In the EFI data, there is a radical difference between the electric field detected by the spin plane wire boom antenna ($>$ 40 m tip-to-tip) and spin axis stacer boom antenna ($<$ 7 m tip-to-tip). We estimate the spin axis component of the electric field of EMIC waves from the spin plane component and the magnetic field data with the plane wave assumption that is $\boldsymbol{E} \cdot \boldsymbol{B} = 0$ for each frequency [*Santolik et al.*, 2003a].

3.2 Event of rising tones

Nakamura et al. (2014) reported that THEMIS D observed rising tone EMIC waves on September 9, 2010 during the period from 14:20 UT to 14:45 UT (Figure 3.5). In this period, THEMIS D was located near the dayside magnetosphere at $\sim 8R_E$ radial distance from the center of the Earth. Observed EMIC waves are in the frequency range from 0.4 to 1.0 Hz, which corresponds to the proton band, and contain several elements with rising frequency sweep. The amplitude of rising tone EMIC waves reached to ~ 2 % of ambient magnetic field. During this period, THEMIS D observed the wave field and particle data with burst-mode operation. Using the burst mode

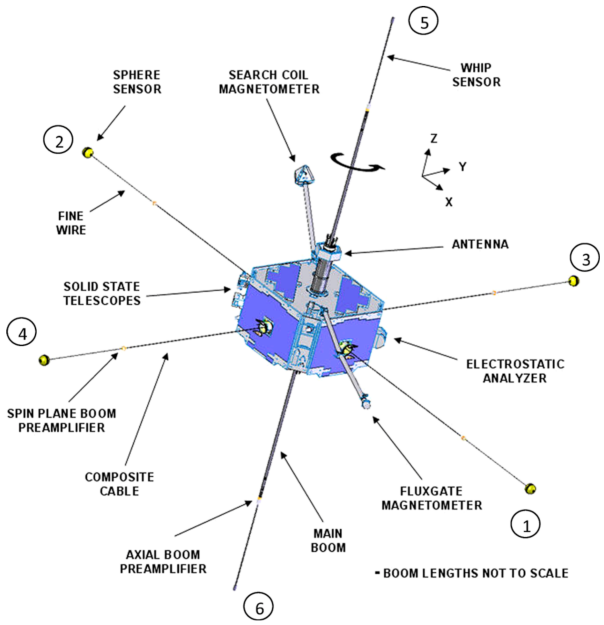

Figure 3.1: Schematic diagram of THEMIS spacecraft, including ESA, FGM, and antennas of EFI [*Bonnel et al.*, 2008].

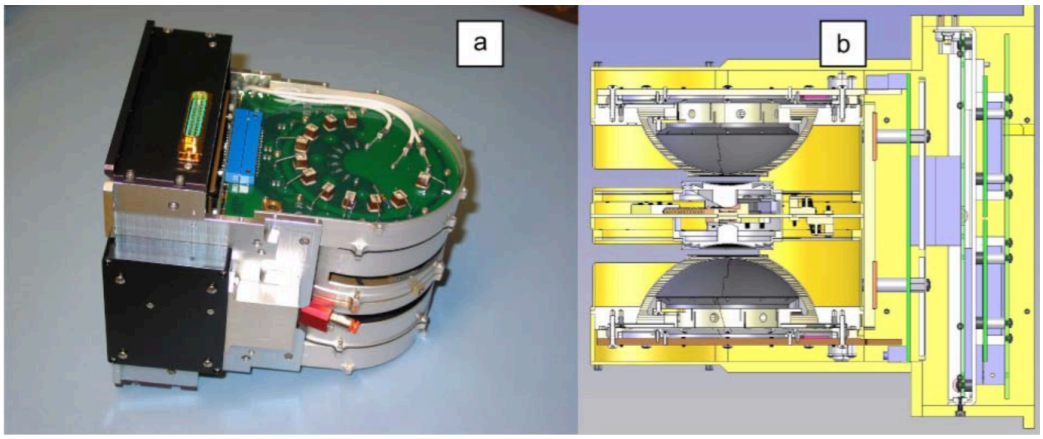

Figure 3.2: (a) A picture and (b) cross-section of the ESA installed on THEMIS satellites [*McFadden et al.*, 2008].

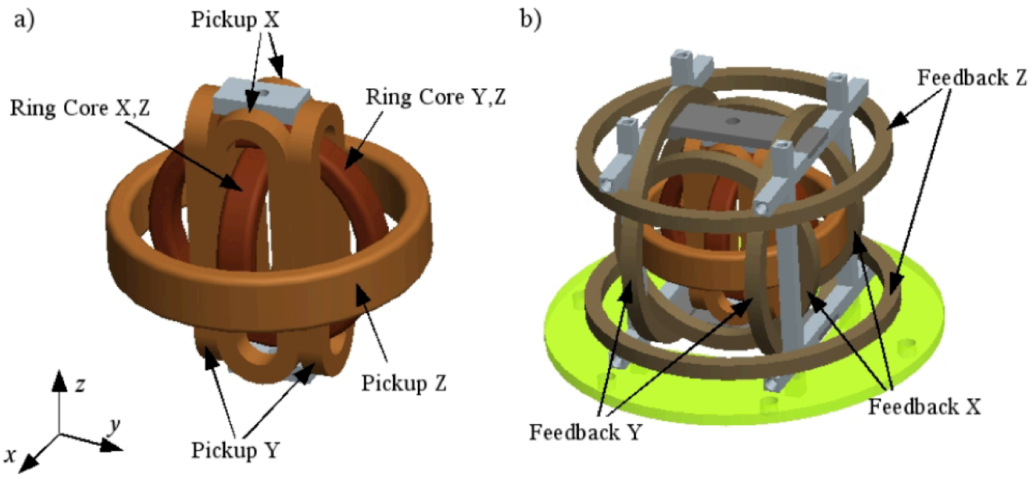

Figure 3.3: The illustration of 3-D model of the FGM sensor. (a) Ring cores and pick- up coil system and (b) fully functional sensor including the Helmholtz feedback system [*Auster et al.*, 2008].

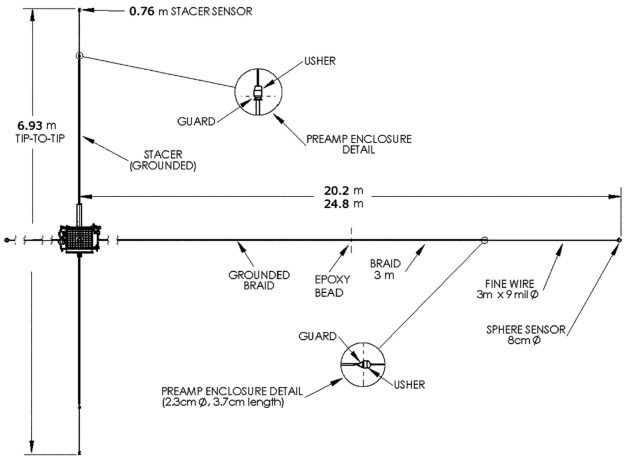

Figure 3.4: The illustration of the EFI sensor and boom system [*Bonnel et al.*, 2008].

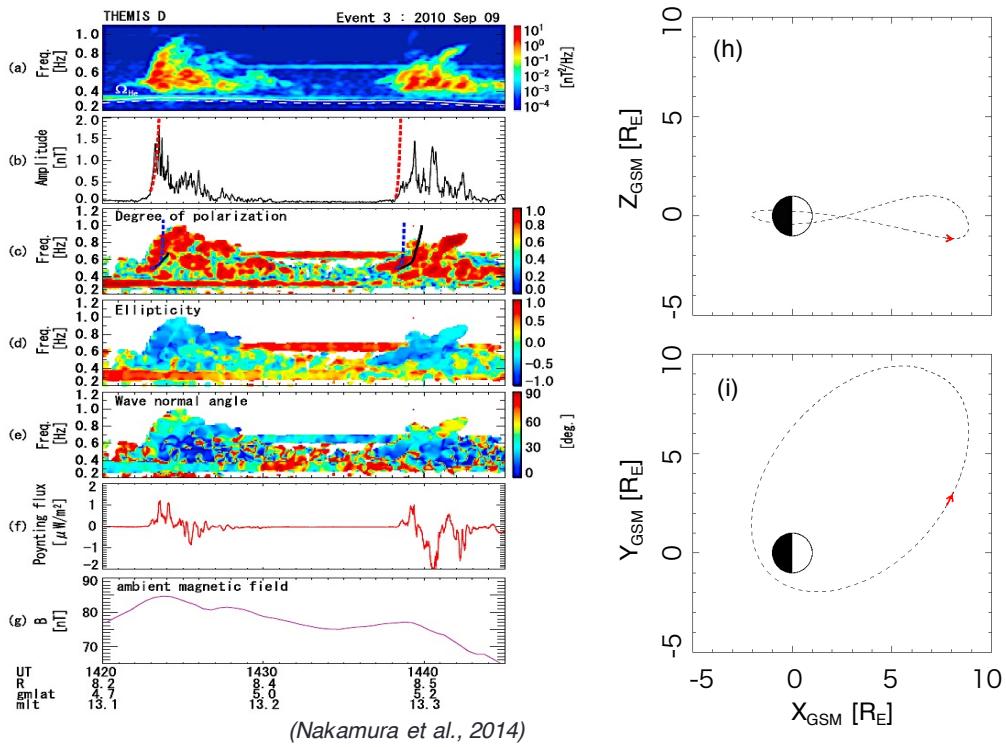

Figure 3.5: Overview of EMIC rising tone event observed on September 9, 2010. (a) Dynamic power spectra, (b) wave magnetic amplitudes, (c) degrees of polarization, (d) ellipticities, (e) wave normal angles, (f) the parallel component of Poynting flux, and (g) The ambient magnetic field intensity [*Nakamura et al.*, 2014]. Red arrows in (h) and (i) shows the location of THEMIS D in the GSM coordinate system during this period.

ESA, FGM, and EFI data of 2010/09/09 EMIC wave event, we apply the WPIA method proposed in the previous chapter and calculate G to directly detect the nonlinear pitch angle scattering caused by rising tone EMIC waves.

3.3 Method

In the previous chapter, we proposed the method to detect pitch angle scattering using WPIA. The G value is defined as

$$G = \iiint q\left(\boldsymbol{E}_w + \boldsymbol{v} \times \boldsymbol{B}_w\right) \cdot \boldsymbol{e}_\alpha f(\boldsymbol{v}, t) \mathrm{d}\boldsymbol{v}, \tag{3.1}$$

and, in the case of real observation, because we should calculate the G values from data for a finite number of particles, we can rewrite equation (3.1) as

$$G = \sum_i^N q\left(\boldsymbol{E}_w(t_i) + \boldsymbol{v}_i \times \boldsymbol{B}_w(t_i)\right) \cdot (\boldsymbol{e}_\alpha)_i. \tag{3.2}$$

To calculate G from equation (3.2), we need full components of waveform data of wave electric and magnetic field, respectively. Therefore, the electric and magnetic field waveforms are passed through a band-pass filter from 0.3 to 1.0 Hz. After then, We estimated E_z (the spin axis component of the electric field) using assumption of $\boldsymbol{E}_w \cdot \boldsymbol{B}_w = 0$ for each frequency. Band-passed E_x, E_y, B_x, B_y, B_z and estimated E_z are substituted for (3.2). The velocity vector of particles for each detected count is estimated from the energy of particles, azimuthal direction of detectors ϕ, and pitch angle α. Pitch angle is calculated from ambient magnetic field $\boldsymbol{B}_0$ that is calculated by 90 seconds averaged FGM data. The most significant factor $\boldsymbol{e}_\alpha$ is calculated for each sector using θ, ϕ, and α. As represented in the previous chapter, because $\boldsymbol{e}_\alpha$ is defined as

$$\boldsymbol{e}_\alpha = \boldsymbol{e}_\perp \cos\alpha - \boldsymbol{e}_\parallel \sin\alpha, \tag{3.3}$$

we calculate the $\boldsymbol{e}_\alpha$ as a unit vector using $\boldsymbol{e}_\perp$ and $\boldsymbol{e}_\parallel$ that is calculated from θ, ϕ, and direction of $\boldsymbol{B}_0$. Black arrows in Figure 3.6 are estimated $\boldsymbol{e}_\alpha$ for each sector in the range of $-45^\circ < \theta < 45^\circ$ in a certain spin period. The horizontal axis is the spin phase ϕ corresponding to spin period ($\sim$3 seconds). The red, orange, yellow, green, cyan, sky-blue, blue, and purple

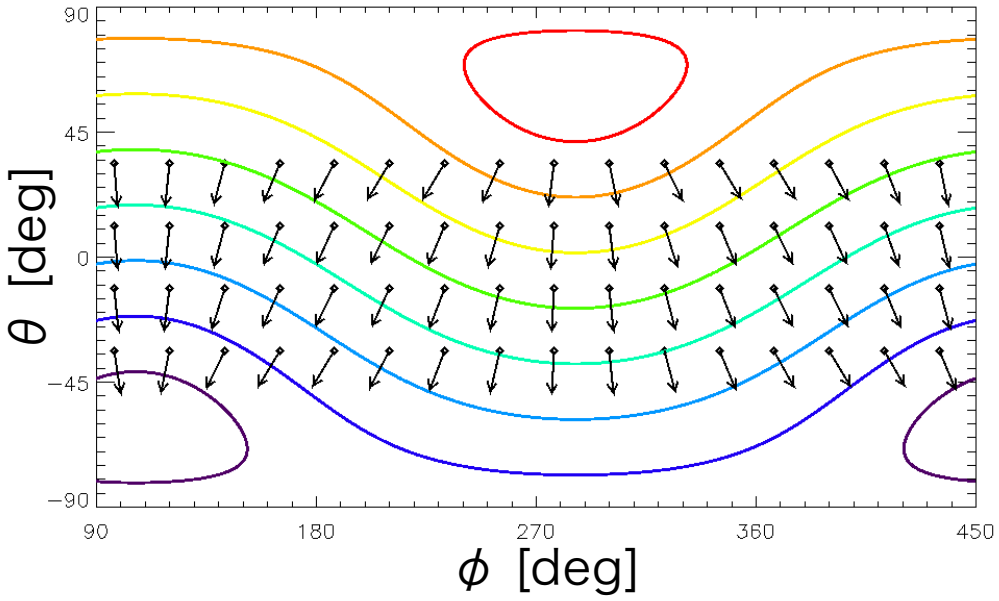

Figure 3.6: Example of $\boldsymbol{e}_\alpha$ estimated from θ, ϕ, and α.

lines are constant pitch angle line corresponding to 160, 140, 120, 100, 80, 60, 40, and 20 degrees, respectively. Using each count detected by each sector, we calculate (3.2) and integrate over 90 seconds time window. The method to calculate G values is summarized in Figure 3.7 as a flowchart.

3.4 Results and discussion

Figure 3.8 (a) shows dynamic spectrum of wave magnetic field with a unit of nT/Hz (note that (a) is not the power spectrum expressed as a unit of $\mathrm{nT}^2/\mathrm{Hz}$), and (b) shows the temporal variation of the parallel component of Poynting flux with a unit of $\mu\mathrm{W/m}^2$. Positive Poynting fluxes indicate the propagation toward northern hemisphere and negative values represent propagation toward southern hemisphere. Figures 3.8 (c) and (d) are the temporal variation of pitch angle distribution of detected count and G cal-

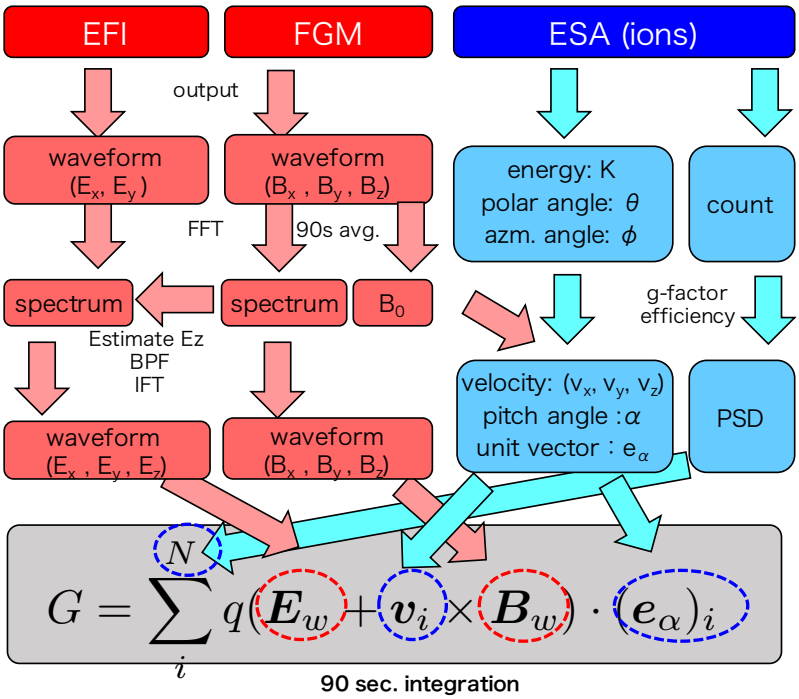

Figure 3.7: Flowchart of the WPIA analysis for THEMIS data.

culated from 5.255 keV ions, respectively. As a result, we can conclude that the G values successfully detect the nonlinear pitch angle scattering of ions caused by rising tone EMIC waves. The G values (Figure 3.8 (d)) represented that the significant pitch angles occurred when EMIC waves were exited during 14:38 UT from 14:43 UT. When Poynting flux is positive, the ions in the pitch angle range of less than 90 degrees are mainly scattered in pitch angle, and the ions in the pitch angle range of larger than 90 degrees are mainly scattered when the Poynting flux is negative. This facts are consistent with the cyclotron resonance condition expressed as

$$\omega - kv\cos\alpha = \Omega_{H^+}, \tag{3.4}$$

where the ω, k and Ω_{H^+} are the wave frequency, wave number, and proton gyro frequency. Because the frequency range of EMIC waves is less than proton gyro frequency, $k\cos\alpha$ is always negative. Therefore, for $k < 0$ (southward propagation), EMIC waves can resonate with protons in the pitch angle range of larger than 90 degrees, and for $k > 0$ (northward propagation), EMIC waves can resonate with protons in the pitch angle range of less than 90 degrees. Figure 3.9 is the same as Figure 3.8 but we use 6.917 keV ions for calculating G. In this energy range, we can also recognize that consistency between the interaction pitch angle and propagation direction.

Shoji et al. (2011) successfully demonstrated the generation of the rising tone EMIC waves in the simulation box by the ion hybrid code. The hybrid simulation results were provided by Dr. Shoji . calculate G with data obtain at the equator in the simulation box (Figure 3.10). (a) and (b) show dynamic spectrum of wave magnetic field and (c) and (d) shows temporal variation of G calculated from ~ 5 keV protons. (a) and (c) are results of simulation in the case of one element rising tone is generated (Case 1), and (b) and (d)

are results when several elements are generated and overlapped temporary (Case 2) [*Shoji and Omura*, 2013; *Shoji, private communication*]. In the case 1, protons in the pitch angle range of less than 90 degrees indicated both positive and negative G values that corresponds to pitch angle increasing and decreasing, respectively. Furthermore, In the Figure 3.8 (d), Figure 3.9 (d), and Figure 3.10 (c), particles in the pitch angle range of closer to 90 degrees tend to be scattered toward 90 degrees, and particles in the lower pitch angle tend to be scatter toward more lower pitch angle. Gendrin (1981) introduced the concept of particle motion along the diffusion curve. In this concept, the particles are scattered by waves along diffusion curves that is defined as concentric circles whose center is located at wave phase velocity in the velocity phase space. Considering the 1th order cyclotron resonance condition (counter streaming condition), the diffusion curves are written as in Figure 3.11. Therefore, the both direction scattering as shown in Figure 3.8 (d) and Figure 3.9 (d) are consistent with not only simulation results but also Gendrin's theory. On the contrary, protons in the pitch angle range of larger than 90 degrees showed only positive G values that means increasing pitch angle in the case 1. Furthermore, in the case 2, the overlapped rising tone elements are generated, G values shows more complicated scattering. What parameter does control the direction of pitch angle scattering is still open issue. To clarify these detail of pitch angle scattering process the we need more fundamental understanding for the nonlinear effect of wave particle interaction.

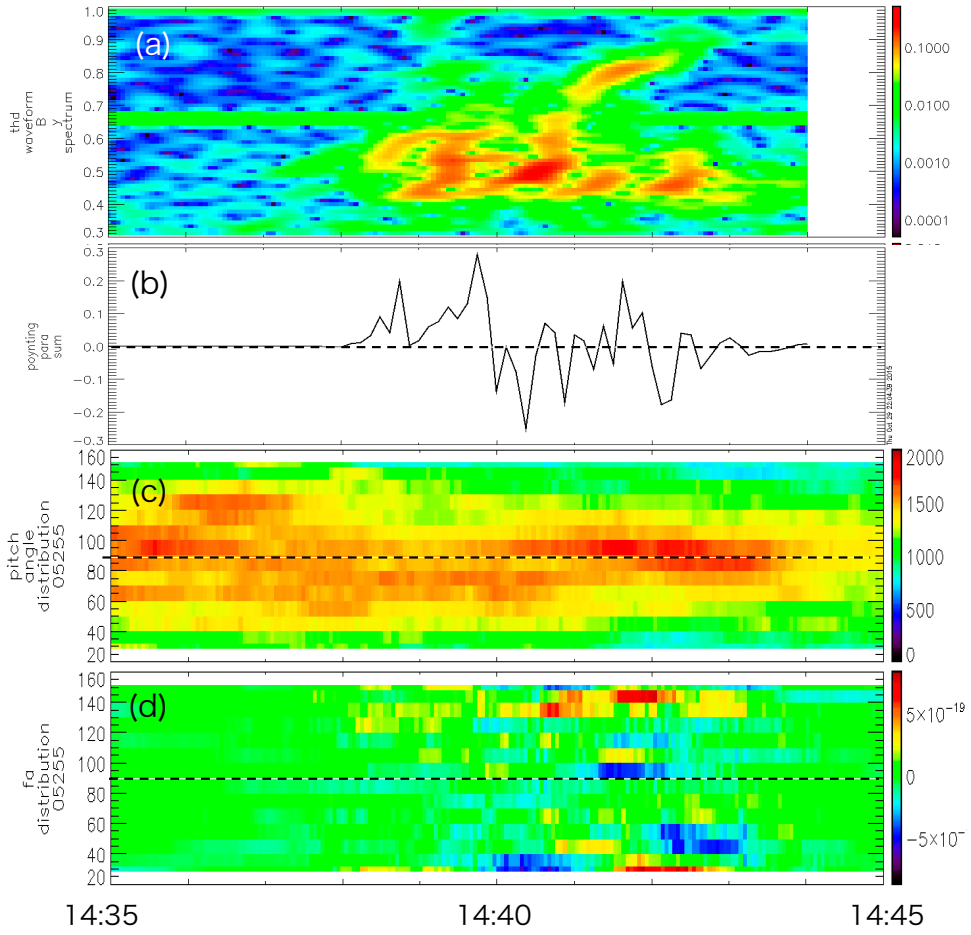

Figure 3.8: (a) Dynamic spectrum of wave magnetic field. a unit of the color bar is nT/Hz. (b) Poynting flux with a unit of μW/m^2. (c) and (d) is temporal variation of pitch angle distribution of count and G calculated from 5.255 keV ions.

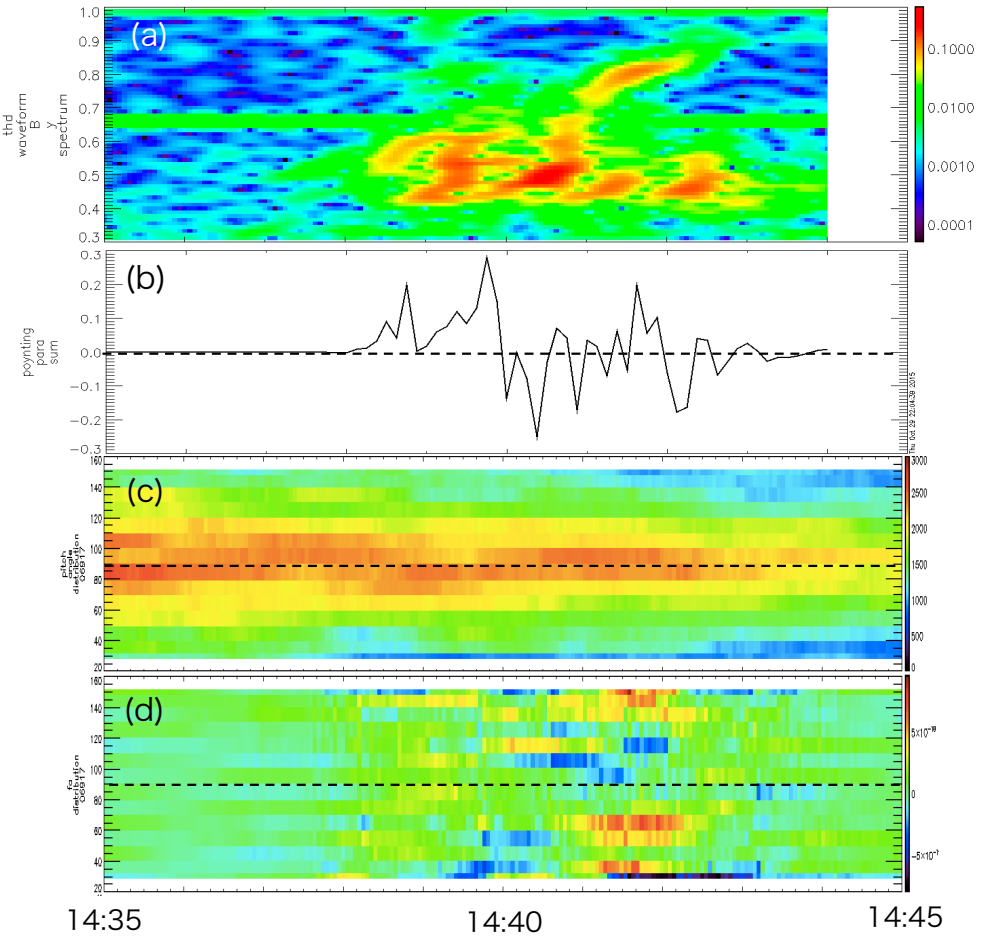

Figure 3.9: (a) and (b) is same figure as (a) and (b) in Figure 3.8. (c) and (d) is temporal variation of pitch angle distribution of count and G calculated from 6.917 keV ions.

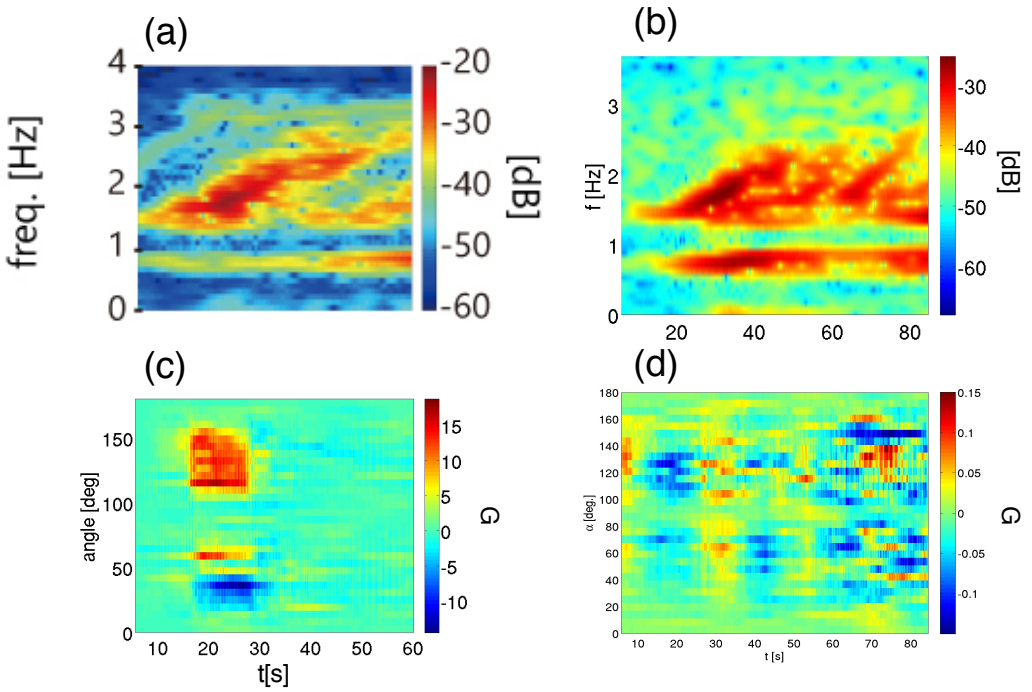

Figure 3.10: Simulation results of rising tone EMIC waves. Upper panels show dynamic spectrum of wave magnetic field and lower panels shows temporal variation of G calculated from ~ 5 keV protons detected at magnetic equator of simulation box. Left panels represent the results of simulation in the case of one element rising tone is generated, and right panels represent the results when several elements are generated in the simulation [*Shoji and Omura*, 2013].

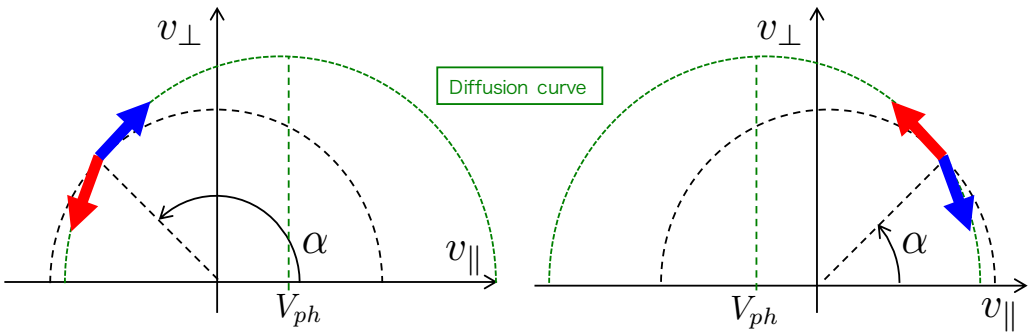

Figure 3.11: Diffusion curve introduced by Gendrin (1981) and scattering direction.

3.5 Concluding remarks

In this chapter, we focus on the the pitch angle scattering of energetic ions caused by rising tone EMIC waves observed by THEMIS satellites, and apply the proposed method of WPIA to detect the pitch angle scattering. THEMIS D observed rising tone EMIC waves on September 9, 2010 during the period from 14:20 UT to 14:45 UT. Using high resolution waveform data and particle count data detected ESA, EFI and FGM installed on THEMIS D, we calculate G values proposed in previous chapter. As a results we successfully detect the pitch angle scattering of ions by observation data. Furthermore, we compare the simulation results reproduced by a ion hybrid code (Shoji, private communication) and THEMIS observation. The both data show good agreement each other, and these results are also consistent with Gendrin's theory.

Chapter 4

Nonlinear pitch angle scattering of low pitch angle electrons caused by chorus emissions

The purpose of this chapter is to clarify the basic physics of interaction between low pitch angle electrons and coherent whistler mode waves such as chorus emissions in a dipole magnetic field using nonlinear theory. In section 1, we derive the equations of particle motion without small pitch angle approximation. After then, we demonstrate the motion of electrons predicted by the derived equations in the test particle simulation in section 2. In section 3, we discuss the significance of the pitch angle scattering of small pitch angle electrons in the inner magnetosphere.

4.1 Nonlinear theory of pitch angle scattering of electrons

In this section, we derive the motion of electrons near the loss cone in the velocity phase space, and discuss the difference of the particle motion under the assumption of moderate pitch angle approximation and low pitch angle approximation. Note that "low" pitch angle means that pitch angle is close to 0 or 180 degrees, "high" pitch angle means that pitch angle is close to 90 degrees, and "moderate" pitch angle is intermediate pitch angle between "low" and "high" pitch angle as in the pitch angle range from 30 to 60 degrees or from 120 to 150 degrees roughly.

4.1.1 Derivation of the equation of temporal variation of ζ

The equation of motion for electrons is expressed as

$$m\frac{\mathrm{d}(\gamma \boldsymbol{v})}{\mathrm{d}t} = -e[\boldsymbol{E}_w + \boldsymbol{v} \times (\boldsymbol{B}_0 + \boldsymbol{B}_w)], \tag{4.1}$$

where m, e, $\boldsymbol{v}$, and γ are the rest mass, elementary charge, velocity, and Lorentz factor of the electron, respectively. $\boldsymbol{E}_w$ and $\boldsymbol{B}_w$ are the electric and magnetic field of the wave, respectively, and $\boldsymbol{B}_0$ is the ambient magnetic field that does not depend on the time. The velocity vector is expressed as $\boldsymbol{v} = v_\parallel \boldsymbol{e}_\parallel + v_\perp \boldsymbol{e}_\perp$ and we define $\boldsymbol{e}_\phi$ by $\boldsymbol{e}_\phi = \boldsymbol{e}_\parallel \times \boldsymbol{e}_\perp$.

In the case that $\boldsymbol{B}_0$ has the gradient and satisfies $\nabla \cdot \boldsymbol{B}_0 = 0$, we can express the ambient magnetic field as

$$\boldsymbol{B}_0 = B_{0z}\boldsymbol{e}_z + \frac{r_c}{2}\frac{\partial B_{0z}}{\partial z}\boldsymbol{e}_\phi, \tag{4.2}$$

where r_c is the Larmor radius and expressed as $r_c = \frac{m\gamma v_\perp}{eB_0}$. This is because the direction of $\boldsymbol{e}_\phi$ is antiparallel to the radial direction. Assuming a purely parallel propagating electromagnetic wave along $B_{0z}\boldsymbol{e}_z$, we can express the wave electromagnetic fields as

$$\boldsymbol{E}_w = E_w(\sin\psi\boldsymbol{e}_x - \cos\psi\boldsymbol{e}_y), \tag{4.3}$$

$$\boldsymbol{B}_w = B_w(\cos\psi\boldsymbol{e}_x + \sin\psi\boldsymbol{e}_y), \tag{4.4}$$

where ψ is the wave phase and expressed as $\psi = \omega t - kz$ for the case of the right handed polarized whistler mode wave. Using the gyrophase of a particle, $\boldsymbol{e}_\parallel$, $\boldsymbol{e}_\perp$, and $\boldsymbol{e}_\phi$ are rewritten as $\boldsymbol{e}_\parallel = \boldsymbol{e}_z$, $\boldsymbol{e}_\perp = \cos\phi\boldsymbol{e}_x + \sin\phi\boldsymbol{e}_y$, and $\boldsymbol{e}_\phi = -\sin\phi\boldsymbol{e}_x + \cos\phi\boldsymbol{e}_y$. Using these forms and the relative phase angle $\zeta = \phi - \psi$, $\boldsymbol{E}_w$ and $\boldsymbol{B}_w$ are rewritten as

$$\boldsymbol{E}_w = E_w(-\sin\zeta\boldsymbol{e}_\perp - \cos\zeta\boldsymbol{e}_\phi), \tag{4.5}$$

$$\boldsymbol{B}_w = B_w(\cos\zeta\boldsymbol{e}_\perp - \sin\zeta\boldsymbol{e}_\phi). \tag{4.6}$$

Using (4.5) and (4.6), $\boldsymbol{v}\times\boldsymbol{B}_0$ term in the right hand side of (4.1) is expressed as

$$-e\boldsymbol{v}\times\boldsymbol{B}_0 = -e(v_\parallel\boldsymbol{e}_\parallel + v_\perp\boldsymbol{e}_\perp)\times\left(B_0\boldsymbol{e}_\parallel + \frac{r_c}{2}\frac{\partial B_0}{\partial z}\boldsymbol{e}_\phi\right) \tag{4.7}$$

$$= eB_0v_\perp\boldsymbol{e}_\phi - \frac{ev_\perp r_c}{2}\frac{\partial B_0}{\partial z}\boldsymbol{e}_\parallel + \frac{ev_\parallel r_c}{2}\frac{\partial B_0}{\partial z}\boldsymbol{e}_\perp. \tag{4.8}$$

The first term expresses the gyro motion of an electron, and the second and

third terms express the mirror force. The $\boldsymbol{v} \times \boldsymbol{B}_w$ term is expressed as

$$-e\boldsymbol{v} \times \boldsymbol{B}_w = -e(v_\parallel \boldsymbol{e}_\parallel + v_\perp \boldsymbol{e}_\perp) \times B_w(\cos\zeta \boldsymbol{e}_\perp - \sin\zeta \boldsymbol{e}_\phi) \tag{4.9}$$

$$= ev_\parallel B_w(-\sin\zeta \boldsymbol{e}_\perp - \cos\zeta \boldsymbol{e}_\phi) + ev_\perp B_w \sin\zeta \boldsymbol{e}_\parallel. \tag{4.10}$$

The each component of the equation (4.1) is expressed as

$$\frac{\mathrm{d}(\gamma v_\parallel)}{\mathrm{d}t} = -\frac{ev_\perp r_c}{2m}\frac{\partial B_0}{\partial z} + \frac{eB_w}{m} v_\perp \sin\zeta, \tag{4.11}$$

$$\frac{\mathrm{d}(\gamma v_\perp)}{\mathrm{d}t} = \frac{ev_\parallel r_c}{2m}\frac{\partial B_0}{\partial z} + \frac{e}{m}(E_w - v_\parallel B_w)\sin\zeta, \tag{4.12}$$

$$\gamma v_\perp \frac{\mathrm{d}\phi}{\mathrm{d}t} = \frac{eB_0}{m} v_\perp + \frac{e}{m}(E_w - v_\parallel B_w)\cos\zeta, \tag{4.13}$$

where r_c and ζ are the Larmor radius and the relative phase angle, and are expressed as $r_c = (m\gamma v_\perp)/(eB_0)$ and $\zeta = \phi - \psi$, respectively. Note that the second term of (4.12) and (4.13) are caused by $\boldsymbol{v}_\parallel \times \boldsymbol{B}_w$ Lorentz force (see Appendix A). From equation (4.13) and the definition of ζ and ψ, the time variation of ζ is derived as

$$\begin{aligned}\frac{\mathrm{d}\zeta}{\mathrm{d}t} &= \frac{\mathrm{d}\phi}{\mathrm{d}t} - \frac{\mathrm{d}\psi}{\mathrm{d}t} \\ &= \left[\frac{\Omega_0}{\gamma} + \frac{e\left(E_w - v_\parallel B_w\right)}{m\gamma v_\perp}\cos\zeta\right] - (\omega - v_\parallel k),\end{aligned} \tag{4.14}$$

where $\Omega_0 = eB_0/m$. Here, we define resonant velocity V_R and θ as $V_R = (\omega - \Omega_0/\gamma)/k$ and $\theta = k(v_\parallel - V_R)$, respectively. Hence, we obtain the time variation of ζ as

$$\frac{\mathrm{d}\zeta}{\mathrm{d}t} = \theta + \frac{e\left(E_w - v_\parallel B_w\right)}{m\gamma v_\perp}\cos\zeta. \tag{4.15}$$

4.1.2 Derivation of the equation of temporal variation of θ

In this subsection, we derive the time variation of θ on the Lagrangian frame of a particle without the assumption of $v_\parallel = V_R$ or $\theta = 0$. The definition of θ is

$$\theta = k(v_\parallel - V_R). \tag{4.16}$$

θ is a frequency dimension parameter that indicates the difference between particle velocity and cyclotron resonance velocity of coherent whistler mode waves. Differentiating both sides of (4.16) with respect to time t, we have following equation:

$$\frac{\mathrm{d}\theta}{\mathrm{d}t} = \frac{\mathrm{d}k}{\mathrm{d}t}(v_\parallel - V_R) + k\left(\frac{\mathrm{d}v_\parallel}{\mathrm{d}t} - \frac{\mathrm{d}V_R}{\mathrm{d}t}\right). \tag{4.17}$$

At first, we derive $\mathrm{d}k/\mathrm{d}t$ and $\mathrm{d}\omega/\mathrm{d}t$ on the Lagrangian frame of a particle. The definition of wave phase of right handed polarized wave is

$$\psi = \omega t - kz. \tag{4.18}$$

Differentiating both sides of (4.18) with respect to t and z, we obtain the

relation

$$\omega = \frac{\partial \psi}{\partial t} \quad \text{and} \quad k = -\frac{\partial \psi}{\partial z}. \tag{4.19}$$

Therefore, we obtain the relation between ω and k:

$$\frac{\partial \omega}{\partial z} = -\frac{\partial k}{\partial t}. \tag{4.20}$$

Here, assuming purely parallel propagating whistler mode waves, the dispersion relation is the implicit function of ω, k, and Ω_0:

$$c^2 k^2 = \omega^2 + \frac{\omega \Pi^2}{\Omega_0 - \omega}. \tag{4.21}$$

Hence, we can express the time variation of frequency on the Eulerian frame as

$$\frac{\partial \omega}{\partial t} = \frac{\partial \omega}{\partial k}\frac{\partial k}{\partial t} + \frac{\partial \omega}{\partial \Omega_0}\frac{\partial \Omega_0}{\partial t}. \tag{4.22}$$

Since $\partial \Omega_0 / \partial t = 0$ and $\partial \omega / \partial k = V_g$, we have the following equation;

$$\frac{\partial \omega}{\partial t} = V_g \frac{\partial k}{\partial t}. \tag{4.23}$$

Furthermore, substituting (4.20), we obtain

$$\frac{\partial \omega}{\partial t} = -V_g \frac{\partial \omega}{\partial z}. \tag{4.24}$$

Similarly, we can express the spatial variation of wave number on the Eulerian frame as

$$\frac{\partial k}{\partial z} = \frac{\partial k}{\partial \omega}\frac{\partial \omega}{\partial z} + \frac{\partial k}{\partial \Omega_0}\frac{\partial \Omega_0}{\partial z}, \tag{4.25}$$

and we obtain the following equation using (4.24):

$$\frac{\partial k}{\partial z} = -\frac{1}{V_g^2}\frac{\partial \omega}{\partial t} + \frac{\partial k}{\partial \Omega_0}\frac{\partial \Omega_0}{\partial z}. \tag{4.26}$$

Therefore, using (4.23), (4.24), and (4.26), we can obtain the time differentiation of frequency and wave number on the Lagrangian frame of a particle as

$$\begin{aligned} \frac{\mathrm{d}k}{\mathrm{d}t} &= \frac{\partial k}{\partial t} + v_\parallel \frac{\partial k}{\partial z} \\ &= \frac{1}{V_g}\left(1 - \frac{v_\parallel}{V_g}\right)\frac{\partial \omega}{\partial t} + v_\parallel \frac{\partial k}{\partial \Omega_0}\frac{\partial \Omega_0}{\partial z}, \end{aligned} \tag{4.27}$$

and

$$\begin{aligned}\frac{\mathrm{d}\omega}{\mathrm{d}t} &= \frac{\partial\omega}{\partial t} + v_{\parallel}\frac{\partial\omega}{\partial z} \\ &= \left(1 - \frac{v_{\parallel}}{V_g}\right)\frac{\partial\omega}{\partial t}. \end{aligned} \tag{4.28}$$

Now, the relativistic equation of motion is represented as

$$\frac{\mathrm{d}u_{\parallel}}{\mathrm{d}t} = -\frac{v_{\perp}r_c}{2}\frac{\partial\Omega_0}{\partial z} + v_{\perp}\Omega_w \sin\zeta, \tag{4.29}$$

$$\frac{\mathrm{d}u_{\perp}}{\mathrm{d}t} = \frac{v_{\parallel}r_c}{2}\frac{\partial\Omega_0}{\partial z} + \left(\frac{\omega}{k} - v_{\parallel}\right)\Omega_w \sin\zeta, \tag{4.30}$$

where $u_{\parallel} = \gamma v_{\parallel}$, $u_{\perp} = \gamma v_{\perp}$, and $\gamma = \sqrt{1 + (u_{\parallel}^2 + u_{\perp}^2)/c^2}$. Using (4.29) and (4.30), we obtain

$$\begin{aligned}\frac{\mathrm{d}\gamma}{\mathrm{d}t} &= \frac{\partial\gamma}{\partial u_{\parallel}}\frac{\mathrm{d}u_{\parallel}}{\mathrm{d}t} + \frac{\partial\gamma}{\partial u_{\perp}}\frac{\mathrm{d}u_{\perp}}{\mathrm{d}t} \\ &= \frac{1}{c^2}\left(v_{\parallel}\frac{\mathrm{d}u_{\parallel}}{\mathrm{d}t} + v_{\perp}\frac{\mathrm{d}u_{\perp}}{\mathrm{d}t}\right) \\ &= \frac{\omega\Omega_w v_{\perp}}{kc^2}\sin\zeta. \end{aligned} \tag{4.31}$$

The cyclotron resonance velocity V_R is expressed as

$$V_R = \frac{1}{k}\left(\omega - \frac{\Omega_0}{\gamma}\right). \tag{4.32}$$

Using (4.27), (4.28), and (4.31), we can derive the time variation of V_R as

$$\begin{aligned}\frac{\mathrm{d}V_R}{\mathrm{d}t} =& \frac{1}{k}\left(\frac{\mathrm{d}\omega}{\mathrm{d}t} - \frac{1}{\gamma}\frac{\mathrm{d}\Omega_0}{\mathrm{d}t} + \frac{\Omega_0}{\gamma^2}\frac{\mathrm{d}\gamma}{\mathrm{d}t}\right) - \frac{1}{k^2}\frac{\mathrm{d}k}{\mathrm{d}t}\left(\omega - \frac{\Omega_0}{\gamma}\right) \\ =& \frac{\Omega_0}{\gamma^2}\frac{\omega\Omega_w v_\perp}{k^2c^2}\sin\zeta + \frac{1}{k}\left(1 - \frac{v_\parallel}{V_g}\right)\left(1 - \frac{V_R}{V_g}\right)\frac{\partial\omega}{\partial t} - \frac{v_\parallel}{k\gamma}\left(1 + \gamma V_R\frac{\partial k}{\partial\Omega_0}\right)\frac{\partial\Omega_0}{\partial z}.\end{aligned} \tag{4.33}$$

Substituting (4.27), (4.28), (4.31), and (4.33) into (4.17), we can obtain the time variation of θ as

$$\frac{\mathrm{d}\theta}{\mathrm{d}t} = \left(1 - \frac{\omega(\omega+\theta)}{k^2c^2}\right)\frac{kv_\perp\Omega_w}{\gamma}\sin\zeta - \left(1 - \frac{v_\parallel}{V_g}\right)^2\frac{\partial\omega}{\partial t} + \left(\frac{v_\parallel}{\gamma} - \frac{kv_\perp^2}{2\Omega_0} + v_\parallel^2\frac{\partial k}{\partial\Omega_0}\right)\frac{\partial\Omega_0}{\partial z}. \tag{4.34}$$

Assuming $\theta = 0$, we can find that the coefficient of the first term is equal to ω_{tr} in Hikishima et al. (2009). Moreover, we can calculate $\partial k/\partial\Omega_0$ from (4.21) as

$$\frac{\partial k}{\partial\Omega_0} = -\frac{\omega\Pi^2}{2c^2k(\Omega_0 - \omega)^2}. \tag{4.35}$$

If we substitute (4.35) and $v_\parallel = V_R$ into (4.34), we can obtain same expression as the equation (27) and (28) in Omura et al. (2008, 2009) and Hikishima et al. (2009). We can also derive the time variation of θ as the following equation;

$$\frac{\mathrm{d}\theta}{\mathrm{d}t} = \omega_{tr}^2(\sin\zeta + S), \tag{4.36}$$

where

$$\omega_{tr} = \sqrt{\left(1 - \frac{\omega(\omega+\theta)}{k^2c^2}\right)\frac{kv_\perp\Omega_w}{\gamma}}, \tag{4.37}$$

$$S = -\frac{1}{\omega_{tr}^2}\left(s_1\frac{\partial\omega}{\partial t} + s_2\frac{\partial\Omega_0}{\partial z}\right), \tag{4.38}$$

$$s_1 = \left(1 - \frac{v_\parallel}{V_g}\right)^2, \tag{4.39}$$

$$s_2 = -\frac{v_\parallel}{\gamma} + \frac{kv_\perp^2}{2\Omega_0} - v_\parallel^2\frac{\partial k}{\partial\Omega_0}. \tag{4.40}$$

4.1.3 Low pitch angle approximation

In previous studies, the second term of equation (4.15) is neglected based on the assumptions of small wave amplitude and/or sufficiently large pitch angle [e.g., Dysthe, 1971; Nunn, 1974; Matsumoto an Omura, 1981; Omura et al., 2008, 2009; Li et al., 2015]. With these assumptions, because parameter S has large value due to small ω_{tr}, particles cannot be trapped by the wave potential.

On the contrary, we cannot ignore the second term in the case of low pitch angle electrons and whistler mode chorus emissions because $v_\perp$ is small. As shown in equation (4.13), the cosine term of equation (4.15) is mainly derived from the Lorentz force caused by parallel velocity and wave magnetic field. From geometric consideration in Figure 4.1, $\boldsymbol{v}_\parallel \times \boldsymbol{B}_w$ Lorentz force acts on particles in the direction of anti-parallel to the wave electric field, in other words, in the direction of $\zeta = 90^\circ$. This fact is also derived from equation (4.15). Assuming that particles satisfy the cyclotron resonant condition, we can derive $\theta \simeq 0$ and reduce equation (4.15) as

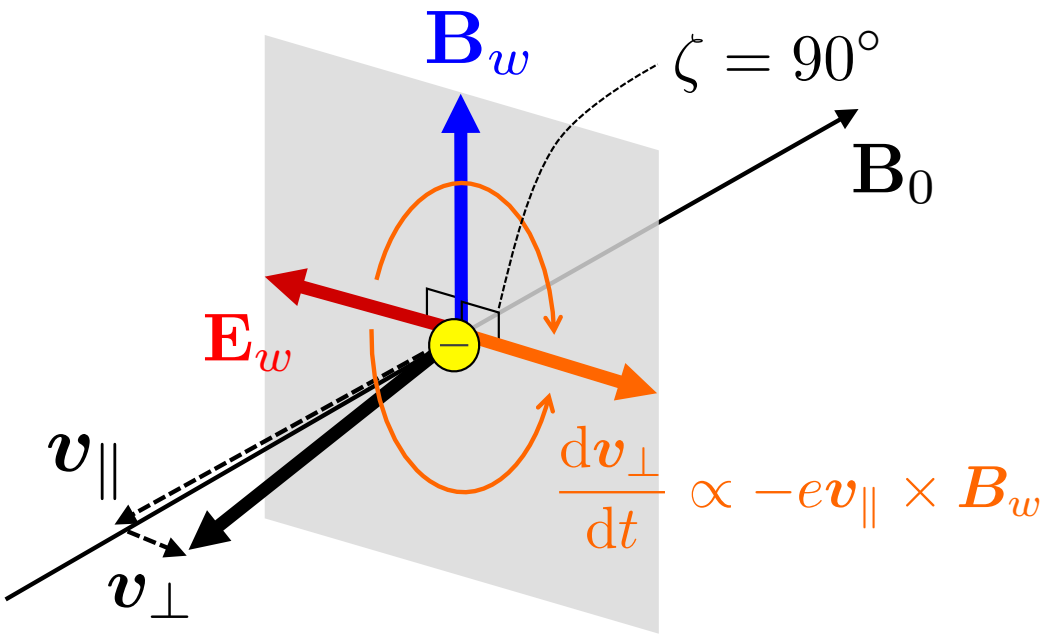

Figure 4.1: Geometric relation between wave Lorentz force and velocity of particles.

$$\frac{\mathrm{d}\zeta}{\mathrm{d}t} = C_w \cos\zeta, \tag{4.41}$$

where

$$C_w = \frac{\Omega_w \Omega_0}{\gamma^2 v_\perp k} = \frac{e\left(E_w - v_\parallel B_w\right)}{m\gamma v_\perp}. \tag{4.42}$$

We can solve equation (4.41) analytically using the method of separation of variables. After we rearrange terms and integrate both sides of the equation, we obtain the following equation;

$$\int \frac{\mathrm{d}\zeta}{\cos\zeta} = \int C_w \mathrm{d}t. \tag{4.43}$$

Here, the relation $x = \sin\zeta$ can be used and the left hand side of equation (4.43) should be rewritten as $\int \frac{\mathrm{d}\zeta}{\cos\zeta} = \int \frac{\mathrm{d}x}{(1+x)(1-x)} = \frac{1}{2}\log\left|\frac{1+x}{1-x}\right| + const.$, namely,

$$\frac{1}{2}\log\left(\frac{1+\sin\zeta}{1-\sin\zeta}\right) = C_w(t+t_0), \tag{4.44}$$

where t_0 is the integration constant related to the initial condition of particles. Since $2\tanh^{-1} y = \log\{(1+y)/(1-y)\}$, we can obtain the solution:

$$\sin\zeta = \tanh[C_w(t+t_0)]. \tag{4.45}$$

Therefore,

$$\zeta = \sin^{-1}[\tanh C_w(t+t_0)]. \tag{4.46}$$

Because the hyperbolic tangent function increases monotonically and has the upper bound at 1, ζ also converges to 90 degrees with time increasing. As shown in equation (4.42), because C_w indicates the Lorentz force caused by wave electric field and $v_\parallel \times B_w$, this results represent that the low pitch angle electrons near the loss cone are scattered toward 90 degrees in pitch angle due to wave Lorentz force, and the large amplitude waves scatter electrons away from the loss cone more efficiently.

4.1.4 Moderate pitch angle approximation

After ζ of electrons are regulated toward the 90 degrees by waves, $v_\perp$ and $|v_\parallel|$ of electrons increase and decrease due to the second terms of equation (4.11) and (4.12), respectively. Therefore, the first term θ becomes dominant and the second term becomes negligible due to large $v_\perp$. In previous studies, they have also assumed that the second term of equation (4.15) is neglected under the assumptions of small wave amplitude and/or sufficiently large pitch angle [e.g., Dysthe, 1971; Nunn 1974; Matsumoto an Omura, 1981; Omura et al., 2008, 2009; Hikishima et al., 2009, 2010; Li et al., 2015]. With these assumptions, we can rewrite equations (4.15) and (4.36) into the following approximated equations:

$$\frac{\mathrm{d}\zeta}{\mathrm{d}t} = \theta, \tag{4.47}$$

and

$$\frac{\mathrm{d}\theta}{\mathrm{d}t} = \tilde{\omega}_{tr}^2(\sin\zeta + \tilde{S}), \tag{4.48}$$

where

$$\tilde{\omega}_{tr} = \sqrt{\left(1 - \frac{\omega^2}{k^2c^2}\right)\frac{kv_\perp\Omega_w}{\gamma}}, \tag{4.49}$$

$$\tilde{S} = -\frac{1}{\tilde{\omega}_{tr}^2}\left(s_1\frac{\partial\omega}{\partial t} + s_2\frac{\partial\Omega_0}{\partial z}\right). \tag{4.50}$$

In this regime, the electrons regulated near the $\zeta \sim 90^\circ$ are inside of the closed trajectory, so-called the electromagnetic electron hole [Omura et al., 2008, 2009; Hikishima et a., 2009]. Therefore, the low pitch angle electrons

scattered away from loss cone tend to be trapped the wave potential continuously.

4.2 Test particle simulations

To evaluate the nonlinear effect for the low pitch angle electrons, we carry out test particle simulations of energetic electrons interacting with coherent whistler mode waves. We solve the relativistic equation of motion in the cylindrical coordinate system (see equations (4.11), (4.12), and (4.13)) with the dipole field as $\boldsymbol{B}_0$ using 4th order Runge–Kutta method. To estimate the wave propagation, we also solve the advection equation of wave amplitude and frequency [e.g., Omura et al., 1991; Furuya et al., 2008]. The group velocity of whistler mode wave is calculated from the dispersion relation of purely parallel propagating whistler mode wave (see equation 4.21). We assume that simulation box is spatially one dimension along $\boldsymbol{B}_0$. We also assume $L = 4$, the plasma frequency $\Pi = 4\Omega_{0eq}$, the initial energy of electrons are 20 keV, and pitch angle is 5°. With these conditions, we perform the test particle simulations. In the case 1, we use simple wave model that the wave has constant frequency 0.30 Ω_0, and the wave exists in the entire of simulation box. In the case 2, we use chorus-like wave model. The wave frequency is swept from 0.30 Ω_0 to 0.45 Ω_0 with sweep rate is 1.0 Ω_0/s, and start and end frequency are 0.30 Ω_0 and 0.45 Ω_0, respectively. The wave packet is spatially-finite. The packet length is determined from these parameter.

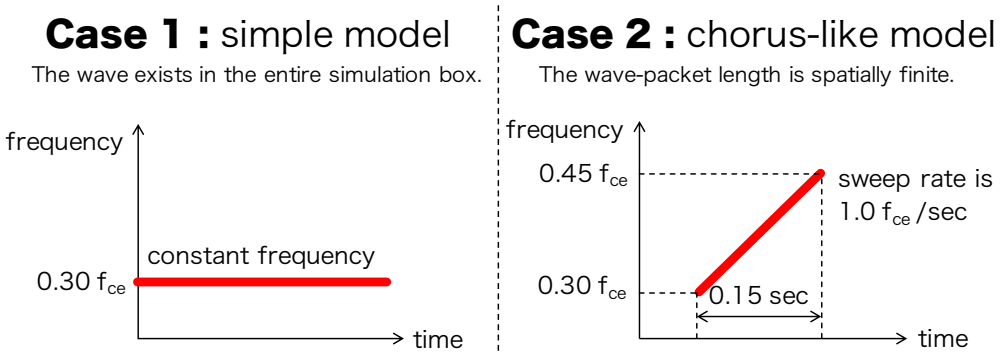

Figure 4.2: Input chorus frequency model in the test particle simulation.

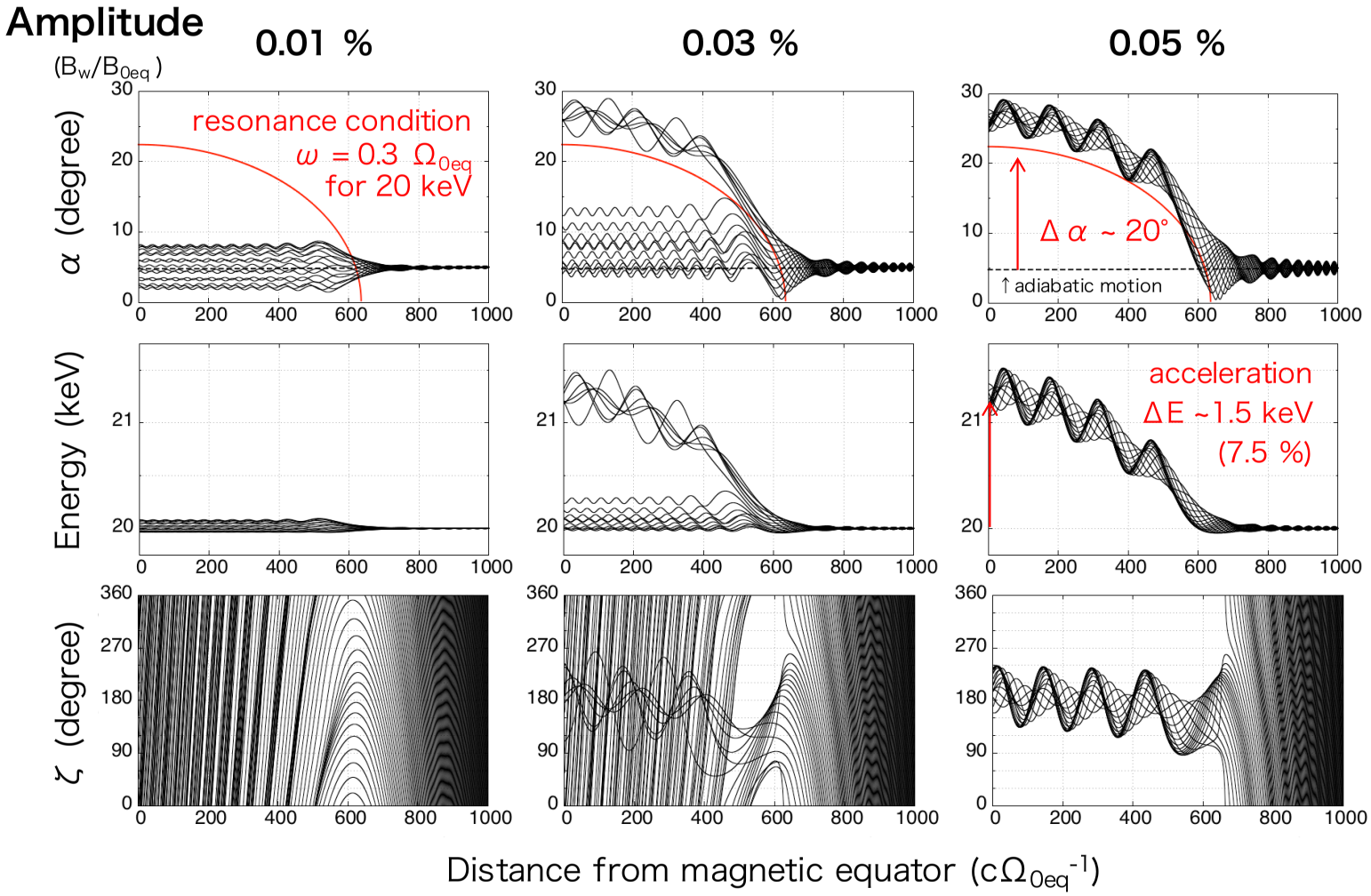

Figure 4.3: The trajectories of low pitch angle electrons for each wave amplitude in the case 1 (constant frequency case).

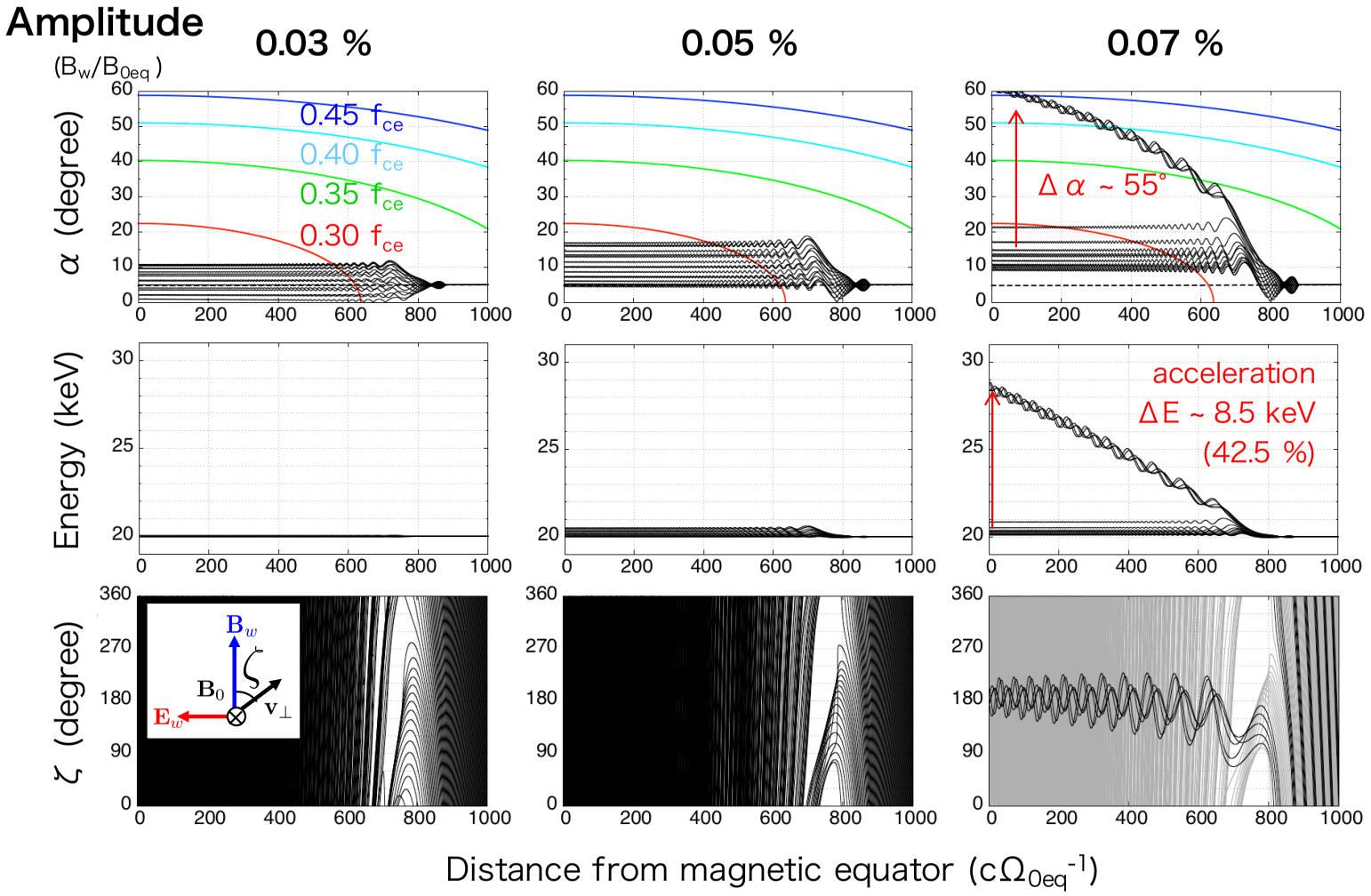

Figure 4.4: The trajectories of low pitch angle electrons for each wave amplitude in the case 2 (sweeping frequency case).

Figures (4.3) and (4.4) show the example of simulation results of wave particle interactions of low pitch angle electrons for each wave intensity. We survey the wave amplitude from 0.01 to 0.1 % of B_0, correspond to 50 to 500 pT. According to Santolik et al. (2014), the amplitude of chorus emissions is typically about tens to hundreds picotesla, and sometimes reaches more than 1 % of the ambient magnetic field. Figure 4.3 shows the simulation results of the case 1. The horizontal axes of all panels in Figure 4.3 represent the distance from the magnetic equator. The vertical axes of upper, middle, and lower panels show the pitch angle α, the energy, and relative phase angle ζ, respectively. The left, middle, and right panels are the results of the case that wave amplitude is 0.01, 0.03, and 0.05 % of the ambient magnetic field B_0, respectively. In this simulation, input particles move toward the magnetic equator (from right to left in each panels of Figure 4.3). When particles reaching the point that particles satisfy the resonant condition, the pitch angle of particles are scattered by the wave. In the case of weak amplitude, the particles are scattered in both direction, toward and away from the loss cone. On the contrary, in the case that wave amplitude is 0.03 % of B_0, some particles are trapped and accelerated by the wave. In the case of more large amplitude, all particles are trapped and accelerated, and the energy of particles increase by 7.5 % of their energy and the pitch angle increase by 20 degrees. Figure 4.4 shows the simulation results of the case 2. The wave packet length is spatially finite and the wave frequency is swept. Compared to the result of the case 1, more large amplitude waves are required to trap particles. In the case that wave amplitude is 0.03 % of B_0, particle motion is still diffusion-like, and even in the case of 0.05 % amplitude waves, particles are not trapped. However, almost all of particles are unidirectionally scattered away from lose cone. In the case of 0.07 %,

some particles are trapped and accelerated more than 42 % of their energy, and the pitch angle increase by 55 degrees. The trapped particles in the case 2 are more strongly accelerated and scattered away from the loss cone compared to the case 1. The large amplitude wave tend to trap the particles efficiently, and frequency sweep also contribute to scattering away from the loss cone. This is because the higher frequency wave can resonate with the higher pitch angle particles, and accelerated particles can also resonate with the higher frequency wave. Hence, the rising tone emissions can efficiently scatter the trapped particles away from the loss cone. According to the lower panels of Figure 4.3, the weak amplitude wave cannot trap particles due to large $|S|$ and particles are scattered with diffusion-like behavior. However, larger amplitude wave modulate the trajectory of electrons, and particles tend to move from 270° to 90°, and the modulated particles are trapped by wave. This simulation results are consistent with the theory derived in previous section.

To reveal that the behavior of low pitch angle particles interacting with the coherent waves are different from the motion predicted by the conventional nonlinear theory expressed as the moderate pitch angle approximation, we compare the trajectories of low and moderate pitch angle particles. Left side panels of Figure 4.5 are the interaction of the low pitch angle electrons ($\alpha = 5°$) interacting with constant frequency waves with $\omega = 0.30\ \Omega_{0eq}$, and right side panels show the interaction of moderate pitch angle electrons ($\alpha = 60°$) interacting with constant frequency waves with $\omega = 0.45\ \Omega_{0eq}$ for $B_w = 0.05\ B_0$. Top, middle, and bottom panels shows that pitch angle variation, inhomogeneity factor S, and θ and C_w. Red dashed lines in the upper panels are resonance pitch angle for each frequency and black dashed lines indicate pitch angle variation of adiabatic bounce motion. In the case

of moderate pitch angle particles interaction, S parameter is in the range of $|S| < 1$ and the first term of equation (4.15) θ indicated by red lines is dominant and C_w indicated by blue lines which is the second term of equation (4.15) is relatively negligible. On the contrary, because $|S|$ parameter of low pitch angle particles interacting with coherent waves are much larger than 1, the particles should be scattered diffusively in the frame of conventional nonlinear theory expressed as the pendulum equations. However, as shown in the left-lower panel of Figure 4.5 , C_w of low pitch angle particles is relatively significant rather than θ. Therefore, particles are scattered away from the loss cone and ζ is modulated toward 90° in the frame of low pitch angle approximation near the region that particles satisfy the resonant condition ($\theta \sim 0$) as shown in Figure 4.6. After the pitch angle increase, the motion of particles are shift to the regime of moderate pitch angle approximation. Hence, the all particles scattered at low pitch angle are trapped because the moderate pitch angle approximation is started at $\zeta \sim 90°$ which is the inside of closed trajectory in the ζ-θ phase space in the frame of moderate pitch angle approximation.

Figure 4.7 shows C_w/θ (upper) and S (lower) in the case of low (left) and moderate (right) pitch angle particles analytically expected by the input parameter. Vertical and horizontal axes in all panels represent pitch angle and distance from the magnetic equator in the simulation space, respectively. Solid lines indicate the resonance condition, and dashed lines is the pitch angle width of corresponding to the electromagnetic electron hole width calculated from $\alpha_{tr\pm} = \cos^{-1}[(V_R \pm V_{tr})/v]$, where V_{tr} is the width of closed trajectory in the θ-ζ phase space expressed as $V_{tr} = \theta/k|_{(\zeta=\sin^{-1} S)}$. For the case of moderate pitch angle particles, $|S|$ parameter is less than 1 near the resonance conditions (Figure 4.7 (d)) and C_w is less than 1 % of θ (Figure

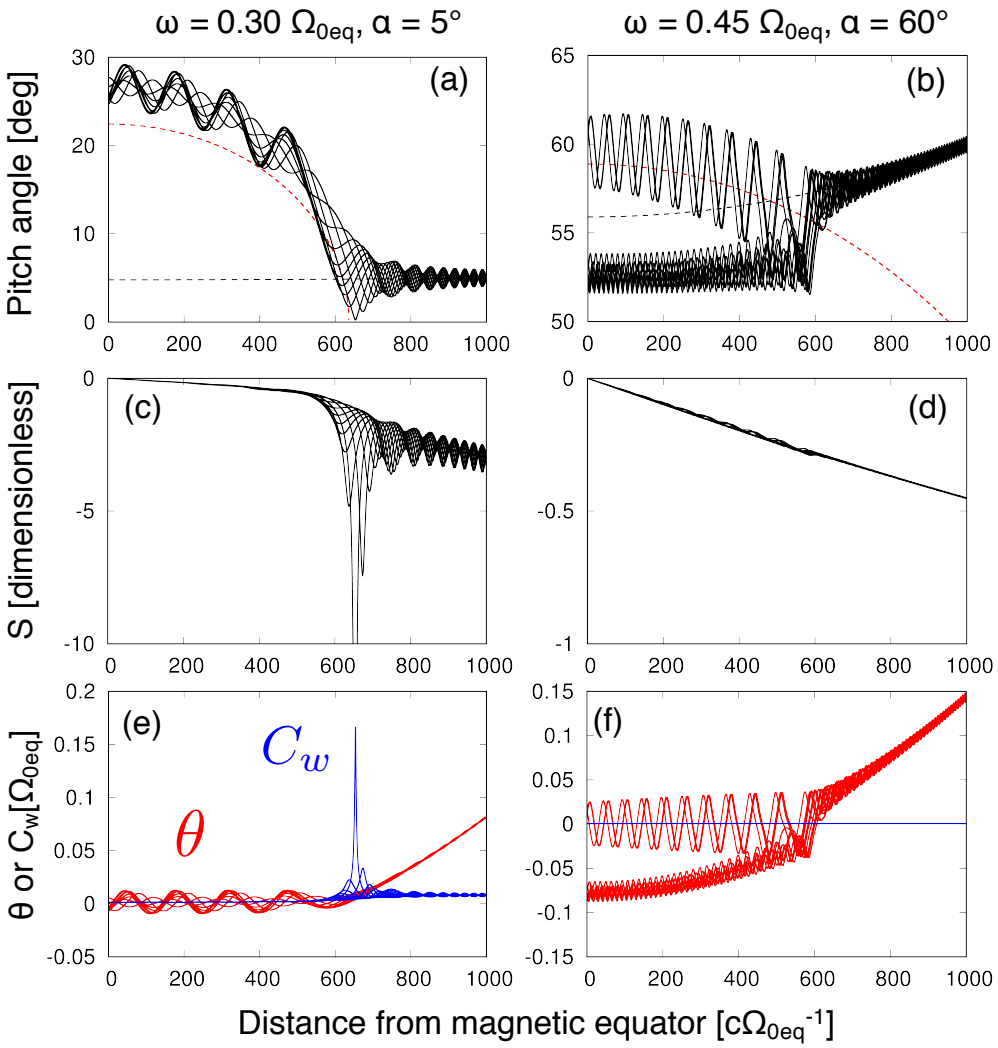

Figure 4.5: Simulation results of α, S, θ, and C_w of low and moderate pitch angle particles.

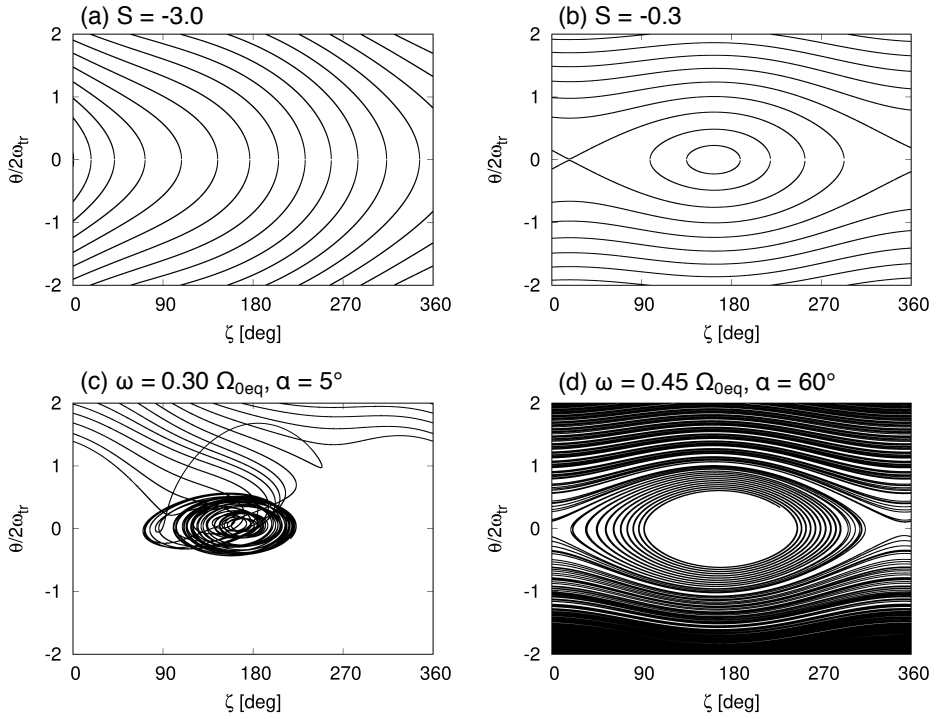

Figure 4.6: Trajectories in the ζ-θ phase space of low and moderate pitch angle particles.

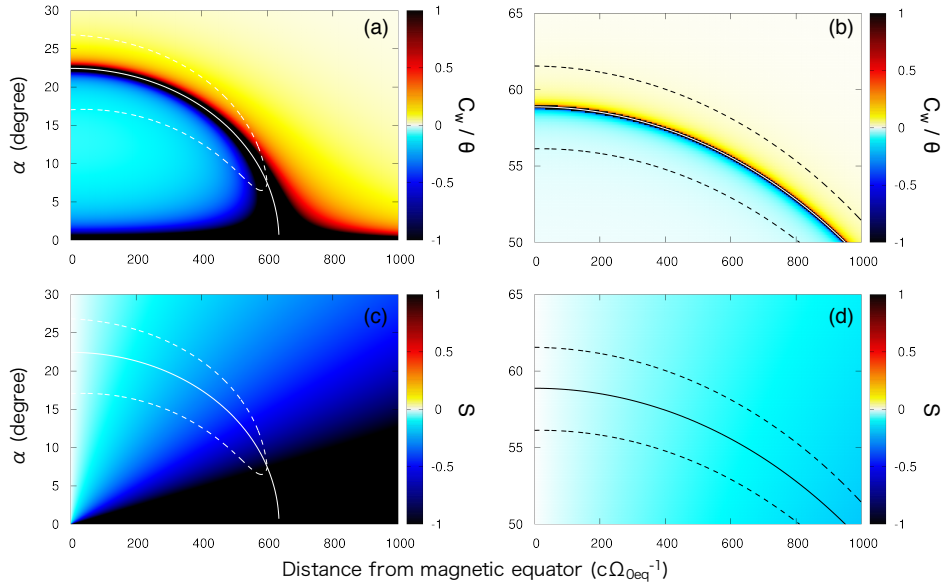

Figure 4.7: Spatial mapping of C_w/θ and S expected by nonlinear theory.

4.7 (b)), therefore the moderate pitch angle approximation is suitable for this parameter. On the contrary, $|S|$ parameter is larger than 1 near the resonance conditions and the width of hole is not defined (Figure 4.7 (c)) and C_w is large than θ (Figure 4.7 (a)), therefore the low pitch angle approximation is suitable for this parameter. In this case, the nonlinear effect at low pitch angle is effective in the pitch angle range of less than 5 degrees (indicated as a black region and outside of hole in Figure 4.7 (a)).

Using 90000 particles in the case 2 (chorus-like frequency model), we calculate the pitch angle distribution at the magnetic equator (Figure 4.8) during one wave packet of chorus emissions through pass the interaction region. Each panel corresponds to each wave amplitude B_w =0.010, 0.025, 0.050, 0.075, and 0.100 % of B_0. In the case of waves with weak amplitude ($\geq$ 0.025 % of B_0), we can recognize diffusion-like scattering (weak bi-directional scattering). On the contrary, with larger amplitude ($\leq$ 0.05 % of B_0), low pitch angle electrons are effectively scattered away from loss cone. A hole is formed at low pitch angle region, and a bump is formed at the resonant pitch angle corresponding to the final frequency of a wave packet.

4.3 Discussion

In the regime of the strong diffusion in the quasilinear theory [e.g., Lyons, 1974], they considered that the loss cone is filled by electrons scattered by waves within the bounce motion period, and the scattering intensity is proportional to the square of the magnetic amplitude. However, this theory and test particle simulation results suggest that the relation between chorus intensity and the flux of auroral electron precipitation is not straightforward, and large amplitude waves such as chorus emissions cannot reproduce the

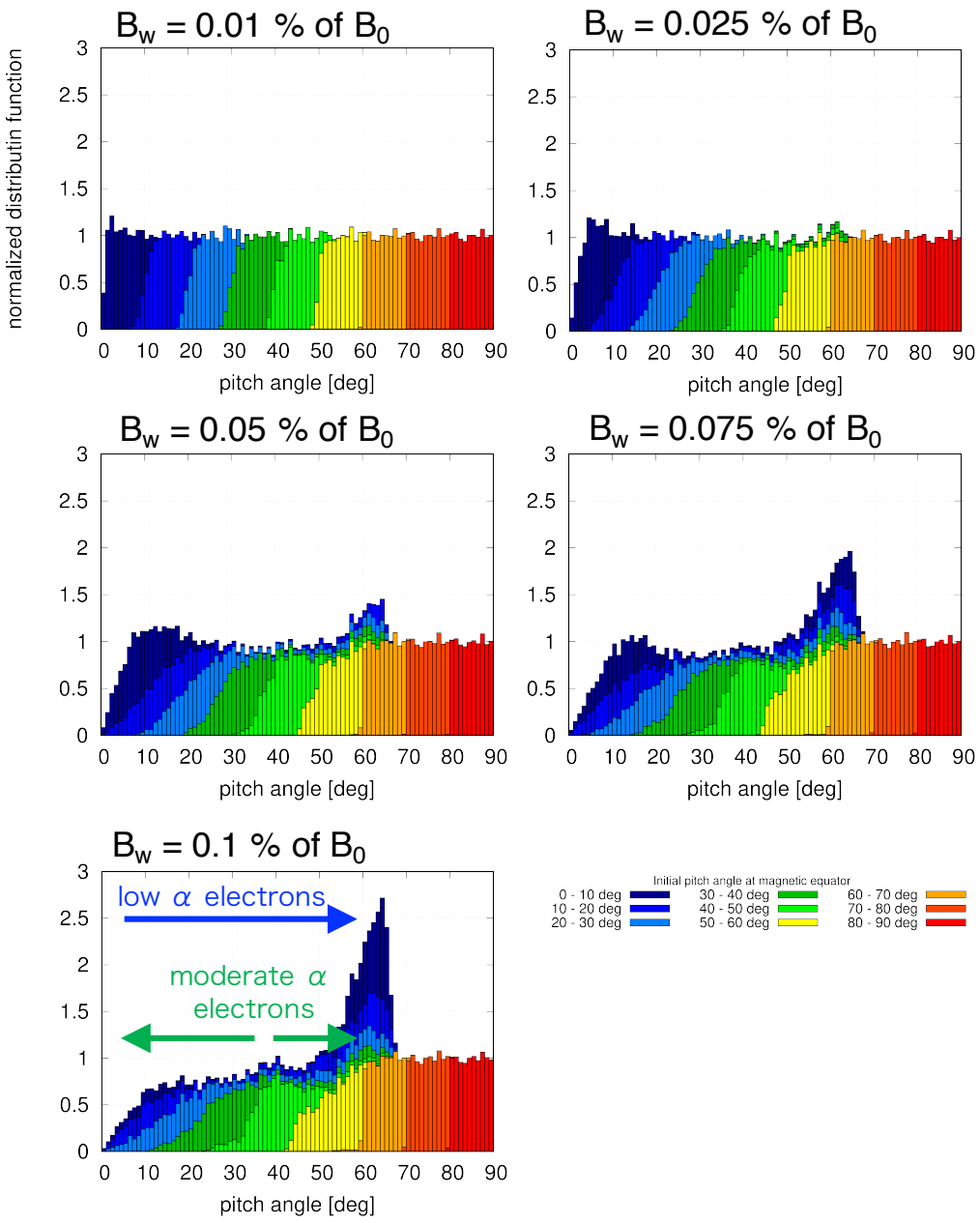

Figure 4.8: Pitch angle distribution after one chorus element pass through for each wave amplitude. As a initial condition, we input the flat distribution as a pitch angle distribution of electrons. Each color corresponds to initial pitch angle at equator.

scattering like the strong diffusion. Note that we do not conclude that the chorus emissions cannot contribute to precipitation into the ionosphere. In the lower panel of Figure 4.8, pitch angle distribution of in the pitch angle region of 0 to 10° (dark blue) are decreased and scattered toward 90° but a few of electrons in pitch angle range of 10 to 20° (blue) penetrate into the extremely small pitch angle range within 3° corresponding to the loss cone. Therefore, we can conclude waves scatter a few electrons into the loss cone but we need investigate with realistic parameters to reveal whether pitch angle scattering by chorus emissions reproduce the sufficient precipitation flux to cause the pulsating aurora. Additionally, the subpacket structure of wave amplitude might contribute to detrapping and lowering the trapping efficiency because small amplitude waves cannot trapped due to insufficient wave potential.

Fennel et al. (2014) reported that Radiation Belt Storm Probes (RBSP) detected the electron distribution bunching in pitch angle when chorus emissions were detected, and the shape of pitch angle distribution is closely resemble to Figure 4.9. We cannot directly compare to the RBSP observations because the input parameters such as wave amplitude, wave frequency, cold density, and the initial pitch angle distribution are different, however, there are possibility of the contribution of trapped particles.

Furthermore, this process of pitch angle scattering should contribute to wave generation process. As shown in Figure 4.3 and 4.4, because the kinetic energy of trapped electrons increase by waves, waves might be damped by electrons scattered away from the loss cone. Therefore, we can predict that the wave generation is determined by the balance of the electrons scattered around the electromagnetic electron hole with moderate pitch angle which loss the energy and electrons scattered away from loss cone with low

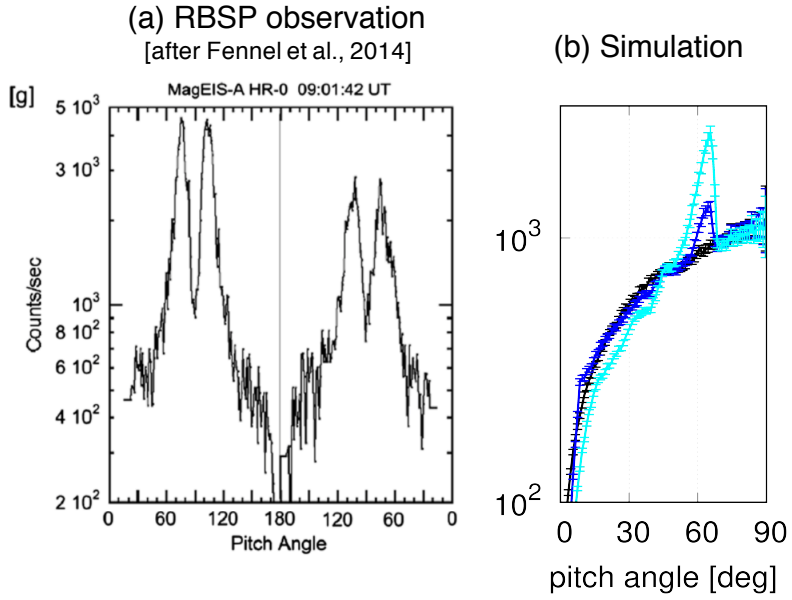

Figure 4.9: (a) Pitch angle distribution of 20 - 40 keV electrons detected by RBSP [Fennel et al., 2014] and (b) simulation results plotted in logarithmic scale.

pitch angle which damp waves. Moreover, because the bunched pitch angle distribution have thermal anisotropy, the electron distribution as a result of scattering caused by waves might generate the waves again. In order to quantitative evaluate this concept of repetition of chorus elements, we need the simulation with realistic parameter.

4.4 Concluding remarks

We clarify the motion of the low pitch angle electrons during encountering the coherent whistler mode waves. Conventional nonlinear theory has predicted that the majority of resonant electrons move along the outermost closed trajectory in θ–ζphase space caused by the wave potential and that the electrons are scattered toward the loss cone. However, as is described in

section 1, almost all of the low pitch angle electrons are trapped by waves and scattered away from the loss cone. This is because that the ζ motion of low pitch angle electrons are efficiently affected from the Lorentz force due to small $v_\perp$, namely α. The motion of these electrons is regulated in the θ–ζ phase space toward $\zeta \to 90°$, which direction is antiparallel to the wave electric field and parallel to the $-e\boldsymbol{v}_\parallel \times \boldsymbol{B}_w$. Consequently, $v_\perp$ increases, i. e., the pitch angle becomes higher. The large amplitude waves tend to trap the particles efficiently, and frequency sweep also contributes to scattering them away from the loss cone. This is because the higher frequency wave can resonate with the higher pitch angle particles, and accelerated particles can also resonate with the higher frequency wave. Hence, the rising tone emissions can efficiently scatter the trapped particles away from the loss cone. Furthermore, scattered electrons away from the loss cone produce the bunch of pitch angle distribution around the resonant pitch angle at the magnetic equator. This result indicates that scattered electrons gain the energy from the waves, and might contribute to wave damping process. Moreover, the bunched electrons reconstruct the anisotropic pitch angle distribution.

Chapter 5

Conclusions

5.1 Summary of this thesis

Whistler mode chorus emissions are one of frequently observed plasma waves in the inner magnetosphere. Chorus emissions are characterized by discrete emissions composed of coherent emissions with a frequency sweep. The frequency sweep is a strong evidence that non-linear processes are responsible for chorus generation [e.g., Omura et al., 2008, 2009]. Pitch angle scattering of energetic electrons caused by chorus emissions is one of candidate of driver of auroral precipitation. Electromagnetic ion cyclotron (EMIC) waves are another mode of plasma waves related to ion cycrotron resonance, and EMIC waves can also scatter energetic ions in pitch angle and cause proton aurora [e.g., Yahnin et al., 2007; Sakaguchi et al., 2008; Nomura et al., 2012; Nishimura et al., 2014]. Recently, the rising tones of EMIC waves are discovered by satellite observations in the magnetosphere [e.g., Pickett et al., 2010; Sakagushi et al., 2013; Nakamura et al, 2014] that involve nonlinear processes [Omura et al., 2010]. These pitch angle scattering by wave-particle interaction not only causes the auroral precipitation but also plays an im-

portant role in loss of ring current particles [e.g., Jordanova et al., 1997]. Therefore, both chorus and EMIC waves are significant plasma waves closely related to the inner magnetospheric and auroral dynamics, and involve nonlinear wave-particle interaction processes. In this thesis, we focused on the two main aims: to establish the method of direct detection of nonlinear pitch angle scattering and to understand the basic process of nonlinear pitch angle scattering using simulation and observation data.

WPIA method for pitch angle scattering

We proposed a new method of detecting pitch angle scattering using the WPIA in chapter 2. The time variation of the pitch angle is formulated as the time variation of the momentum, which is the Lorentz force in the direction of increasing pitch angle, and the measurable value G is defined as the direction of varying pitch angle component of the lost momentum of the wave electromagnetic fields. We applied the proposed method to simulation results reproducing the generation of whistler mode chorus emissions and evaluated the feasibility of the proposed method. We analyzed simulation data at fixed points in the simulation system, and the results inidecated that the time variation of the pitch angle distribution of electrons is very small, but the G values clearly show the statistically significant results of pitch angle scattering. The simulation results clarified that the proposed method enables us to directly detect the nonlinear pitch angle scattering of electrons caused by whistler mode chorus emissions. Furthermore, calculating G, we can identify the location at which pitch angle scattering occurs and the energy and pitch angle ranges in which energetic electrons are effectively scattered. In this simulation, the detected G values correspond to $\left\langle \frac{\mathrm{d}\alpha}{\mathrm{d}t} \right\rangle = 0.36°/\mathrm{ms}$ in the nonlinear phase. The pitch angle variation as a result of wave particle

interaction is stronger than the pitch angle variation expected by the quasi-linear diffusion coefficient. Additionally, in chapter 2, we focused on the pitch angle scattering of energetic ions caused by rising tone EMIC waves observed by THEMIS satellites, and applied the proposed method of WPIA to detect the pitch angle scattering. THEMIS D observed rising tone EMIC waves on September 9, 2010 during the period from 14:20 UT to 14:45 UT. Using high resolution waveform and particle data detected by ESA, EFI and FGM installed on THEMIS D, we calculated G values proposed in previous chapter. As a result, we successfully detected the pitch angle scattering of ions in the observation data when rising tone EMIC waves are detected even if the temporal variation of pitch angle distribution of ions is small. Furthermore, we compared the THEMIS observation with simulation data reproduced by an ion hybrid code. The simulation results were provided by Dr. Shoji, M. of Nagoya University. Both data is in good agreement with each other, and these results are also consistent with Gendrin's theory. Applying the proposed method to both interaction between rising tone EMIC waves and ions, and between chorus emissions and electrons, we found that the utility of the proposed method of WPIA to directly detect pitch angle scattering for simulation and real observation.

Nonlinear effect of low pitch angle particles

We clarify the motion of low pitch angle electrons during encountering the coherent whistler mode waves. Conventional nonlinear theory has predicted that the majority of resonant electrons move along the outermost closed trajectory in θ–ζ phase space caused by the wave potential and that the electrons are scattered toward the loss cone. However, almost all of low pitch angle electrons are trapped by waves and scattered away from the loss

cone. This is because that the ζ motion of low pitch angle electrons are efficiently affected from the Lorentz force due to small $v_\perp$, namely low α. The motion of these electrons is regulated in the θ–ζ phase space toward $\zeta \to 90°$, which direction is antiparallel to the wave electric field and parallel to the $-e\boldsymbol{v}_\parallel \times \boldsymbol{B}_w$. Consequently, $v_\perp$ increases, i.e., the pitch angle becomes higher. The large amplitude waves tend to trap the particles efficiently, and frequency sweep also contributes to scattering them away from the loss cone. This is because the higher frequency wave can resonate with the higher pitch angle particles, and accelerated particles can also resonate with the higher frequency wave. Hence, the rising tone emissions can efficiently scatter the trapped particles away from the loss cone. Furthermore, scattered electrons away from the loss cone produce the bunch of pitch angle distribution around the resonant pitch angle at the magnetic equator. This result indicates that scattered electrons gain the energy from waves, and might contribute to wave damping process. On the contrary, the scattered electrons construct a bump at the magnetic equator after bounce motion. The bumped pitch angle distribution has anisotropy and it could lead to wave generation process.

5.2 Remaining issues and future works

In chapter 3, we focused on the pitch angle scattering between the EMIC waves and ions. THEMIS satellites have observed 228 EMIC wave events with particle burst-mode data including the event of which frequency spectrum is obscure. Through the multi-event analysis of EMIC waves (not only the rising tone emissions) with WPIA method, we will determine spatial distribution of the G parameter and discuss how commonly pitch angle interactions occur between EMIC waves and energetic protons. Furthermore,

we can create the L-MLT distribution of the G parameter. On the based of the L-MLT spatial distribution, we will discuss where and when non-linear interactions occur between EMIC waves and ring current ions, and how effectively ions are scattered. Additionally, Magnetosperic Multiscale (MMS) satellites, launched on March 15, 2015, have 8 particle detectors for each probes, and provide high time resolution data (velocity distribution function is output per 0.15 s). MMS data is suitable for estimating and validating the absolute value of G.

In chapter 2, we proposed a new method to detect pitch angle scattering of energetic particles caused by plasma waves using WPIA. The proposed method can be applied to various types of wave-particle interactions in space plasma. A significant future work is the application of the proposed method to observations made in space by the ERG satellite. ERG satellite was launched on December 20, 2016. Direct measurements in space plasma will provide important clues to the study of processes governing pitch angle scattering of energetic particles in the magnetosphere. WPIA designed for chorus observation was installed on ERG satellite for the first time in the world. Main purpose of WPIA on ERG satellite is to measure the energy exchange, but we can try to apply method for detection of pitch angle scattering through the update of the installed program If we obtain the data observed WPIA on ERG, we can compare the observation with simulation data. Comparison between observation and simulation enables us to discuss the interaction energy range, scattering direction, and other basic property of pitch angle scattering of electrons caused by chorus emissions.

We also expect that ERG satellite observation detect the nonlinear effect of pitch angle scattering investigated in chapter 4. We will model the waveform from the observed burst mode waveform data, and then will carry out

the test particle simulation in the modeled waveform. Comparing pitch angle distribution of electrons observed by ERG satellite with simulation results, we can clarify how effectively nonlinear wave particle interaction modulate the electron pitch angle distribution in the real space. Also the contribution of scattered particles to generation or damping of waves is a remaining issue. We need to carry out the simulation using particles in more wide energy range, and clarify the contribution to generation or damping mechanism of chorus elements. Furthermore, we expect that the nonlinear effect can contribute to proton scattering caused by EMIC waves more effectively because amplitudes of rising tones EMIC waves can reach more than 1 % of ambient magnetic fields. Therefore, quantitative estimation of nonlinear effect for the interaction between EMIC waves and protons are needed.

References

[1] Albert, J. M. (1999), Analysis of quasi-linear diffusion coefficients, J. Geophys. Res., 104, 2429.

[2] Allcock, G. M. (1957), A study of the audio-frequency radio phenomenon known as "dawn chorus '' , Aust. J. Phys., 10, 286.

[3] Angelopoulos, V. (2008), The THEMIS mission, Space Sci. Rev., 141, 534, doi:10.1007/s11214-008-9336-1.

[4] Auster, H. U., et al. (2008), The THEMIS fluxgate magnetometer, 141(1-4), 235264, doi:10.1007/s11214-008-9365-9.

[5] Bonnell, J. W., F. S. Mozer, G. T. Delory, A. J. Hull, R. E. Ergun, C. M. Cully, V. Angelopoulos, and P. R. Harvey (2008), The electric field instrument (EFI) for THEMIS, 141(1-4), 303341, doi:10.1007/s11214-008-9469-2.

[6] Burtis, W., and R. Helliwell (1969), Banded chorus—A new type of VLF radiation observed in the magnetosphere by OGO 1 and OGO 3, *J. Geophys. Res.*, 74(11), 3002, doi:10.1029/JA074i011p03002.

[7] Cornwall, J. M. (1965), Cyclotron instabilities and electromagnetic emission in the ultra low frequency and very low frequency ranges, J. Geophys. Res., 70(1), 6169, doi:10.1029/JZ070i001p00061.

[8] Cornwall, J.M., Coroniti, F.V., Thorne, R.M. (1970), Turbulent loss of ring current protons. J. Geophys. Res. 75, 46994709.

[9] Dysthe, K. B. (1971), Some studies of triggered whistler emissions, J. Geophys. Res., 76(28), 69156931, doi:10.1029/JA076i028p06915.

[10] Engebretson, M. J., et al. (2015), Van Allen probes, NOAA, GOES, and ground observations of an intense EMIC wave event extending over 12 h in magnetic local time, J. Geophys. Res. Space Physics, 120, 54655488, doi:10.1002/ 2015JA021227.

[11] Ergun, R. E., C. W. Carlson, J. P. McFadden, J. H. Clemmons, and M. H. Boehm (1991), Langmuir wave growth and electron bunching: Results from a wave–particle correlator, *J. Geophys. Res.*, 96(A1), 225–238, doi:10.1029/90JA01596.

[12] Fennell, J. F., et al. (2014), Van Allen Probes observations of direct wave- particle interactions, Geophys. Res. Lett., 41, 18691875, doi:10.1002/ 2013GL059165.

[13] Fukuhara, H., H. Kojima, Y. Ueda, Y. Omura, Y. Katoh, and H. Yamakawa (2009), A new instrument for the study of wave-particle interactions in space: One-chip Wave-Particle Interaction Analyzer, *Earth Planets Space*, 61, 765.

[14] Furuya, N., Y. Omura, and D. Summers (2008), Relativistic turning acceleration of radiation belt electrons by whistler mode chorus, J. Geophys. Res., 113, A04224, doi:10.1029/2007JA012478.

[15] Gendrin, R. (1981), General relationships between wave amplification and particle diffusion in a magnetoplasma, Rev. Geophys., 19(1), 171-184.

[16] Glauert, S. A., and R. B. Horne (2005), Calculation of pitch angle and energy diffusion coefficients with the PADIE code, J. Geophys. Res., 110, A04206, doi:10.1029/2004JA010851.

[17] Gurnett, D. A., and B. J. O ' Brien, High-latitude geophysical studies with Satellite Injun 3: 5. Very low frequency electromagnetic radiation, J. Geophys. Res., 69, 65, 1964.

[18] Helliwell, R. A. (1965), Whistler and Related Ionospheric Phenomena, Stanford Univ. Press, Stanford, Calif.

[19] Helliwell, R. A. (1967), A theory of discrete emissions from the magnetosphere, J. Geophys. Res., 72, 47734790, doi:10.1029/JZ072i019p04773.

[20] Hikishima, M., S. Yagitani, Y. Omura, and I. Nagano (2009), Coherent nonlinear scattering of energetic electrons in the process of whistler mode chorus generation, *J. Geophys. Res.*, 114(A10), A10205, doi:10.1029/2009JA014371.

[21] Hikishima, M., Y. Omura, and D. Summers (2010), Microburst precipitation of energetic electrons associated with chorus wave generation, *Geophys. Res. Lett.*, 37, L07103, doi:10.1029/2010GL042678.

[22] Horne, R. B., and R. M. Thorne (2003), Relativistic electron acceleration and precipitation during resonant interactions with whistler-mode chorus, *Geophys. Res. Lett.*, 30(10), 1527, doi:10.1029/2003GL016973.

[23] Jordanova, V. K., et al. (1997), Kinetic model of the ring current-atmosphere interactions, J. Geophys. Res., 102, 14279, 10.1029/96JA03699.

[24] Katoh, Y., and Y. Omura (2007a), Computer simulation of chorus wave generation in the Earth's inner magnetosphere, *Geophys. Res. Lett.*, 34, L03102, doi:10.1029/2006GL028594.

[25] Katoh, Y., and Y. Omura (2007b), Relativistic particle acceleration in the process of whistler-mode chorus wave generation, *Geophys. Res. Lett.*, 34, L13102, doi:10.1029/2007GL029758.

[26] Katoh, Y., and Y. Omura (2011), Amplitude dependence of frequency sweep rates of whistler-mode chorus emissions, *J. Geophys. Res.*, 116, A07201, doi:10.1029/2011JA016496.

[27] Katoh, Y., Y. Omura, and D. Summers (2008), Rapid energization of radiation belt electrons by nonlinear wave trapping, *Ann. Geophys.*, 26, 3451–3456, doi:10.5194/angeo-26-3451-2008, 2008.

[28] Katoh, Y. et al. (2013), Significance of Wave-Particle Interaction Analyzer for direct measurements of nonlinear wave-particle interactions, *Ann. Geophys.*, 31, doi:10.5194/angeo-31-503-2013.

[29] Kennel, C. F. and F. Engelmann, (1966), Velocity Space Diffusion from Weak Plasma Turbulence in a Magnetic Field, Physics of Fluids, 9, 2377, doi:10.1063/1.1761629.

[30] Kennel, C. F., and H. E. Petschek (1966), Limit on stably trapped particle fluxes, *J. Geophys. Res.*, 71(1), 1, doi:10.1029/JZ071i001p00001.

[31] Lerche, I. (1968), Quasilinear Theory of Resonant Diffusion in a Magneto- Active, Relativistic Plasma, Physics of Fluids, 11, 1720, doi:10.1063/1.1692186.

[32] Li, J., et al. (2015), Comparison of formulas for resonant interactions between energetic electrons and oblique whistler-mode waves, Phys.Plasmas, 22, 052922, doi:10.1063/1.4914852.

[33] Li, W., R. M. Thorne, J. Bortnik, Y. Y. Shprits, Y. Nishimura, V. Angelopoulos, C. Chaston, O. Le Contel, and J. W. Bonnell (2011), Typical properties of rising and falling tone chorus waves, Geophys. Res. Lett., 38, L14103, doi:10.1029/ 2011GL047925.

[34] Lorentzen, K., J. Blake, U. Inan, and J. Bortnik (2001), Observations of relativistic electron microbursts in association with VLF chorus, *J. Geophys. Res.*, 106(A4), 6017, doi:10.1029/2000JA003018.

[35] Lyons, L. R., R. M. Thorne, and C. F. Kennel (1971), Electron pitch-angle diffusion driven by oblique whistler-mode turbulence, J. Plasma Physics, 6(3), 589-606, doi:10.1017/S0022377800006310.

[36] Lyons, L. R. (1974), Pitch angle and energy diffusion coefficients from resonant interactions with ion-cyclotron and whistler waves, *J. Plasma Phys.*, 12, 417, doi:10.1017/S002237780002537X.

[37] Matsumoto, H., and Y. Omura (1981), Cluster and channel effect phase bunching by whistler waves in the nonuniform geomagnetic field, J. Geophys. Res., 86, 779.

[38] McFadden, J. P., et al. (2008), The THEMIS ESA plasma instrument and in- flight calibration, Space Sci. Rev., 141, 277302, doi:10.1107/s11214-008-9440-2.

[39] Meredith, N. P., R. B. Horne, and R. R. Anderson (2001), Substorm dependence of chorus amplitudes: Implications for the accelera-

tion of electrons to relativistic energies, *J. Geophys. Res.*, 106, 13165, doi:10.1029/2000JA900156.

[40] Meredith, N. P., R. B. Horne, R. H. A. Iles, R. M. Thorne, D. Heynderickx, and R. R. Anderson (2002), Outer zone relativistic electron acceleration associated with substorm-enhanced whistler mode chorus, *J. Geophys. Res.*, 107(A7), 1144, doi:10.1029/2001JA900146.

[41] Miyoshi, Y., A. Morioka, T. Obara, H. Misawa, T. Nagai, and Y. Kasahara (2003), Rebuilding process of the outer radiation belt during the 3 November 1993 magnetic storm: NOAA and Exos-D observations, *J. Geophys. Res.*, 108(A1), 1004, doi:10.1029/2001JA007542.

[42] Miyoshi, Y., Y. Katoh, T. Nishiyama, T. Sakanoi, K. Asamura, and M. Hirahara (2010), Time of flight analysis of pulsating aurora electrons, considering wave–particle interactions with propagating whistler mode waves, *J. Geophys. Res.*, 115, A10312, doi:10.1029/2009JA015127.

[43] Miyoshi, Y. et al. (2012), The Energization and Radiation in Geospace (ERG) Project, in: Dynamics of the Earth's Radiation Belts and Inner Magnetosphere, Geophys. Monogr. Ser., 199, edited by: D. Summers, I. R. Mann, D. N. Baker, and M. Schulz, 103–116, AGU, Washington, D.C., doi:10.1029/2012GM001304.

[44] Miyoshi, Y., et al. (2015), Relation between fine structure of energy spectra for pulsating aurora electrons and frequency spectra of whistler mode chorus waves, J. Geophys. Res. Space Physics, 120, 77287736, doi:10.1002/2015JA021562.

[45] Nakamura, R., M. Isowa, Y. Kamide, D. Baker, J. Blake, and M. Looper (2000), SAMPEX observations of precipitation bursts

in the outer radiation belt, *J. Geophys. Res.*, 105(A7), 15875, doi:10.1029/2000JA900018.

[46] Nakamura, S., Y. Omura, S. Machida, M. Shoji, M. Nose, and V. Angelopoulos (2014), Electromagnetic ion cyclotron rising tone emissions observed by THEMIS probes outside the plasmapause, J. Geophys. Res. Space Physics, 119, 18741886, doi:10.1002/2013JA019146.

[47] Nishimura, Y., J. Bortnik, W. Li, R. M. Thorne, L. R. Lyons, V. Angelopoulos, S. B. Mende, J. Bonnell, O. Le Contel, C. Cully, R. Ergun, and U. Auster (2010), Identifying the driver of pulsating aurora, *Science (New York, N.Y.)*, 330(6000), 81, doi:10.1126/science.1193186.

[48] Nishimura, Y., et al. (2011), Multievent study of the correlation between pulsating aurora and whistler mode chorus emissions, J. Geophys. Res., 116, A11221, doi:10.1029/2011JA016876.

[49] Nishimura, Y., et al, (2013), Structures of dayside whistler-mode waves deduced from conjugate diffuse aurora, J. Geophys. Res. Space Physics, 118, 664673, doi:10.1029/2012JA018242.

[50] Nishimura, Y., J. Bortnik, W. Li, L. R. Lyons, E. F. Donovan, V. Angelopoulos, and S. B. Mende (2014), Evolution of nightside subauroral proton aurora caused by transient plasma sheet flows, J. Geophys. Res. Space Physics, 119, 5295?5304, doi:10.1002/2014JA020029.

[51] Nishiyama, T., T. Sakanoi, Y. Miyoshi, Y. Katoh, K. Asamura, S. Okano, and M. Hirahara (2011), The source region and its characteristic of pulsating aurora based on the Reimei observations, *J. Geophys. Res.*, 116, A03226, doi:10.1029/2010JA015507.

[52] Nomura, R., K. Shiokawa, K. Sakaguchi, Y. Otsuka, and M. Connors (2012), Polarization of Pc1/EMIC waves and related proton auroras observed at subauroral latitudes, J. Geophys. Res., 117, A02318, doi:10.1029/2011JA017241.

[53] Nomura, R., K. Shiokawa, Y. Omura, Y. Ebihara, Y. Miyoshi, K. Sakaguchi, Y. Otsuka, and M. Connors (2016), Pulsating proton aurora caused by rising tone Pc1 waves, J. Geophys. Res. Space Physics, 121, 1608?1618, doi:10.1002/2015JA021681.

[54] Nunn, D. (1974), A self consistent theory of triggered VLF emissions, Planet. Space Sci., 22, 349378, doi:10.1016/0032-0633(74)90070-1.

[55] Oliven, M., and D. Gurnett (1968), Microburst phenomena: 3. An association between microbursts and VLF chorus, *J. Geophys. Res.*, 73(7), 2355, doi:10.1029/JA073i007p02355.

[56] Omura, Y., Y. Katoh, and D. Summers (2008), Theory and simulation of the generation of whistler-mode chorus, *J. Geophys. Res.*, 113, doi:10.1029/2007JA012622.

[57] Omura, Y., M. Hikishima, Y. Katoh, D. Summers, and S. Yagitani (2009), Nonlinear mechanisms of lower-band and upper-band VLF chorus emissions in the magnetosphere, *J. Geophys. Res.*, 114, doi:10.1029/2009JA014206.

[58] Omura, Y., J. Pickett, B. Grison, O. Santolik, I. Dandouras, M. Engebretson, P. M. E. Decreau, and A. Masson (2010), Theory and observation of elec- tromagnetic ion cyclotron triggered emissions in the magnetosphere, J. Geophys. Res., 115, A07234, doi:10.1029/2010JA015300.

[59] Preece, W. H. (1894), Earth Currents, Nature 49, 554-554 (12 April 1894) — doi:10.1038/049554b0

[60] Pickett, J. S., et al. (2010), Cluster observations of EMIC triggered emissions in association with Pc1 waves near Earth ' s plasmapause, Geophys. Res. Lett., 37, L09104, doi:10.1029/2010GL042648.

[61] Saito, S., Y. Miyoshi, and K. Seki (2012), Relativistic electron microbursts associated with whistler chorus rising tone elements: GEMSIS-RBW simulations, *J. Geophys. Res.*, 117(A10), A10206, doi:10.1029/2012JA018020.

[62] Sakaguchi, K., K. Shiokawa, Y. Miyoshi, Y. Otsuka, T. Ogawa, K. Asamura, and M. Connors (2008), Simultaneous appearance of isolated auroral arcs and Pc 1 geomagnetic pulsations at subauroral latitudes, J. Geophys. Res., 113, A05201, doi:10.1029/2007JA012888.

[63] Santolik, O., M. Parrot, and F. Lefeuvre (2003), Singular value decomposition methods for wave propagation analysis, Radio Sci., 38(1), 1010, doi:10.1029/2000RS002523.

[64] Santolik, O., D. A. Gurnett, J. S. Pickett, M. Parrot, and N. Cornilleau-Wehrlin (2003), Spatio-temporal structure of storm-time chorus, J. Geophys. Res., 108(A7), 1278, doi:10.1029/2002JA009791.

[65] Santolik, O., E. Macusova, E. E. Titova, B. V. Kozelov, D. A. Gurnett, J. S. Pickett, V. Y. Trakhtengerts, and A. G. Demekhov (2008), Frequencies of wave packets of whistler-mode chorus inside its source region: a case study, Ann. Geophys., 26, 16651670.

[66] Shoji, M., and Y. Omura (2011), Simulation of electromagnetic ion cyclotron triggered emissions in the Earth ' s inner magnetosphere, J. Geophys. Res., 116, A05212, doi:10.1029/2010JA016351.

[67] Shoji, M., and Y. Omura (2013), Triggering process of electromagnetic ion cyclotron rising tone emissions in the inner magnetosphere, J. Geophys. Res. Space Physics, 118, 55535561, doi:10.1002/jgra.50523.

[68] Stix, T. H. (1992), Waves in Plasmas, Am. Inst. of Phys., New York.

[69] Storey, L. R. O. (1953), An investigation of whistling atmospherics, Philos. Trans. R. Soc. London, Ser. A, 246, 113 141, doi:10.1098/rsta.1953.0011.

[70] Summers, D., R. M. Thorne, and F. Xiao (1998), Relativistic theory of wave-particle resonant diffusion with application to electron acceleration in the magnetosphere, J. Geophys. Res., 103, 20,487–20,500.

[71] Summers, D. (2005), Quasi-linear diffusion coefficients for field-aligned electromagnetic waves with applications to the magnetosphere, J. Geophys. Res., 110, A08213, doi:10.1029/2005JA011159.

[72] Thorne, R. M. (2010), Radiation belt dynamics: The importance of wave- particle interactions, Geophys. Res. Lett., 37, L22107, doi:10.1029/2010GL044990.

[73] Thorne, R., B. Ni, X. Tao, R. Horne, and N. Meredith (2010), Scattering by chorus waves as the dominant cause of diffuse auroral precipitation, *Nature*, 467(7318), 943, doi:10.1038/nature09467.

[74] Trakhtengerts, V. (1995), Magnetosphere cyclotron maser: backward wave oscillator generation regime, J. Geophys. Res., 100, 1720517210.

[75] Trakhtengerts, V. (1999), A generation mechanism for chorus emission, Ann. Geophys., 17, 95100, http://www.ann-geophys.net/17/95/1999/.

[76] Tsurutani, B. T., and E. J. Smith (1974), Postmidnight chorus: A substorm phenomenon, *J. Geophys. Res.*, 79(1), 118, doi:10.1029/JA079i001p00118.

[77] Yahnin, A. G., T. A. Yahnina, and H. U. Frey (2007), Subauroral proton spots visualize the Pc1 source, J. Geophys. Res., 112, A10223, doi:10.1029/2007JA012501.